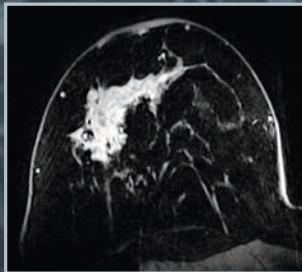


# MAGNETOM Flash

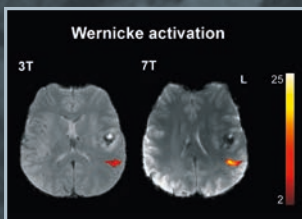
The Magazine of MRI

Issue Number 4/2014 | Oncology Edition

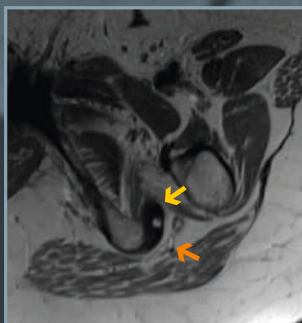
Not for distribution in the US



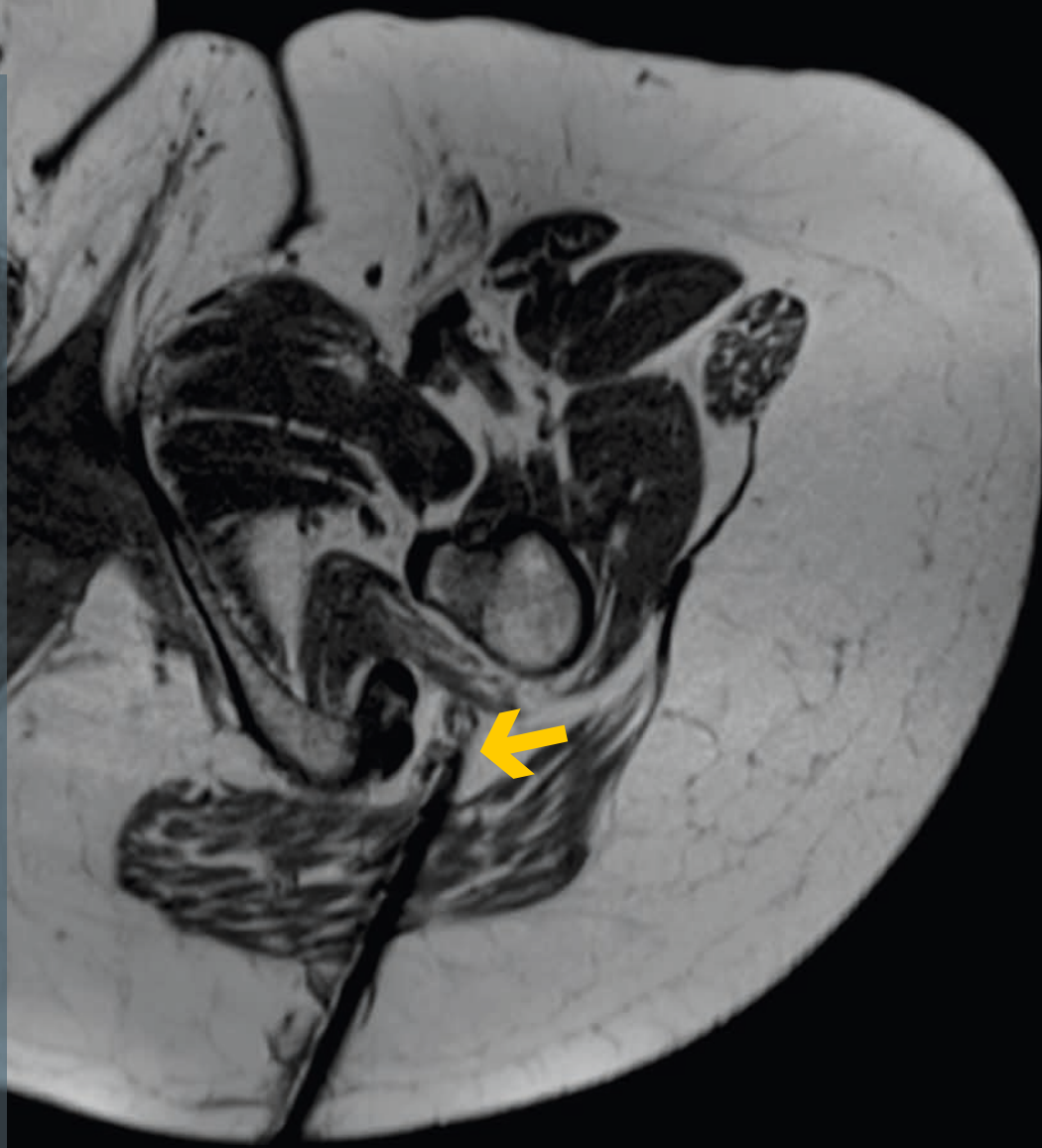
**Clinical Multiparametric  
MR Imaging of Breast  
Tumors at 7 Tesla\***  
Page 54



**fMRI in Presurgical  
Planning at 7T\***  
Page 20



**3 Tesla MR Neurography-  
Guided Posterior Femoral  
Cutaneous Nerve Block**  
Page 30





**Professor Anwar R. Padhani, MB BS, FRCP, FRCR** is Consultant Clinical Radiologist at Mount Vernon Cancer Centre in London and Professor of Cancer Imaging at the Institute of Cancer Research, Royal Marsden Hospital in London, UK.

His research interests include functional imaging and the microenvironment of tumors. Professor Padhani has a passion for teaching and has an impressive record of publications and lectures. His work involving whole-body and multi-parametric MRI is internationally renowned.

## Advancing Cancer Care with Modern MRI

Many aspects of cancer care remain on 'red alert' as we enter the second decade of the 21<sup>st</sup> century. There are many times when we healthcare professionals cannot confidently answer questions that directly affect patient care. Seemingly simple questions such as "Do I have cancer?", "Is the cancer going to kill me?", "Is my cancer responding to therapy?", "Is the cancer back?" and "How long do I have to live?", "Will I make it to my daughter's wedding?" evade us on a daily basis. While we struggle to respond to the needs of our patients, we remain aware that progress is being made every day in cancer diagnosis and therapy, and within this, is the role being played by MRI as highlighted by articles in this Oncology edition of MAGNETOM Flash magazine.

MRI has become an integral part in management of cancer patients with distinct decision making roles in the clinic and for drug development. Clinical questions that can be addressed by MRI are highly dependent on the point of the patient journey. Many cancer-afflicted patients comment on the loss of control of their destiny which makes their progress through life more like a 'roller coaster'. The

optimal use of MRI requires very close interactions between oncologists and their radiologists and physicists. This is because MRI technologies (hardware, data acquisition sequences, post-processing etc) are continuously being developed and refined, validated and adopted for use in the clinic, but at different rates which makes cross platform standardisation and validation problematic. Oncologists need to define specific questions/ problem areas in order for radiologists/physicists to choose or develop appropriate technologies to answer the clinical need. If this is done successfully, both morphologic and generated functional MRI biomarkers have the power to transform the way that some patients are managed in the clinic. This issue of MAGNETOM Flash is full of examples where MRI is being developed to meet clinical needs of cancer patients.

### Early cancer detection

When MRI is employed for early cancer detection in subjects with a high lifetime risk of developing cancer, either due to germline mutations or exposure to carcinogens, this is typically organ-based. Examples of organ-based

MRI screening include evaluation of those at increased risk of developing breast cancer (BRCA mutations, TP53 deletions, previous mantle radiotherapy). The biology being exploited in breast cancer detection and characterization is tumor neovascularization and hyperperfusion, which is done by using dynamic contrast-enhanced sequences (DCE-MRI). A key requirement for early breast cancer detection is very high spatial and temporal resolution of DCE sequences. High spatial resolution is important because lesions detected need characterization which in turn depends on the evaluation of fine morphologic features such as distinctness of margins and the patterns of internal structure. How this can be achieved using ultrahigh field, 7T\* MRI scanners is discussed in the article by Siegfried Trattnig et al. in this issue. The challenges of working at 7T, particularly of achieving uniform fat suppression over both breasts are highlights.

Another area where MRI is increasingly used is for the detection (localization) of suspected cancer when another test(s) suggests that a tumor may be present. Examples include persistently raised serum prostate specific antigen (PSA) levels or when monoclonal bands



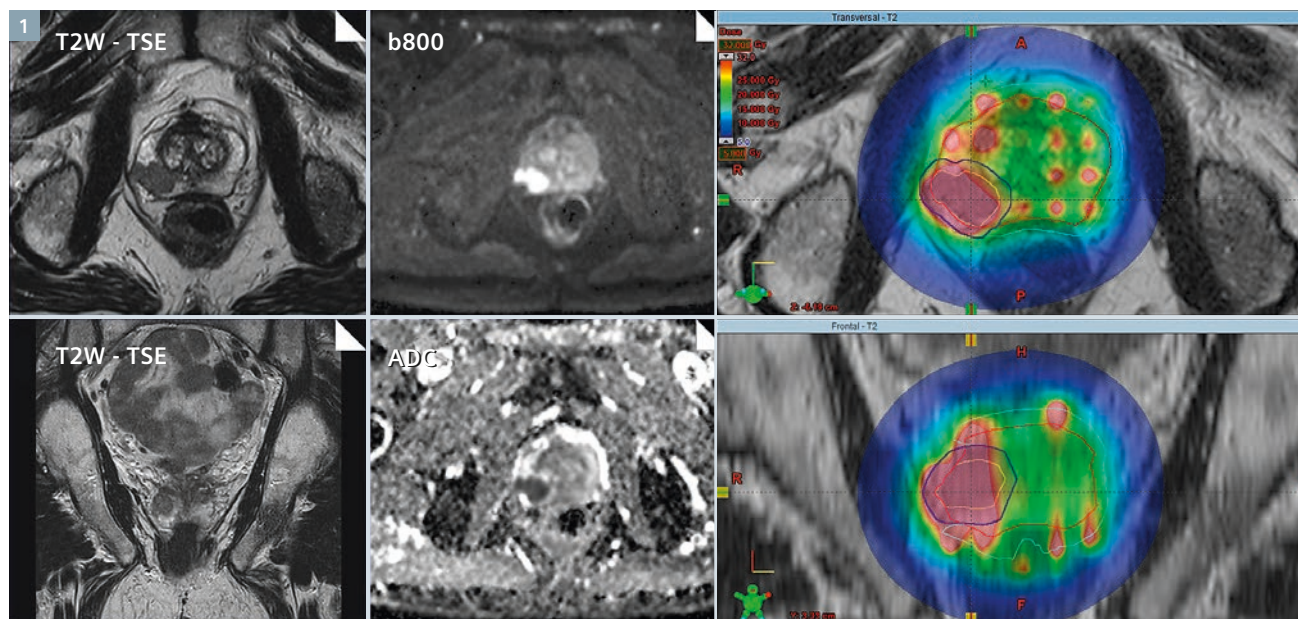
(M component) are found in older patients referred for the investigation of osteoporosis; when respectively prostate cancer and multiple myeloma may be suspected. Prostate cancer diagnosis is particularly problematic because many men with raised PSA will never be diagnosed with prostate cancer in their life (false alarms), with the flip side also being true that many men with diagnosed prostate tumors having normal PSA levels (false reassurance). Even in men with prostate cancer diagnosed from histologic samples, the question "Is the cancer going to cause patient harm?" cannot always be confidently answered, because the misclassification rate concerning risk status is too high (poor characterization). Often there is insufficient confidence to distinguish non-aggressive disease (only needing careful monitoring – active surveillance program) from virulent cancers (requiring definitive treatment). Such diagnostic uncertainty contributes to over-treatment of patients with low-grade cancers and under-treatment of patients with aggressive disease.

Multiparametric MRI (mpMRI) is now incorporated into many guidelines for the detection of prostate cancer particularly in men with persistently raised PSA levels and negative systematic transrectal prostate biopsies, who are considered to harbor cancer that has not yet been diagnosed. Diffusion MRI is a cornerstone of any mpMRI prostate examination as highlighted in the article by Liang Li and colleagues, who demonstrate high resolution, dedicated prostate diffusion MRI. Beyond detection of suspected lesions, better targeted biopsies from cancer suspicious regions at highest risk of harbouring the most aggressive lesion (dominant intra-prostatic lesion (DIL) or index intraprostatic lesion) is needed (Fig. 1). The article by Lars Schimmöller et al. provides practical examples of how this is achieved by in-bore MRI targeted biopsy. Of course mpMRI usage is not only confined to the characterization of prostatic lesions. mpMRI is also being routinely used in the brain and other organs, including gynaecological tumor characterization as highlighted by Hamidreza Sligheh Rad.

## Diagnostic workup

Once patients are diagnosed with cancer, accurate workup of disease extent is key for therapy planning and prognostication. For this, the relationship between the primary tumor and adjacent normal tissues as well as the accurate determining of nodal and metastatic disease status are key requirements. A particularly venerable group of patients that can benefit from multisystem MRI assessments of metastatic disease are children\* with cancer as shown by the case example of Maren Asmussen and Peter Reimer. Of course diagnostic workup of cancer patients goes beyond MRI, using other imaging modalities including PET scans. The hybrid imaging platform PET/CT has already established itself in the cancer evaluation arena but we now see the

\*MR scanning has not been established as safe for imaging fetuses and infants under two years of age. The responsible physician must evaluate the benefit of the MRI examination in comparison to other imaging procedures.



### 1 Biologically optimized radiotherapy.

75-year-old male with prostate cancer (Gleason 4+3; PSA18 ng/mL; T3a; N0; M0).

A dominant intra-prostatic lesion (DIL) in the right postero-lateral peripheral zone has been defined using multi-parametric MRI (T2-weighted and diffusion images (b800 and ADC maps) are shown). High dose rate brachytherapy catheters were inserted under general anaesthetic. The planning computer optimization software has been programmed to maximize the radiation dose to the DIL and limit the dose to the rest of the prostate to a defined ceiling. The DIL and DIL planning treatment volumes (PTV) (yellow and dark blue lines) receive a higher dose as a proportion of their volume than the non-dominant prostate and the non-dominant prostate PTV (light blue and red lines). Courtesy of Dr. Roberto Alonzi, Mount Vernon Cancer Centre, Northwood, UK.

# *“Morphologic and generated functional MRI biomarkers have the power to transform the way that some patients are managed in the clinic.”*

Professor Anwar R. Padhani, MB BS, FRCP, FRCR

emergence of PET/MRI for improving lesion characterization as highlighted by the article of Amy Melsaether in women with breast cancer. Potential advantages of the hybrid PET/MRI approach include more precise registration and anatomic localisation of the PET uptake, the potential for simultaneous quantitative dynamic PET and contrast-enhanced perfusion MRI and shorter scan times (less sedation/anaesthesia). But MRI is not there to just to make PET scanning better! Unlike the situation with PET/CT (where low dose, non-contrast-enhanced CT is used principally for rough anatomic localisation and attenuation correction), the position of MRI in PET/MRI systems is that of an equal partner because of its own uniqueness. MRI strengths include excellence in anatomic imaging and multiparametric imaging capability which, combined with the high sensitivity of PET, have the potential to greatly improve the care of cancer patients, although evidence for the latter is still lacking. Watch this space!

## Transforming treatment

MRI information has to be able to transform what we do for our patients. The article by Marymol Koshy highlights how breast MRI is transforming the surgical approach for breast cancer patients in Malaysia. An impressive article by Simon Robinson and colleagues highlights how functional MRI at 7T\* can aid in the presurgical planning of brain cancer patients. The quality of fMRI is simply astonishing but 7T is not simply about creating pretty pictures! It is about much

more. It is about identifying the precise location of vital brain functions that must be preserved in complex brain surgery. It's about preserving a patient's uniqueness, what makes them human. The article suggests that millimetre precision is required for localizing eloquent brain areas in order to mitigate against severe post-operative deficits which are inevitable with brain tumor surgery without fMRI. You have to admire the efforts of Robinson and colleagues who are trying to make a difference in this very challenging area.

Just as we have seen advances in MRI diagnosis, so we have seen marked progress in image-guided treatment. A striking example is high precision, minimally invasive tumor ablation as highlighted by Kemal Tuncali who shows several case examples of tumor ablation guided by MRI. Another large field of advancement is in image guided radiotherapy. Advances in imaging hardware related to radiation delivery, have improved the physical conformality of radiation planning, treatment and delivery to tumors and organ boundaries using conformal and intensity modulated techniques. Articles by Gary Liney and Joann Prisciandaro highlight how MRI information can offer these advantages when radiation is delivered as external beam radiotherapy and internal high dose rate brachytherapy respectively. The authors reflect on the challenges of incorporating MRI data into the radiotherapy planning processes including the lack of electron density information and image distortion.

When considering further roles for MRI in radiation planning we can also look towards additional advantages that functional imaging, in general, can bring to radiation therapy. The ability to combine image-depicted biology with image-guided radiotherapy techniques opens the way for further refinements of target delineation and dose delivery, such that it is now possible to shape dose volume distributions not only to the geometry of targets but also to differences in the radiobiology across tumors. So it is possible to define additional 'targets-within-targets' as 3D maps of prescribed dose incorporating biological information derived from functional imaging; this is sometimes called 'dose painting by numbers'. An example of such an approach is shown in Figure 1. When considering these additional opportunities, it should be remembered that the perceived advantages of such approaches are currently without a sound evidence base regarding selection of patients who would benefit from these more complex approaches and whether improved patient outcomes will ultimately be seen; there remains incomplete clinical validation of these novel approaches.

## Therapy monitoring

Lastly I would like to mention another challenging area in cancer care, that of treatment monitoring. There is an increasing awareness that the evaluation of tumor response to oncologic treatments based solely on anatomic imaging faces many limitations, particularly in the era of novel biologic targeted therapies. This is illustrated by the difficulty of response assessments in metastatic skeletal disease which unlike soft tissues, are exceptionally difficult to assess morphologically, and in brain tumors where increasing enhancement following chemoradiation therapy may be unduly misinterpreted as disease progression (so-called pseudoprogression). These limitations have hampered the development of new generations of cytostatic drugs also. It was thought that progression free survival (PFS) would serve as a suitable surrogate for overall therapeutic efficacy for the development of cytostatic compounds. However, it is increasingly being recognized that PFS



(most often anatomically determined) is often times disconnected from overall survival, as reported in large scale trials of bevacizumab therapy for metastatic solid tumors and brain gliomas [1, 2].

A particularly problematic area is monitoring response of patients with bone metastases because measureable bony soft tissue disease occurs infrequently. Symptom assessments and development of skeletal-related events (fractures, cord compression, skeletal pain requiring radiotherapy) are preferred markers of therapeutic efficacy in clinical trials but should not be used in routine clinical practice. Regardless of the method(s) used, current response biomarkers focus on assessing disease progression rather than positively addressing therapy benefit. The clinical consequences of using progression criteria can be detrimental for patients, including "prolonged exposure to potentially ineffective medications" and "all patients potentially getting all drugs – often too late". Thus, currently available assessment methods can have negative impacts on oncologists' thinking regarding therapy choices for patients with metastatic bone disease. The case example of Anwar Padhani shows a potential new approach by using whole-body diffusion MRI which

is able to positively assess therapy effectiveness even when morphology is unhelpful. This case also highlights how image post-processing of diffusion data can help to increase confidence regarding the effectiveness of therapy in patients with predominantly bone disease.

### Future challenges

Clearly there are many professional challenges for incorporating advanced anatomic and multi-functional MRI methods into the care pathways of cancer patients as highlighted by many of the articles within this issue of MAGNETOM Flash. These include integration of the information of multiple individual tests all of which can be done at a single patient visit (new bioinformatics challenge), dealing with heterogeneity that exists between patients, between lesions (in the same patient) and within lesions (at baseline and in response to therapy). We also need to better understand the biology behind the image at multiple scales (physiology or pathologic processes, gene expression profiles, proteomics) and how imaging features correlate with other therapeutic efficacy biomarkers. An ongoing challenge is the need to

develop common measurements and analysis methods, uniform data displays and standardization across imaging vendor platforms. Documentation of reproducibility particularly across multiple centers also needs to be undertaken. Finally developing roadmaps for imaging biomarkers qualification and high precision medicine need to be developed. I hope you enjoy reading about the many new advances in oncologic MRI that we present to you in this magazine.



Anwar Padhani

- 1 Amit L, Ben-Aharon I, Vidal L, Leibovici L, Stemmer S. The impact of Bevacizumab (Avastin) on survival in metastatic solid tumors – a meta-analysis and systematic review. *PLoS One*. 2013;8(1):e51780.
- 2 Fine HA. Bevacizumab in glioblastoma – still much to learn. *N Engl J Med*. 2014; 20;370(8):764-5.

\*MAGNETOM 7T is ongoing research. All data shown are acquired using a non-commercial system under institutional review board permission. MAGNETOM 7T is still under development and not commercially available yet. Its future availability cannot be ensured.

## Editorial Board

We appreciate your comments.  
Please contact us at [magnetomworld.med@siemens.com](mailto:magnetomworld.med@siemens.com)



Antje Hellwich  
Editor-in-chief



Wellesley Were  
MR Business Development  
Manager Australia and  
New Zealand



Ralph Strecker  
MR Collaborations Manager,  
São Paulo, Brazil



Sven Zühlsdorff, Ph.D.  
Clinical Collaboration  
Manager, Chicago, IL, USA



Gary R. McNeal, MS (BME)  
Advanced Application  
Specialist, Cardiovascular  
MR Imaging Hoffman  
Estates, IL, USA



Peter Kreisler, Ph.D.  
Collaborations & Applications,  
Erlangen, Germany

## Review Board

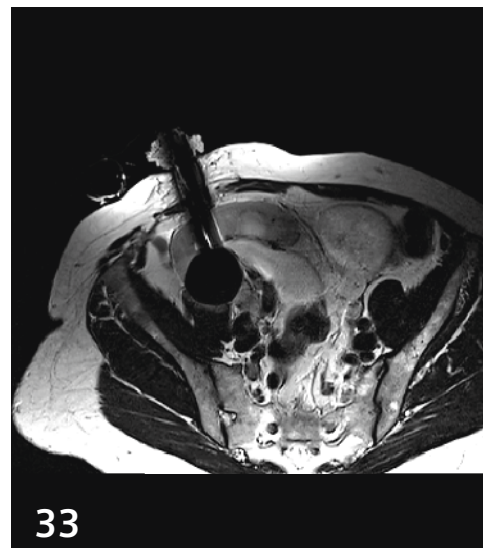
Lisa Chuah, Ph.D.  
Global Segment Manager Neurology  
Lars Drüppel, Ph.D.  
Global Segment Manager Cardiovascular MR  
Wilhelm Horger  
Application Development Oncology  
Michelle Kessler  
US Installed Base Manager  
Berthold Kiefer, Ph.D.  
Head of Oncological and Interventional  
Applications  
Sunil Kumar S.L., Ph.D.  
Senior Manager Applications  
Reto Merges  
Head of Outbound Marketing MR Applications  
Edgar Müller  
Head of Cardiovascular Applications  
Heiko Meyer, Ph.D.  
Head of Neuro Applications  
Gregor Thörmer, Ph.D.  
Global Segment Manager Men's and  
Women's Health & MR in Radiation Therapy  
Heike Weh  
Clinical Data Manager

# Content



8

A Dedicated MRI Scanner for Radiotherapy Planning



33

Minimally Invasive 3T Interventional MRI



## Learn from the experience of other MAGNETOM users

The MAGNETOM World is the community of Siemens MR users worldwide, providing you with relevant clinical information. Here you will find application tips and protocols to optimize your daily work. Lectures and presentations from experts in the field will allow you to be exposed to new ideas and alternative clinical approaches.

Put the advantages of the MAGNETOM World to work for you!

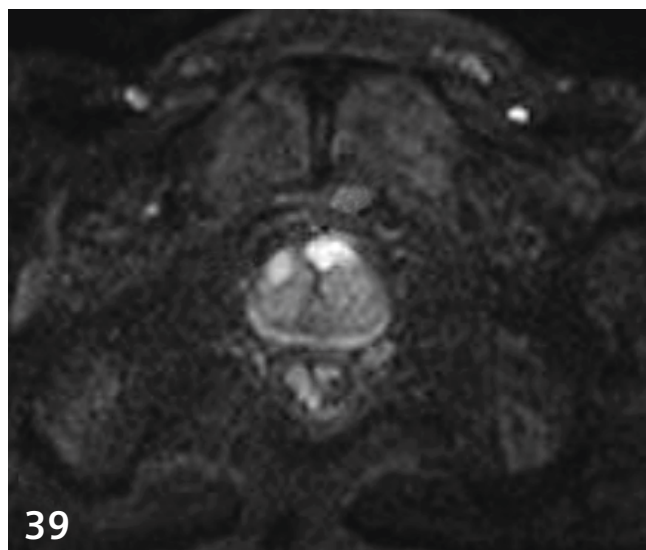
[www.siemens.com/magnetom-world](http://www.siemens.com/magnetom-world)

## Editorial

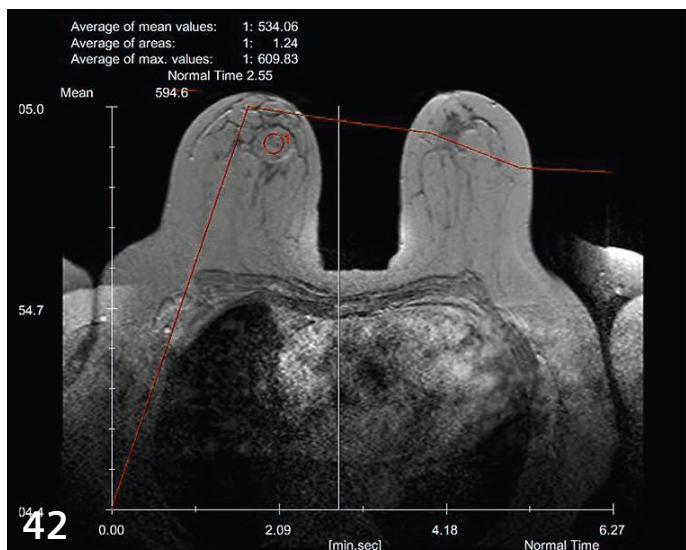
- 2 Advancing Cancer Care  
Anwar R. Padhani, Mount Vernon Cancer Centre, London, UK

## Therapy Planning

- 8 A dedicated MRI Scanner for Radiotherapy Planning  
Gary Liney, et al.,  
Liverpool Cancer Therapy Centre, Sydney, Australia
- 14 MR-Guided Gynecological High Dose Rate (HDR) Brachytherapy  
Joann I. Prisciandaro, Shruti Jolly, et al.,  
University of Michigan, Ann Arbor, MI, USA
- 20 fMRI in Presurgical Planning at 7T\*  
Simon Robinson, Roland Beisteiner, et al.,  
Medical University of Vienna, Austria



**39** High Resolution DWI of the Prostate using RESOLVE at 3T



**42** How Breast MRI Changed the Operative Management

## Therapy Monitoring

- 26** Monitoring Bone Marrow Metastases Treatment with Whole-Body Diffusion MRI  
*Anwar R. Padhani, Mount Vernon Cancer Centre, London, UK*

## Interventional MRI

- 30** Case Study: 3T MR Neurography Guided Posterior Femoral Cutaneous Nerve Block  
*Jan Fritz, John Morelli, Johns Hopkins School of Medicine, Baltimore, MD, USA*
- 33** Minimally Invasive 3 Tesla Interventional MR  
*Kemal Tuncali, Brigham & Womens, Hospital, Boston, MA, USA*
- 36** 3T Multiparametric MRI and MR-Guided In-Bore Biopsy to Detect Prostate Cancer  
*Lars Schimmöller, Dirk Blondin, et al., University Duesseldorf, Germany*

## Men's Health

- 39** High-Resolution DWI of the Prostate using syngo RESOLVE at 3T  
*Liang Wang, Liang Li, et al., Huazhong University, Wuhan, China*

## Women's Health

- 42** How Breast MRI Changed the Operative Management  
*Marymol Koshy, et al., Universiti Teknologi MARA, Malaysia*
- 46** <sup>18</sup>F-FDG PET/MRI as Compared with <sup>18</sup>F-FDG PET/CT. Initial Experiences in Patients with Metastatic Breast Cancer  
*Amy Melsaether, Linda Moy, et al., New York University School of Medicine, USA*

- 54** Clinical Multiparametric MR Imaging of Breast Tumors at 7T\*  
*Siegfried Trattnig, et al., Medical University of Vienna, Austria*
- 62** Can an Automated Decision Tree Based on Quantitative DCE-MRI Help to Accurately Classify Complex Adnexal Masses?  
*Hamidreza Sligheh Rad, et al., Tehran University of Medical Sciences, Iran*

## Pediatric Imaging\*\*

- 70** Case Study: Yolk Sac Tumor  
*Maren Asmussen; Peter Reimer, Karlsruhe City Hospital, Germany*

The information presented in MAGNETOM Flash is for illustration only and is not intended to be relied upon by the reader for instruction as to the practice of medicine.

Any health care practitioner reading this information is reminded that they must use their own learning, training and expertise in dealing with their individual patients. This material does not substitute for that duty and is not intended by Siemens Medical Solutions to be used for any purpose in that regard. The treating physician bears the sole responsibility for the diagnosis and treatment of patients, including drugs and doses prescribed in connection with such use. The Operating Instructions must always be strictly followed when operating the MR System. The source for the technical data is the corresponding data sheets.

\*MAGNETOM 7T is ongoing research. All data shown are acquired using a non-commercial system under institutional review board permission. MAGNETOM 7T is still under development and not commercially available yet. Its future availability cannot be ensured.

\*\*MR scanning has not been established as safe for imaging fetuses and infants under two years of age. The responsible physician must evaluate the benefit of the MRI examination in comparison to other imaging procedures.



# A Dedicated MRI Scanner for Radiotherapy Planning: Early Experiences

Gary Liney<sup>1,2</sup>; Robba Rai<sup>1</sup>; Lois Holloway<sup>1</sup>; Shalini Vinod<sup>1</sup>

<sup>1</sup>Liverpool Cancer Therapy Centre, Sydney, Australia

<sup>2</sup>Ingham Institute for Applied Medical Research, Sydney, Australia

## Introduction

The last decade has seen a dramatic increase in the use of MRI for radiotherapy planning. MRI has a number of advantages for the simulation of treatment plans, over the current gold standard of computed tomography (CT); Its excellent and variable soft-tissue contrast has been shown to improve the delineation accuracy

of both the tumor and surrounding organs-at-risk; a range of functional techniques are able to measure and display tumor physiology in the same examination, potentially revealing sub-regions that could receive a boost in radiation dose; and finally, the absence of ionising radiation means the patient may be scanned

any number of times before, during and after treatment, giving the clinician the ability to assess and adapt plans on an individual basis.

## MR-simulator

In common with most radiotherapy centres, our department at Liverpool Cancer Therapy Centre (LCTC), located



1

The 3 Tesla MAGNETOM Skyra MR-Simulator at Liverpool CTC, in south western Sydney, Australia. The 30 Gauss line can be seen marked on the floor which serves to emphasise this inner controlled area for the majority of our staff who have not previously worked in MRI. The object on the bed is our 3D volumetric distortion test phantom.



**2** Photographs showing the RF coil set-up used in head and neck planning scans. **(2A)** Two small flexible coils are placed laterally around the fixation shell using two coil supports. **(2B)** The 18-channel body array is connected to one of the available ports at the bottom of the table using a long cable.

in south western Sydney, relied heavily on local radiology scanners to provide MR images. This often meant a compromise in image protocol and the limited availability of these busy scanners restricted our patient throughput and any opportunity for further development. However, in August 2013, as part of a wider investment in MRI, which will also see the Australian MR-Linac program on site, we installed our own dedicated system for the exclusive use of radiotherapy patients to provide MR-based treatment simulation scans. This scanner is a wide-bore 3 Tesla MAGNETOM Skyra with XQ gradients and 64-channel RF architecture and was purchased with the latest suite of functional imaging sequences. Our MR-Simulator (MR-sim), shown in Figure 1, is configured with a number of radiotherapy-specific features in mind including in-room lasers (as on a CT-simulator), flat indexed table top and a range of RF coils suitable for optimum imaging with the patients in the treatment position. The field strength was chosen with aspirations of incorporating functional studies into future clinical practice.

Over the last 12 months or so, our small but dedicated team has climbed a steep learning curve and implemented MR-based planning successfully into clinical practice for a variety

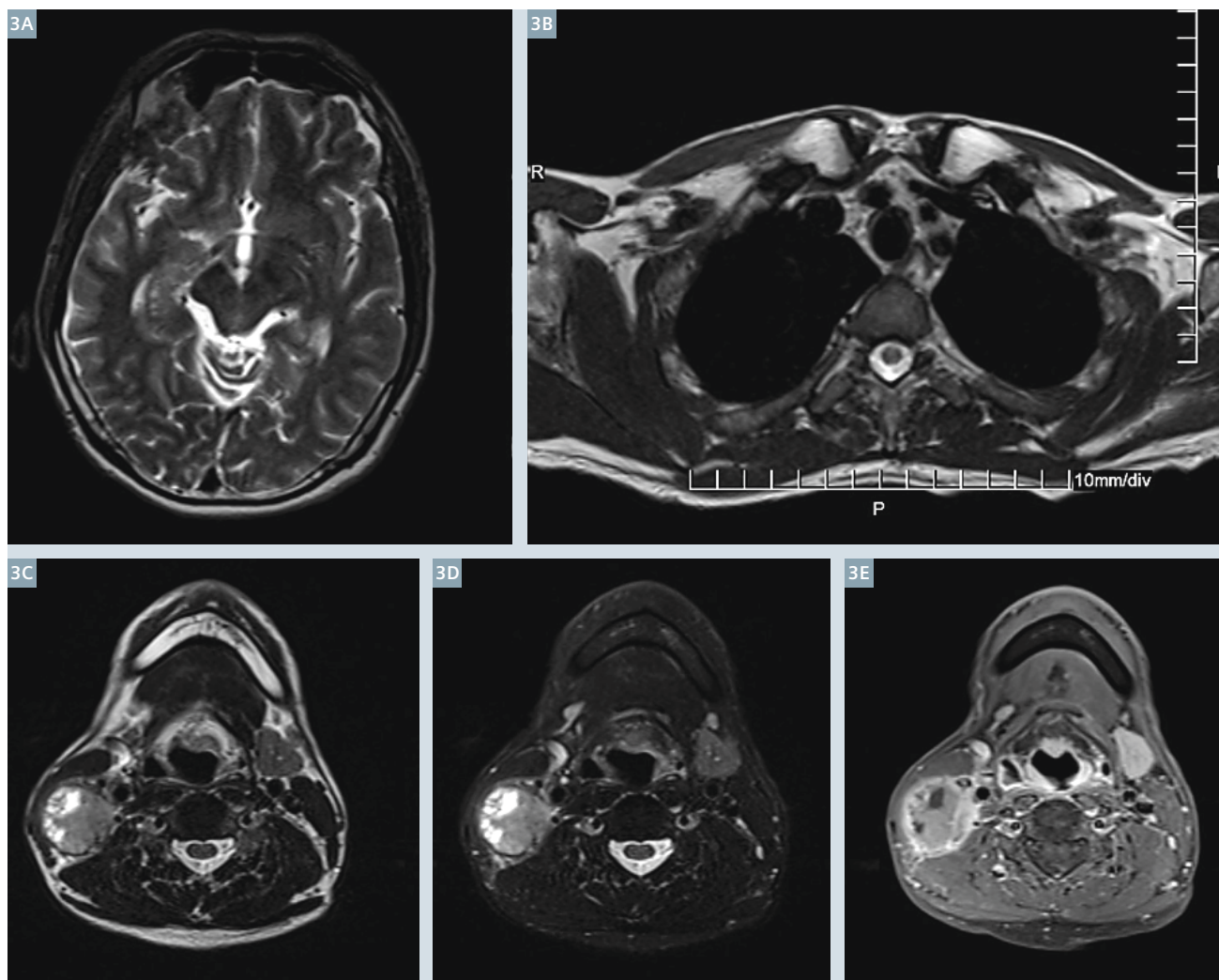
of tumor sites. This process began even before the installation and acceptance testing of the system, with in-house safety and educational training being implemented for all radiotherapy and physics staff connected with MRI. Under normal operation, scanning is performed by our lead MR radiographer and one of a small number of specialist radiotherapists who are rotated through MR-Sim. Additional support is provided by the lead MR physicist and a radiologist. By preserving a significant portion of scan time during the week for research – one of the many advantages of having our own system – we have also been able to develop a number of studies that are beginning to explore the use of functional information and motion evaluation in treatment planning. This article serves as a brief illustration of how we are using this system in practice.

The vast majority of our workload requires MRI to be registered to CT for the electron density information needed in the dose calculation. To facilitate this, we image our patients in the treatment position and take advantage of the RF coils we have available. A good example of this is in head and neck tumors where patients lie on a flat table top and are imaged

in a fixation shell placed over their head and shoulders which is attached to the table. Previous attempts to cater for this equipment on other scanners were compromised either due to a narrower 60 cm bore or unsuitable RF coils. On the MR-Sim we take advantage of the in-built 32-channel RF coil under the flat table-top and use this in conjunction with two laterally positioned 4-channel flexible coils attached to a supporting bridge. More recently we have been able to add an 18-channel body array connected at the foot of the table by a long cable (Fig. 2). This gives us vastly improved signal-to-noise ratio (SNR) and greater coverage compared to what had previously been possible as shown in Figure 3.

### Imaging details

In working up our protocols, we have had to consider the specific requirements of MR-simulation, which is often quite different from standard diagnostic procedure [1]. Geometric distortion is something we have to be especially mindful of. For radial distances less than 15 cm from isocentre (i.e. up to 30 cm FOV), system distortions caused by non uniformity in  $B_0$  and non linearity of the gradients are within our tolerance, and the dominant contribution is instead



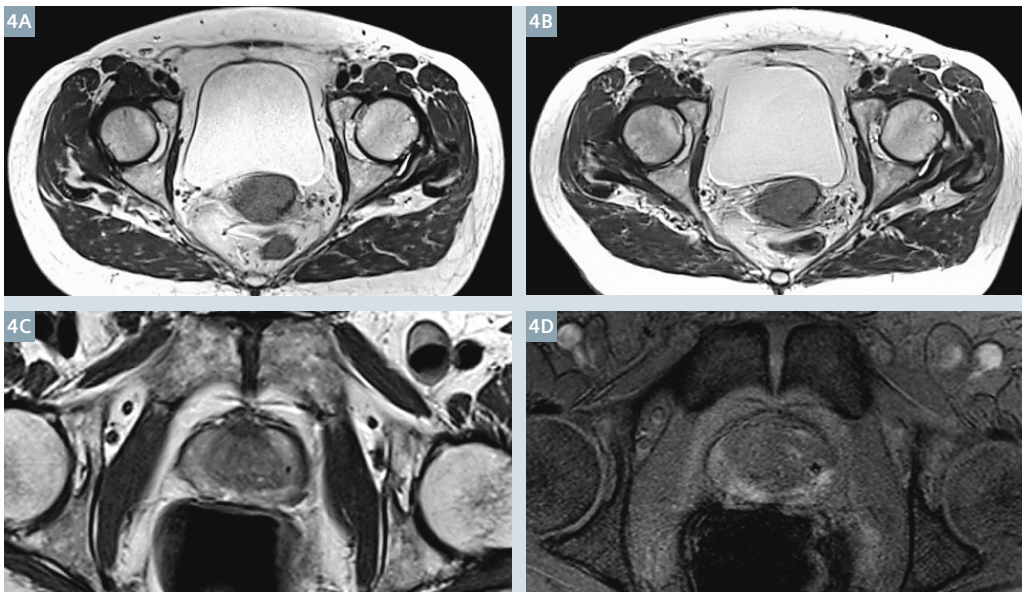
**3** Example images acquired in a head and neck tumor patient. Figures **3A** and **B** serve to illustrate the image quality and coverage obtained using dedicated RF coils which extend from midbrain down to sternal notch. The bottom images show a slice taken through the tumor using **(3C)** Dixon T2w in-phase, **(3D)** water-only and **(3E)** Dixon T1w water-only post-contrast.

from chemical shift and magnetic susceptibility within the patient. These effects can be mitigated by use of high receiver bandwidths which we set to 440 Hz/pixel or greater. The large coverage that is required for planning creates long scan times compared to diagnostic practice and we rely heavily on iPAT technology to keep these down to an acceptable level. Nevertheless, these scan times inevitably result in some organ motion and we have found BLADE to be useful in reducing artifacts for example from bladder filling. One of our current studies is comparing the image quality of this radial *k*-space technique against the administration of anti-peristaltic agents and normal cartesian acquisition as

shown in Figure 4A. Another particular interest for us is the development of a single planning scan for prostate patients with fiducial gold seeds. These exams would normally require two separate scans, a gradient-echo based sequence to identify the seed position and a second T2-weighted TSE for contouring the gland. The susceptibility artefact from the seed, while making them clearly visible, reduces positional accuracy, even with high bandwidths, and the requirement for two scans is less than ideal. However, we have begun looking at sequences such as turbo gradient spin-echo (TGSE) which offer the potential of combining both types of contrast into a single image (Fig. 4B).

To fully map out the geometric integrity of our system over large volumes, we have designed and built our own 3D phantom which covers 50 cm in each orientation (pictured in the magnet in Fig. 1). This test object has proved particularly useful in demonstrating the role of TimCT in cases when we have needed to exceed our 30 cm rule. By moving the patient through the bore while acquiring thin isocentric sections the distortion limit along the z-axis may be avoided altogether, thereby extending planning coverage. Figure 5 shows an example of this in a particularly difficult sarcoma case where more than 60 cm coverage was requested by the Oncologist and a total of 50 coil elements were used.





4

Developing body protocols for RT simulation; A comparison of BLADE (4A) versus anti-peristaltic agent (4B) as an effective control of organ motion artefacts. Use of the TGSE (4C) to provide a prostate planning scan that combines T2w contrast and gold seed visualization. (4D) Standard gradient-echo image used for seed localisation, which exaggerates the dimension of the marker.

## Therapy response

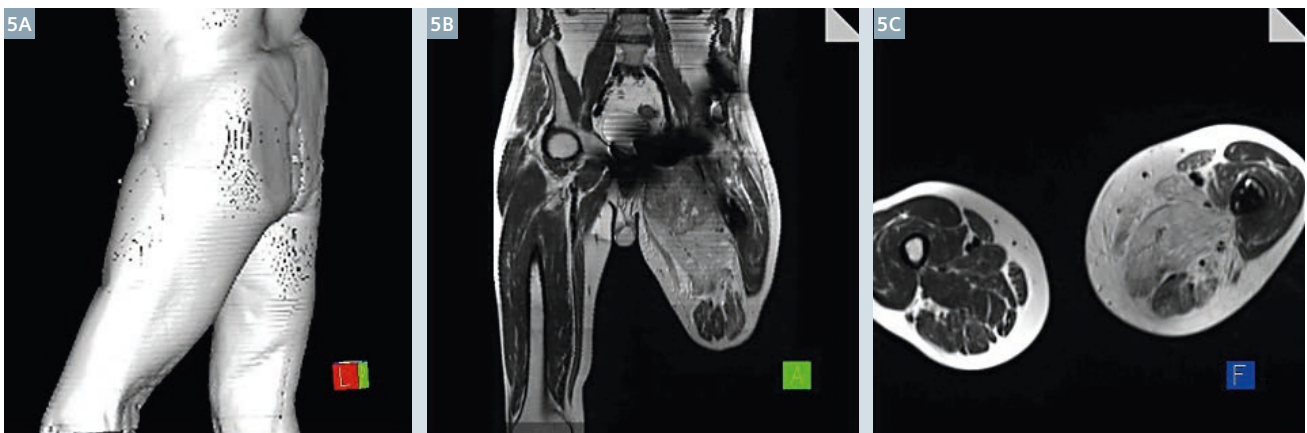
For most examinations we are using MRI at the commencement of treatment for its soft-tissue contrast and the improvement in planning contours. Alongside this routine work, we have begun several research studies that are using MRI to assess response over the course of treatment. These studies use both diffusion-weighted imaging (DWI) and dynamic contrast enhancement (DCE) to look at changes in tumor cellularity and vascularity respectively. In the case of diffusion, the commonly-used EPI sequence produces significant distortions and artifacts that has made its application in radiotherapy plan-

ning problematic. We have recently concluded a study that compared EPI with RESOLVE, which uses multi-segmentation in the frequency encoding direction combined with navigator self-correction, and showed improvements in ADC repeatability and geometric integrity compared to a T2-weighted gold standard [2]. Figure 6 shows a DWI example in a prostate patient acquired with  $b = 800 \text{ s/mm}^2$  together with the corresponding ADC map and we have now also adopted this sequence for rectum and cervix. As part of our DCE protocol we acquire pre-contrast

sequences at 2 and 15 degree flip angles to measure the native T1 prior to using dynamically acquired TWIST images. These scans are then analysed using the two compartment model which is available with the Tissue4D software.

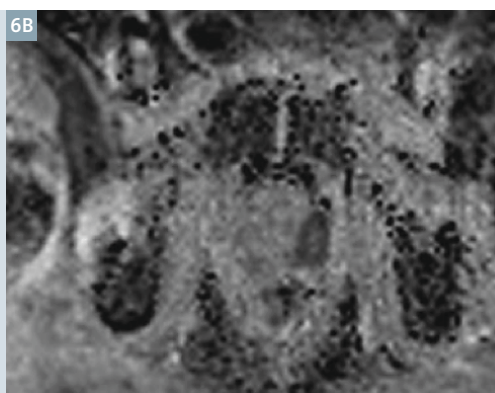
## Lung imaging

For our lung patients, we have developed an advanced imaging protocol providing a comprehensive assessment of anatomy, function and motion throughout their treatment (Fig. 7). For tumor contouring a T2-weighted HASTE sequence with a phase



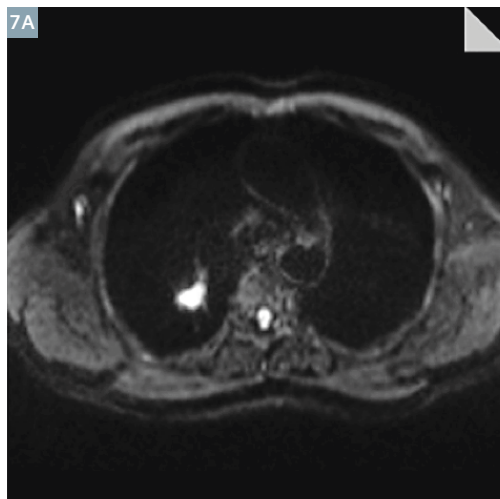
5

TimCT was used in this patient with a leg sarcoma and prosthesis *in situ* who could not straighten the effected leg. A full treatment simulation coverage of 61 cm in the head to foot direction was obtained by using the continuously moving table technique.



6

Diffusion-weighted imaging using the RESOLVE sequence in the prostate; **(6A)** A distortion free image with  $b = 800 \text{ s/mm}^2$  and **(6B)**, the resulting ADC map, both of which demonstrate an area of reduced diffusion in the left peripheral zone.



7

Example images from a lung tumor patient study; **(7A)** DWI with  $b = 500 \text{ s/mm}^2$  image, **(7B)** single frame from a coronal TrueFISP cine sequence acquired with cardiac shim, **(7C)** a late post-contrast enhanced TWIST image and **(7D)** axial HASTE acquired using a phase navigator.



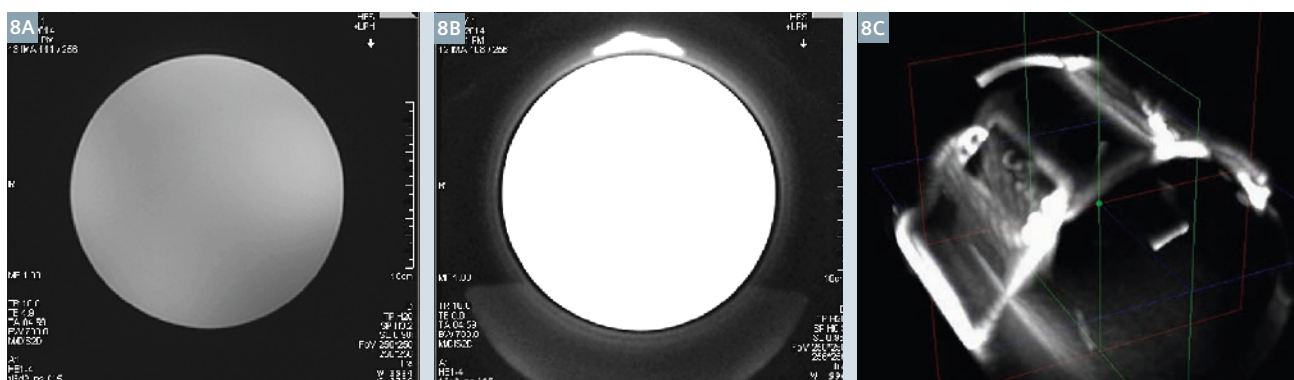
navigator placed in the liver dome is used to provide artefact free images. We then acquire a diffusion-weighted sequence to measure ADC, and cine TrueFISP scans during free breathing to assess tumor motion. The protocol is completed with a DCE TWIST sequence which is modified to acquire

a total of six separate short breath-hold windows from early first pass to 5 minutes post contrast. The incorporation of all this data is still in its infancy but we have already begun to use our own analysis to look at the tumor excursion and how it correlates with respiration.

## Conclusion

In the future, we anticipate that it will be possible to replace CT altogether in the majority of cases. In order to do this, one of the challenges will be the need to substitute CT and provide a surrogate for electron density. As part





**8** Examples of UTE imaging; **(8A, B)** Test object imaged at 4 ms displays signal from the fluid only but when this is repeated at 0.04 ms (40  $\mu$ s) a previously invisible lump of adhesive putty placed on top and the plastic cushion underneath can also be seen. **(8C)** 3D rendering of a processed dataset which demonstrates the RF coil itself (courtesy Jason Dowling, CSIRO).

of our research agreement with Siemens we are currently investigating the efficacy of ultrashort echo time (UTE) sequences to develop a strategy for MR-only planning\*. By bringing the TE down to tens of microseconds it becomes possible to obtain signal from materials and tissues that were previously invisible (Fig. 8). These images have the potential to provide more accurate substitute CT datasets as they can map cortical bone and even the RF coil itself which will be useful on the MR-Linac.

In summary, although it is still very much early days for us, the installation of a dedicated scanner in our department has been a great success and crucial in propelling MRI into our practice. We hope that in the not-too-distant future, MR-Sim will become a fairly standard sight in many radiotherapy centres throughout Australia and indeed the rest of the world. This will certainly help to establish a standardised approach for the implementation of MRI into radiotherapy so that the full benefit of this modality can be realised.

## Acknowledgements

We would like to acknowledge the following radiotherapists who make up the MR-Sim team: Lynnette Casapi, Ewa Juresic, Jim Yakobi & Callie Choong. Also thanks to Aitang Xing, Amy Walker (radiotherapy physicists), Mark Sidom and Dion Forstner (oncologists) and Daniel Moses (MR radiologist).

## References

- 1 GP Liney & MA Moerland. Magnetic resonance imaging acquisition techniques for radiotherapy planning, Sem Rad Onc in press, 2014.
- 2 GP Liney, T Al Harthi, E Juresic et al. Quantitative evaluation of diffusion-weighted imaging techniques for radiotherapy planning of prostate cancer. Proc ISMRM 2718: 2014.

\*WIP, the product is currently under development and is not for sale in the US and in other countries. Its future availability cannot be ensured.



## Contact

Conjoint Associate Professor Gary Liney (UNSW)  
Hon Principal Fellow, University of Wollongong  
Ingham Institute for Applied Medical  
Research & Radiation Oncology  
Liverpool Hospital, 1 Campbell Street  
Liverpool NSW 2170, Australia  
Phone: +61 2 8738 9221  
gary.liney@sswahs.nsw.gov.au



# MR-guided Gynecological High Dose Rate (HDR) Brachytherapy

Joann I. Prisciandaro<sup>1</sup>; James M. Balter<sup>1</sup>; Yue Cao<sup>1</sup>; Katherine Maturen<sup>2</sup>; Amir Owraangi<sup>1</sup>; Shruti Jolly<sup>1</sup>

<sup>1</sup>Department of Radiation Oncology, University of Michigan, Ann Arbor, MI, USA

<sup>2</sup>Department of Radiology, University of Michigan, Ann Arbor, MI, USA

## Introduction

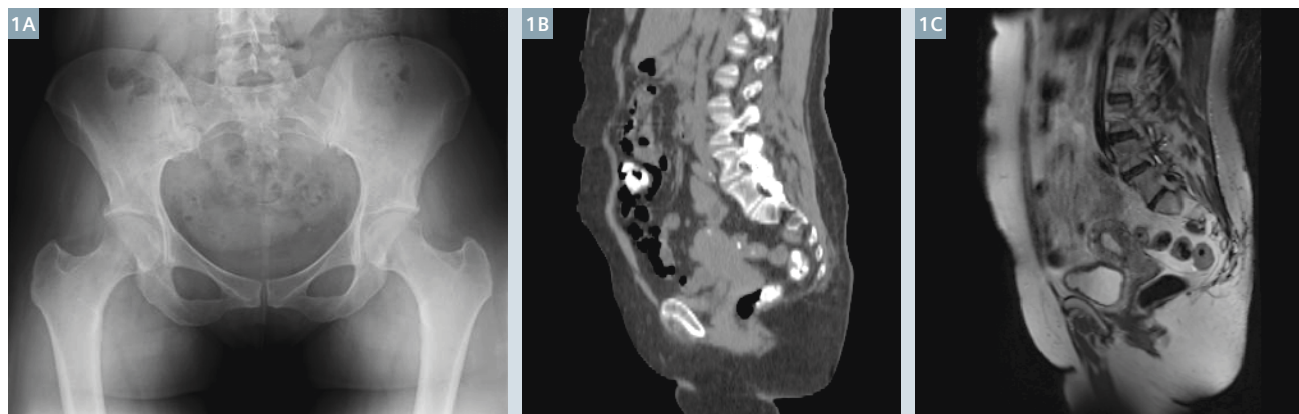
Brachytherapy is a form of radiation therapy that is delivered using sealed radioactive sources positioned in close proximity to tissues with cancer. The term derives from the Greek meaning short distance therapy. It is one of the original forms of radiation therapy, and emerged shortly after the discovery of radium in the early 1900's. Up until the 1990's, little had changed in the way brachytherapy treatments were planned and delivered. The nominal workflow consisted of the selection and *in vitro* placement of the appropriate applicator (a device that contains the radioactive source(s)), acquisition of 2D radiographic images to determine the position of the applicator and sources relative to the patient's anatomy, determination of the desired dose to the cancerous tissues and dose limits to neighboring normal tissues, and development of a treatment strategy to deliver the dose. The last two steps are iterative, as one tries to optimize the position and length of time the radioactive source(s) may reside in

the applicator to deliver the highest possible dose to the defined region of interest, while minimizing dose to neighboring normal tissues. However, 2D imaging presents limitations to the development of an optimal treatment plan. Although radiographs provide sharp subject contrast and detail between objects with highly varying attenuation, such as bone and air, the limited differences in attenuation between different types of soft tissue make them difficult to discern (Fig. 1A). As a result, brachytherapy treatment plans have traditionally been designed to deliver the desired dose to a geometrically defined reference point relative to the applicator to which anatomic significance is attached. This approach limits the ability to individualize the patient's radiation to their specific tumor and normal tissues.

In the 1990's, as computed tomography (CT) and magnetic resonance imaging (MRI) became more widely available at clinics and hospitals,

brachytherapy imaging began to transition from the use of planar to volumetric imaging. Unlike radiographs, volumetric images support some visualization of tumors and adjacent normal soft tissues (Figs. 1B, C). Compared to CT, MR images have the advantage of superior soft tissue resolution, and clear distinction of pelvic structures such as the uterus and cervix. Since local tumor control is strongly dependent on appropriately defined tumor volumes and the accurate delivery of radiation, the ability to visualize and delineate soft tissue is expected to improve target coverage and normal tissue sparing [1].

Beginning in 2000, GEC-ESTRO (the Groupe Européen de Curiethérapie – European Society for Radiotherapy & Oncology) recognized the significance of volumetric imaging in the movement toward 3D treatment planning for gynecological diseases, namely cervical cancer, with the formation of the gynecological (GYN) GEC-ESTRO work group [1]. In the fourteen years



**1** Example (1A) anterior pelvic radiograph [10], (1B) sagittal view of a pelvic CT simulation, and (1C) a sagittal reconstruction of a T2w 3D (SPACE) coronal image.

since its creation, the work group has released a series of recommendations to help standardize the approach to image-based brachytherapy treatment planning [1-4]. This has included the definition of a common language and means of delineating the target volumes (i.e., Low Risk-Clinical Target Volume (CTV), Intermediate Risk-CTV and High Risk-CTV for definitive treatment of cervix cancer), discussion on issues related to applicator reconstruction, and suggestions on the appropriate MR imaging sequences to utilize for treatment planning. Although these recommendations are helpful, there is a significant learning curve for each clinic during the clinical commissioning of MR-guided brachytherapy that is dependent on their specific MRI unit and brachytherapy applicators.

### MR-simulator

In 2012, a 3T wide-bore MRI-simulator was installed in the department of Radiation Oncology at the University of Michigan (MAGNETOM Skyra, Siemens Healthcare, Erlangen, Germany). This unit was purchased for the express purpose of complementing, and at times, replacing CT treatment simulations, and has been outfitted with a laser marking system (LAP, Lueneburg, Germany) and detachable couch [5]. The couch supports imaging and treatment of brachytherapy patients, eliminating the need to transfer patients to other tables and the risk of inadvertently modifying the local geometry of the applicator and surrounding tissues. The brachytherapy suite is directly across the hall from the MRI-simulator, and an access door and path was built into the room design to permit wheeling the couch directly to the treatment suite following scanning.

### Clinical commissioning

Prior to the clinical implementation of MR-guided brachytherapy, it is imperative to commission the process and workflow. Commissioning varies based on the desired treatment site, and involves the determination of the optimal imaging sequences for anatomical and applicator visualization. Care must be taken to ensure an MR conditional or compatible applicator is selected prior to the simulation. For treatment



2

Common brachytherapy applicators used for vaginal brachytherapy delivery, (2A) vaginal cylinder (Varian Medical Systems, Palo Alto, CA, USA) and (2B) ovoids (modified from the Fletcher Williamson Applicator Set, Nucletron/Elekta, Veenendaal, The Netherlands).

planning purposes, the images are imported into a software package (treatment planning system) that allows the user to identify the position of the applicator/potential source positions (a process known as applicator reconstruction) and the relevant patient anatomy. This software can then be used to optimize the length of time the radioactive source(s) should reside in various positions along the length of the applicator in order to deliver the desired dose and dose distribution to the patient. While the applicator, in particular the source channel (i.e., the hollow channel within the applicator where the source(s) may reside), is well-visualized in planar and CT imaging with the use of x-ray markers, this task is challenging with MRI. At present there are few MR markers that are commercially available to assist with applicator reconstruction. Additionally, the presence of the applicator, especially titanium applicators, produces image artifacts and distortions. Since dose calculations are dependent on the accurate definition of the applicator, namely the source position(s), relative to the patient's anatomy, geometrical uncertainties may result in dosimetric uncertainties to the target volume(s) and neighboring normal structures

[3]. Thus, it is critical to evaluate these uncertainties prior to the clinical implementation of MR-guided brachytherapy.

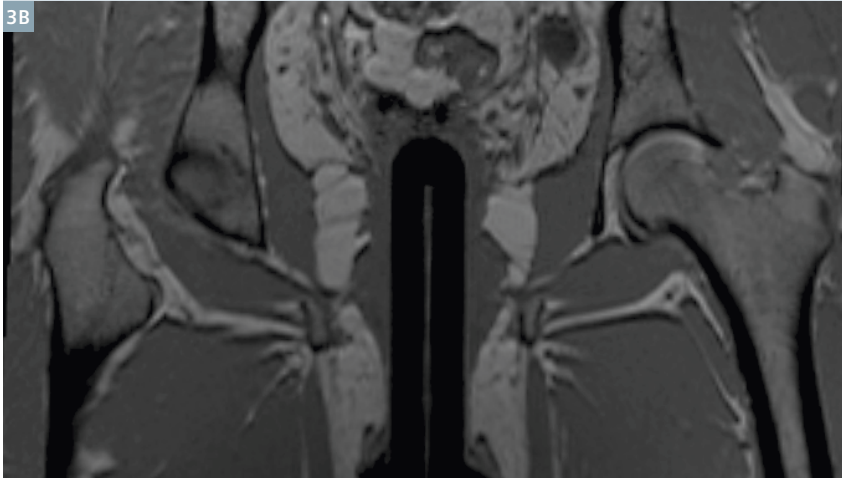
#### a. Vaginal high dose rate (HDR) brachytherapy

Clinically, vaginal brachytherapy is most often used in the adjuvant treatment of uterine cancer post hysterectomy to reduce the risk of cancer recurrence in the vagina. Vaginal brachytherapy can also be used for treatment of other gynecologic cancers, including cervix, primary vaginal and vulvar cancer as clinically indicated. The typical applicators used for the delivery of vaginal brachytherapy are the vaginal cylinder and ovoids [6] (see Fig. 2). A vaginal cylinder is typically a smooth, plastic cylinder with a dome shaped apex that is available in diameters ranging from approximately 2.0–4.0 cm, depending on the patient's anatomy. The applicator typically has a single, hollow channel that runs along the center of the device; however, multi-channel variants are also available. Ovoids are hollow egg or cylinder-shaped capsules that are inserted into a patient's vagina and pressed up against the cervix if present or apex of the vaginal vault. Whereas the ovoids may be used to treat the upper

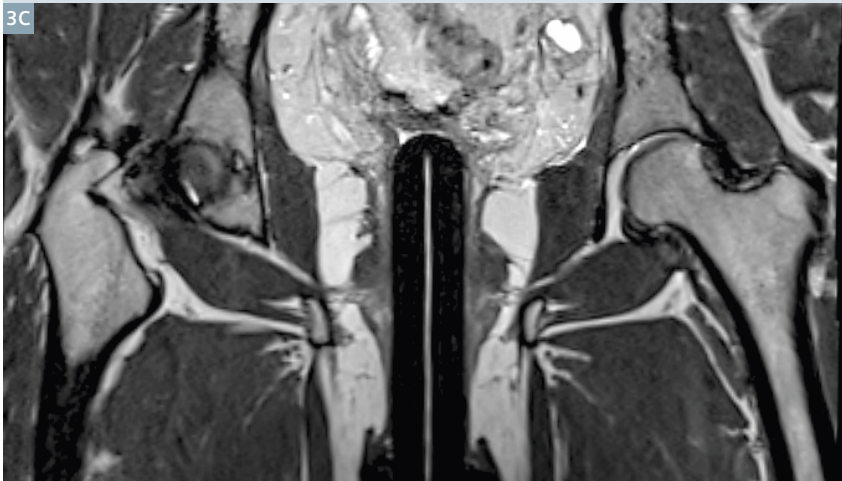
3A



3B



3C



**3** Coronal view of a patient with a vaginal cylinder on (3A) CT, (3B) 3D T1w (MPRAGE) MR, and (3C) 3D T2w (SPACE) MR. To assist with the visualization of the central source channel, the appropriate marker (x-ray for CT and contrast filled for MR) was inserted in the applicator prior to simulations.

The following MRI sequences were used: 3D T2 (SPACE) coronal (FOV  $320 \times 320 \times 176$  mm, voxel size  $0.94 \times 0.94 \times 1$  mm, TR 1700 ms, TE 88 ms) and 3D T1 (MPRAGE) coronal (FOV  $300 \times 300 \times 166.4$  mm, voxel size  $1.17 \times 1.17 \times 1.3$  mm, TR 1900 ms, TE 2.35 ms, TI 900 ms, flip angle  $9^\circ$ ). In order to identify the applicator channel, an MR marker was made in-house using a thin (0.046" outer diameter), hollow nylon tube (Best Medical International, Springfield, VA, USA) filled with gadolinium-doped water (T1 contrast) or either water or 0.2% Agarose Gel (T2 contrast), then sealed. Several different techniques were tested to seal the catheter ends including a heat seal with and without hot glue, bone wax with cyanoacrylate, and Water Weld™ with and without cyanoacrylate.

Although the applicator channel was easily visualized with the presence of the appropriate MR marker in both the T1w and T2w images as illustrated in Figures 3B and 3C, the applicator tip proved difficult to identify due to challenges in achieving a watertight seal. This resulted in observed displacements of the catheter tip, at times exceeding 1 cm. As such, an alternative method was investigated for applicator reconstruction using a solid model of the applicator available in the treatment planning software (BrachyVision 8.11, Varian Medical Systems, Palo Alto, CA, USA). Using T1w and/or T2w images, the solid model was aligned to the perimeter of the applicator (see Fig. 4). Deviations between the central source positions identified via aligning the applicator surface model to MR versus using the x-ray marker on CT to reconstruct the applicator (the conventional method) ranged from 0.07–0.19 cm and 0.07–0.20 cm for T1w and T2w images, respectively. Based on this study, vaginal brachytherapy patients at the University of Michigan now routinely undergo a single, T2w SPACE scan with approximately 1 mm isotropic voxel size. The applicator and related source positions for treatment planning are determined by alignment of the applicator model to the vaginal cylinder outline as observed on MRI.

portion of the vagina (known as the vaginal cuff), the vaginal cylinder offers the flexibility of treating the entire length of the vaginal vault [6].

During the clinical commissioning of MR-guided vaginal brachytherapy at the University of Michigan between August and September of 2013, three patients received a CT simulation preceding each HDR treatment

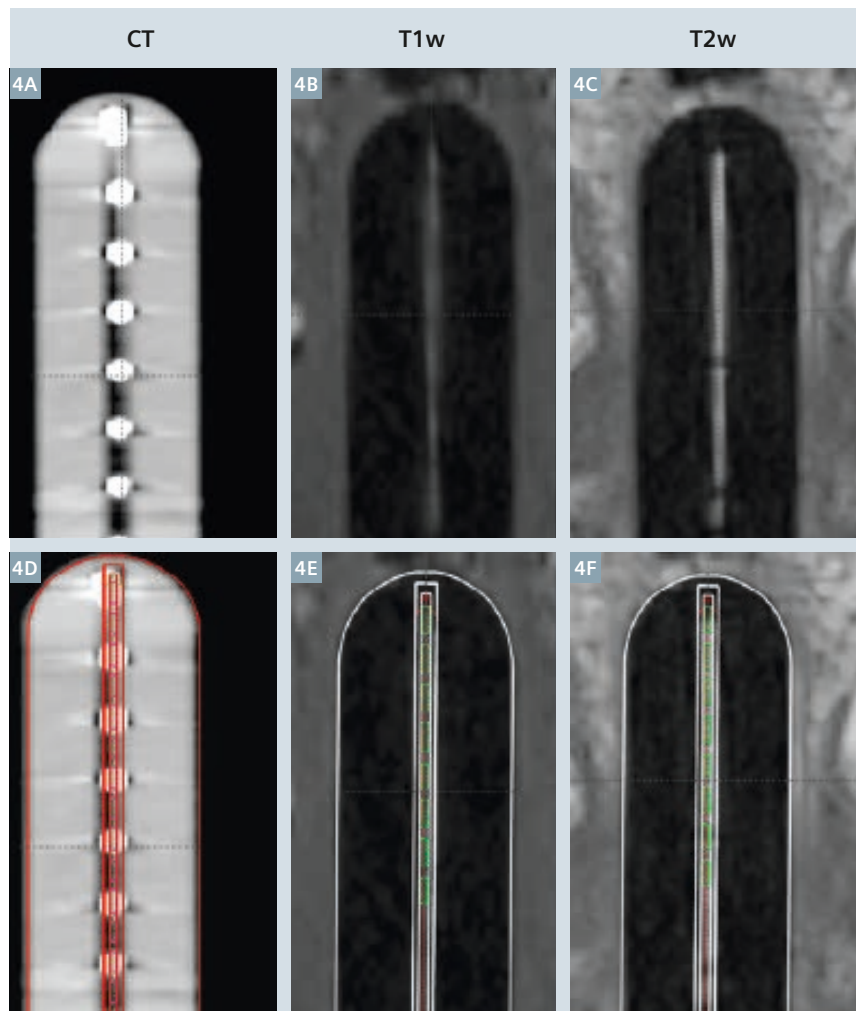
with a Philips Brilliance CT scanner (Philips Medical, Chesterfield, MO, USA), followed by an MRI simulation using a Siemens MAGNETOM Skyra 3T scanner. The patients were positioned supine with their legs straight. The CT scan was acquired with a 1 mm slice thickness with an x-ray marker in place (see Figure 3A). The MRI was acquired with T1 and T2-weighted 3D imaging sequences.



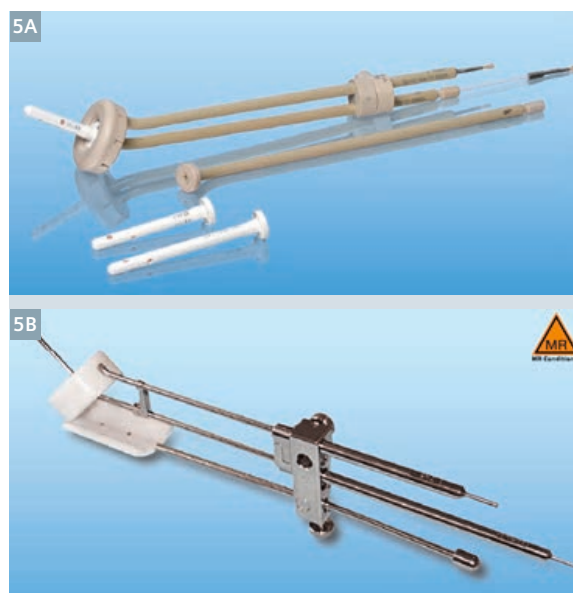
### b. Cervical HDR brachytherapy

While cervical cancer remains the most common gynecologic cancer world-wide, in the United States, the incidence of cervical cancer has decreased significantly since the widespread use of Papanicolaou (pap) smears in preventative care. Currently, approximately 12,000 new cases of cervical cancer are diagnosed per year. Treatment options are dependent on the stage of the disease upon clinical exam. Early stage cervical cancers are treated primarily by surgery. Occasionally, post-operative radiation or chemotherapy may be needed. When cervical tumors are not considered to be small enough to be removed by definitive hysterectomy, then curative or neoadjuvant radiation therapy with chemotherapy is the standard of care. In such situations, the patient undergoes combined external beam radiation with brachytherapy to provide high doses of radiation close to the tumor. Such treatments employ a variety of brachytherapy applicators. For most cases, the cervix can be treated using a combination of a tandem and ovoids, ring, or cylinder applicators [7]. However, when significant vaginal and/or parametrial involvement are present, then an interstitial brachytherapy implant may be needed to safely bring the required high doses of radiation to those areas.

At the University of Michigan, a plastic MR compatible ring and tandem applicator (GM11001220 and GM1100760, Varian Medical Systems, Palo Alto, CA, USA) has typically been used for HDR brachytherapy treatment of cervical cancer. This applicator system consists of an intrauterine catheter (tandem) and a circular, ring shaped device that allows the sealed source to be placed adjacent to the cervix (see Fig. 5A). During applicator commissioning which commenced in November 2013, 3D T2 (SPACE) sagittal images (FOV  $300 \times 300 \times 79.2$  mm, voxel size  $0.94 \times 0.94 \times 0.9$  mm, TR 1700 ms, TE 88 ms), 3D T1 (MPRAGE) sagittal images (FOV  $300 \times 300 \times 79.2$  mm, voxel size  $1.17 \times 1.17 \times 0.9$  mm, TR 1900 ms, TE 2.49 ms, TI 932 ms, flip angle  $9^\circ$ ), and multi-planar 2D T2w images at 2–3 mm slice thickness, were acquired with in-house MR markers in each applicator. Although the



4 Para-coronal view of the vaginal cylinder on (4A) CT, (4B) 3D T1w (MPRAGE) MR, and (4C) 3D T2w (SPACE) MR. Following alignment, the overlay of the solid applicator model is depicted for each imaging set in (4D–F).



5 The (5A) plastic and (5B) titanium ring and tandem applicator system used at the University of Michigan (Varian Medical Systems, Palo Alto, CA, USA).

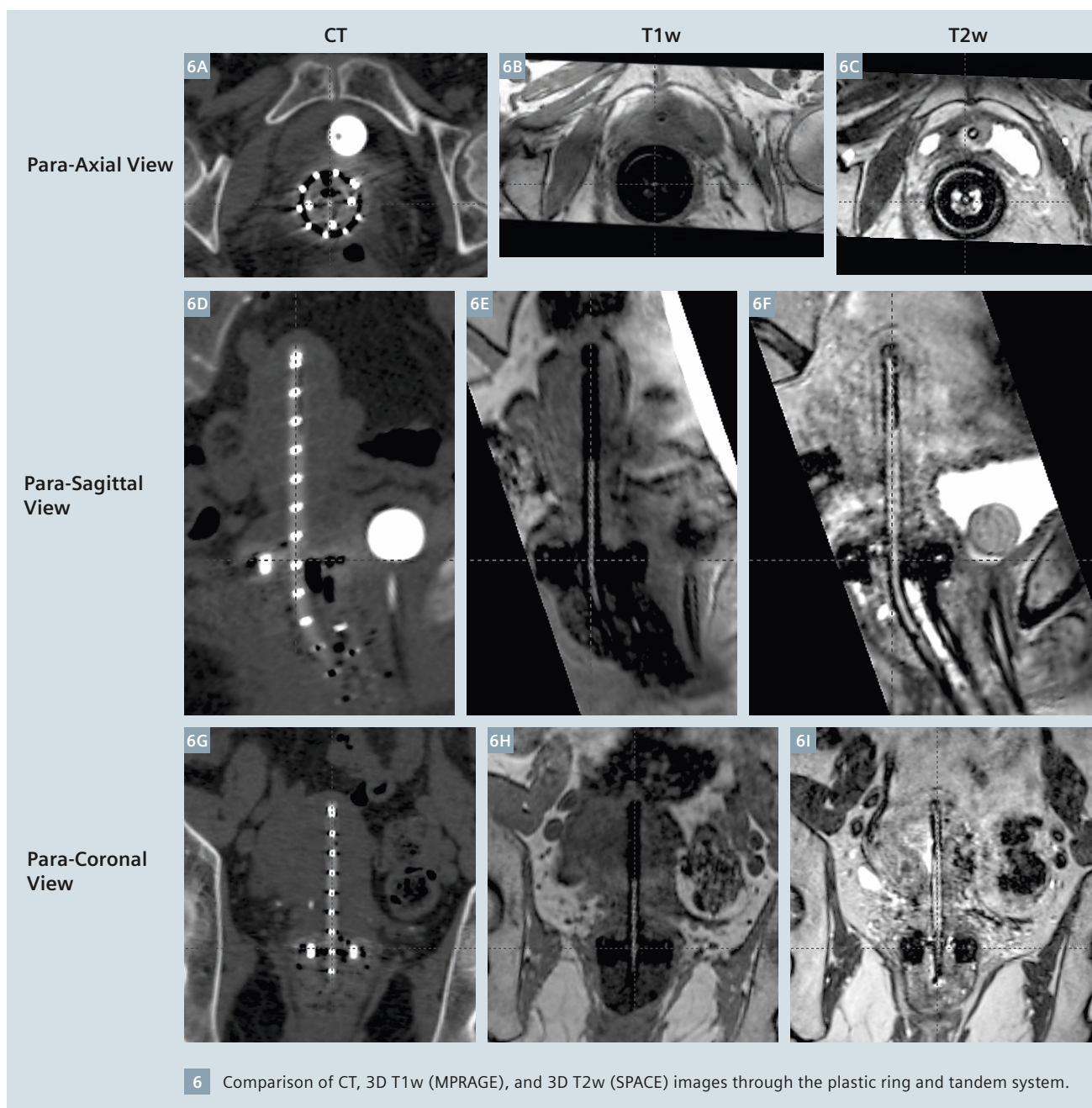
The MRI restrictions (if any) of the metal implant must be considered prior to patient undergoing MRI exam. MR imaging of patients with metallic implants brings specific risks. However, certain implants are approved by the governing regulatory bodies to be MR conditionally safe. For such implants, the previously mentioned warning may not be applicable. Please contact the implant manufacturer for the specific conditional information. The conditions for MR safety are the responsibility of the implant manufacturer, not of Siemens.

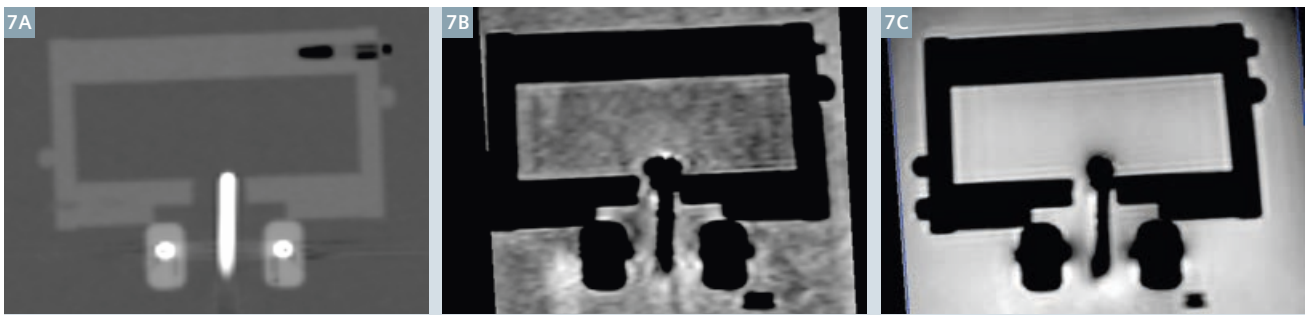
tip of the tandem and ring was not visualized reproducibly due to the compromised seal of the MR markers, the source path and MR marker was discernable on the T1w images (see Fig. 6). As a result of the significantly higher acquisition time for the T2w versus T1w images (nearly twice the scan time), the source channel and MR markers were blurred due to patient and organ motion on the T2w images (see Fig. 6). To minimize scan time, multi-planar 2D T2w images as well as a 3D T1 (VIBE) sagittal scan

with approximately 1 mm voxel size are acquired. Although the 2D T2w planar scans improve the quality of the resulting images, due to the large slice thickness of the 2D versus 3D MRI images, the MR marker was not visible on the 2D images. Therefore, 2D multi-planar T2w images as well as a small FOV 3D T2 (SPACE) sequence are acquired for soft tissue details, and 3D T1 (VIBE) sagittal images are acquired for applicator reconstruction. Prior to treatment planning, the registration of the T1w and T2w images

is verified. If significant patient motion is observed, the images are manually registered in the treatment planning software.

Unlike the vaginal cylinder, a solid applicator model was not available in the treatment planning system for the utilized plastic ring and tandem system. As such, a user defined library plan and applicator model was developed based on the CT reconstruction of the applicator. When a new treatment planning simulation is acquired, the library plan is imported, and the





**7** Comparison of (7A) CT, (7B) 3D T1w (MPRAGE), and (7C) 3D T2w (SPACE) sagittal images of the titanium ring and tandem system. The applicator set was scanned in a custom phantom designed to hold the applicator in a fixed position (based on [8, 9]). Prior to imaging, the phantom was filled with gadolinium-doped water. As compared to the CT image, magnetic susceptibility effects produce a mushroom effect off the tip of the tandem in the T1w and T2w images, resulting in uncertainties in the identification of the applicator tip on MRI.

applicator model is aligned based on the visible portions of the source channel, specifically focusing on the curvature of the tandem and/or ring.

Following a recent recall of the plastic ring and tandem system (PN BT-01366 Rev A, Varian Medical Systems, Palo Alto, CA, USA), a new titanium ring and tandem system (AL13017000, Varian Medical Systems, Palo Alto, CA, USA) has been purchased by the University of Michigan (see Fig. 5B). Due to susceptibility artifacts, the MR marker is not visible in the titanium applicator [8]. Additionally, these artifacts result in a mushroom effect

off the tip of the applicator, making it challenging to accurately identify the applicator tip on MR (see Fig. 7). Kim *et al.* [9] have reported this effect to be considerably smaller when using a small slice thickness (i.e., 1 mm) T1w versus T2w MRI. With the recent arrival of the titanium ring and tandem system at our institution, the clinical commissioning of this applicator set is currently in progress.

## Conclusions

MRI based image guided brachytherapy has the potential to significantly change the treatment planning pro-

cess. Soft tissue contrast allows the user to customize treatment plans to accurately deliver therapeutic doses to the region-of-interest, while minimizing dose to the normal structures in the vicinity of the tumor, potentially resulting in fewer treatment-related complications. However, the transition from point to volume-based planning requires the user to perform a thorough set of commissioning tests to determine the geometric uncertainties related to their imaging and the associated dosimetric uncertainties.

## References

- Haie-Meder C, R. Potter, E. Van Limbergen *et al.*, Recommendations from Gynaecological (GYN) GEC-ESTRO Working Group (I): concepts and terms in 3D image based 3D treatment planning in cervix cancer brachytherapy with emphasis on MRI assessment of GTV and CTV, *Radiotherapy & Oncology*, 2005;74:235-245.
- R. Potter CH-M, E. Van Limbergen *et al.*, Recommendations from gynaecological (GYN) GEC ESTRO working group (II): Concepts and terms in 3D image-based treatment planning in cervix cancer brachytherapy – 3D dose volume parameters and aspects of 3D image-based anatomy, radiation physics, radiobiology, *Radiotherapy & Oncology*, 2006;78:67-77.
- Hellebust TP, C. Kirisits, D. Berger *et al.*, Recommendations from Gynaecological (GYN) GEC-ESTRO Working Group: Considerations and pitfalls in commissioning and applicator reconstruction in 3D image-based treatment planning of cervix cancer brachytherapy, *Radiotherapy & Oncology*, 2010;96:153-160.
- Dimopoulos JCA, P. Petrow, K. Tanderup *et al.*, Recommendations from Gynaecological (GYN) GEC-ESTRO Working Group (IV): Basic principles and parameters for MR imaging within the frame of image based adaptive cervix cancer brachytherapy, *Radiotherapy & Oncology*, 2012;103: 113-122.
- Balter J, Y. Cao, H. Wang *et al.*, Optimizing MRI for Radiation Oncology: Initial Investigations, *MAGNETOM Flash*, 2013(April): 45-49.
- Small W, S. Beriwal, D.J. Demanes *et al.*, American Brachytherapy Society consensus guidelines for adjuvant vaginal cuff brachytherapy after hysterectomy, *Brachytherapy*, 2012;11:58-67.
- Viswanathan AN, and B. Thomadsen, American Brachytherapy Society consensus guidelines for locally advanced carcinoma of the cervix. Part I: General principles, *Brachytherapy*, 2012;11:33 - 46.
- Haack S, S.K. Nielsen, J.C. Lindegaard *et al.*, Applicator reconstruction in MRI 3D image-based dose planning of brachytherapy for cervical cancer, *Radiotherapy & Oncology*, 2009;91:187-193.
- Kim Y, M. Muruganandham, J. M Modrick *et al.*, Evaluation of artifacts and distortions of titanium applicators on 3.0-Tesla MRI: Feasibility of titanium applicators in MRI-guided brachytherapy for gynecological cancer, *Int. J. Radiation Oncology Biol. Phys.*, 2011;80(3):947-955.
- Jones, Jeremy. <http://images.radiopaedia.org/images/16912/7bb87421cbd7be3955346f5c27ef93.jpg>. Accessed June 29, 2014.

## Contact

Joann I. Prisciandaro, Ph.D.,  
FAAPM, Associate Professor  
Dept. of Radiation Oncology  
University of Michigan  
Ann Arbor, MI  
USA  
Phone: +1 (734) 936-4309  
[joann@med.umich.edu](mailto:joann@med.umich.edu)



Joann Prisciandaro



Shruti Jolly



# fMRI in Presurgical Planning at 7T

Simon Robinson<sup>1,3</sup>; Florian Fischmeister<sup>2,3</sup>; Eva Matt<sup>2,3</sup>; Roland Beisteiner<sup>2,3</sup>

<sup>1</sup>Department of Biomedical Engineering and Image-Guided Therapy, Medical University of Vienna, Austria

<sup>2</sup>Study Group Clinical fMRI, Department of Neurology, Medical University of Vienna, Austria

<sup>3</sup>High Field MR Center of Excellence, Medical University of Vienna, Austria

Functional Magnetic Resonance Imaging (fMRI) can be used to define brain regions which must be left intact when patients undergo surgery. Critical function is mapped with fMRI using a relevant task [1], generally presented in a simple block design and repeated a number of times. The localization of essential function needs to be reliable and accurate; some literature indicates that a shift of resection margins by only 1 mm close to eloquent brain areas may determine whether post-operative deficits are reversible or permanent [2].

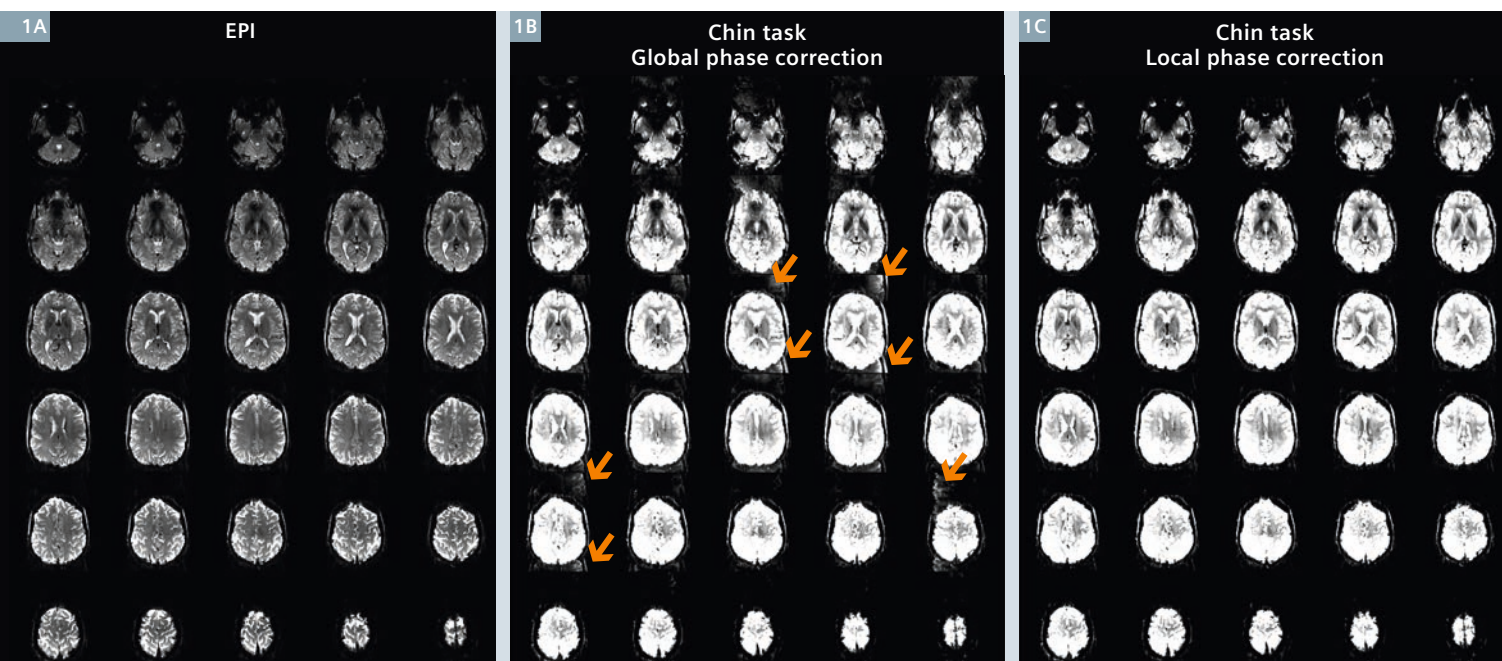
High signal-to-noise ratio (SNR) at ultra-high field provides elevated sensitivity to BOLD signal changes as

has been demonstrated both in healthy subjects [3, 4] and, more recently, patients [5]. Increased BOLD sensitivity allows resolution to be increased and very weak activation to be detected in previously undiagnosable patients with large and rapidly evolving tumors and complex pathologies. Improving the reliability of clinical fMRI through the use of ultra-high field and new acquisition methods offers the possibility to increasingly supplant invasive diagnostic procedures such as intraoperative cortical stimulation.

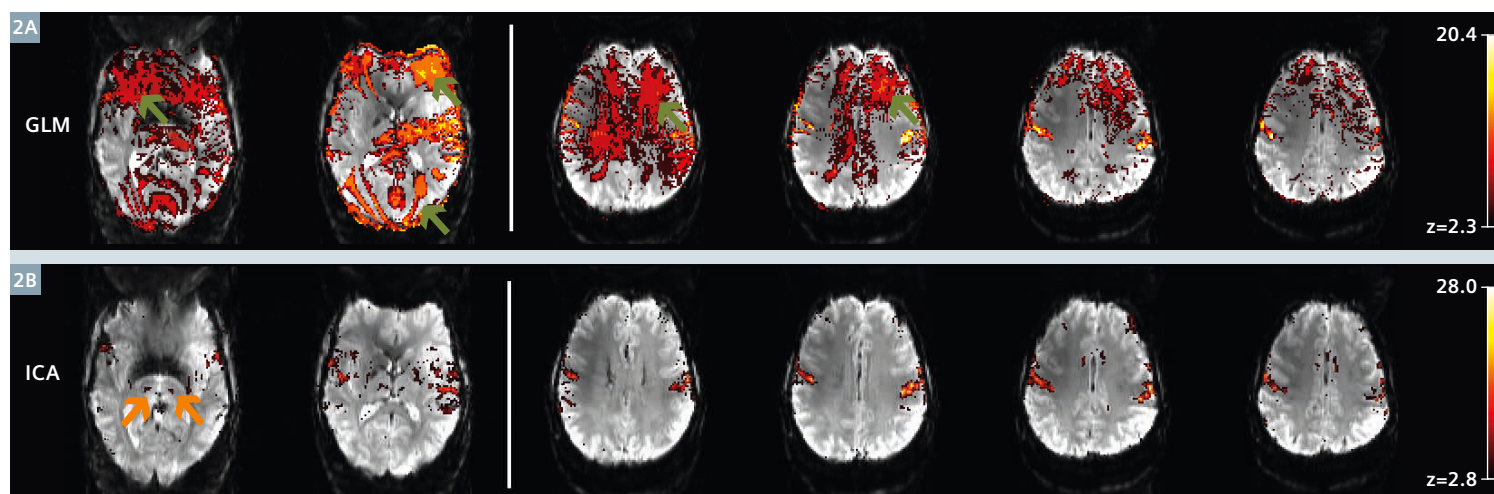
As in the high field (3-4T) regime, signal dropout in 7T\* EPI can be reduced by increasing resolution [6, 7] and using parallel imaging

acceleration [8, 9]. Parallel imaging reconstruction artifacts arising from motion and respiration either during the acquisition of GRAPPA reference lines (or Auto-Calibration Scans – ACS) or between acquisition of the ACS lines and the EPI time series can lead to serious reconstruction artifacts, particularly at very high field. Many clinical fMRI tasks are prone to generate motion, particularly motor foot and chin tasks, and language paradigms

\*MAGNETOM 7T is ongoing research. All data shown are acquired using a non-commercial system under institutional review board permission. MAGNETOM 7T is still under development and not commercially available yet. Its future availability cannot be ensured.



**1** Nyquist ghost reduction by robust phase correction. **(1A)** A single EPI time point acquired with parameters commonly used in presurgical planning [5]. **(1B)** The mean of the fMRI time series in which the subject performed a chin task (scaled to show Nyquist ghosts, indicated by arrows). **(1C)** The mean of the same fMRI time series reconstructed with an improved 'local' phase correction (scaling same as centre panel). Virtually no residual Nyquist ghost is visible.



**2** General linear model (GLM) results for a patient with a right frontal tumor are contaminated by motion artifacts (green arrows). The independent component analysis (ICA) component for this task networks shows no motion contamination, bilateral activation throughout primary motor areas and basal ganglia activation not apparent in GLM results.

involving overt speech [5, 10]. These parallel imaging artifacts can be reduced by acquiring the ACS lines with FLASH [11] or by acquiring all the segments required for each slice in rapid succession, with low flip angle – ‘FLEET’ [12].

Nyquist ghost artifacts are also more pronounced at higher field. The mean of an fMRI time series acquired during a chin task (which generates similar artifacts to those observed in clinical language paradigms involving overt speech) shows serious ghosting using a phase correction method which was standard in the product EPI sequence in earlier versions of *syngo* (Fig. 1B). We found ICA a useful means to isolate activation from stimulus-correlated artifacts in such data [10], as can be seen in Fig. 2.

It is far better to remedy the problem at source, however, and the development and implementation of a local phase correction (now as default in the product EPI), hugely reduces Nyquist ghosts (Fig. 1C).

A useful alternative approach to the problem of Nyquist ghosting is offered by the IDEA EPI sequence [13], in which every readout line is sampled twice; once with positive and once with negative readout gradient. The data from positive readouts and negative readouts are assigned to two

separate (usually undersampled) *k*-spaces. Avoiding the need to reverse alternate *k*-space line, this method yields images which are virtually ghost-free.

A recent development in EPI with enormous clinical potential due to the high temporal SNR per unit time is the ‘simultaneous multislice’ (SMS, a.k.a. ‘multiband’) approach, in which a number of slices are excited and read out simultaneously. Slice-dependent shifts in the image position in the blipped CAIPIRINHA approach make it possible to cleanly reallocate the overlapping signal in images to the correct slices, allowing the TR to be reduced by the SMS factor with very low g-factor penalty [14]. This approach was used in the results shown in Fig. 3.

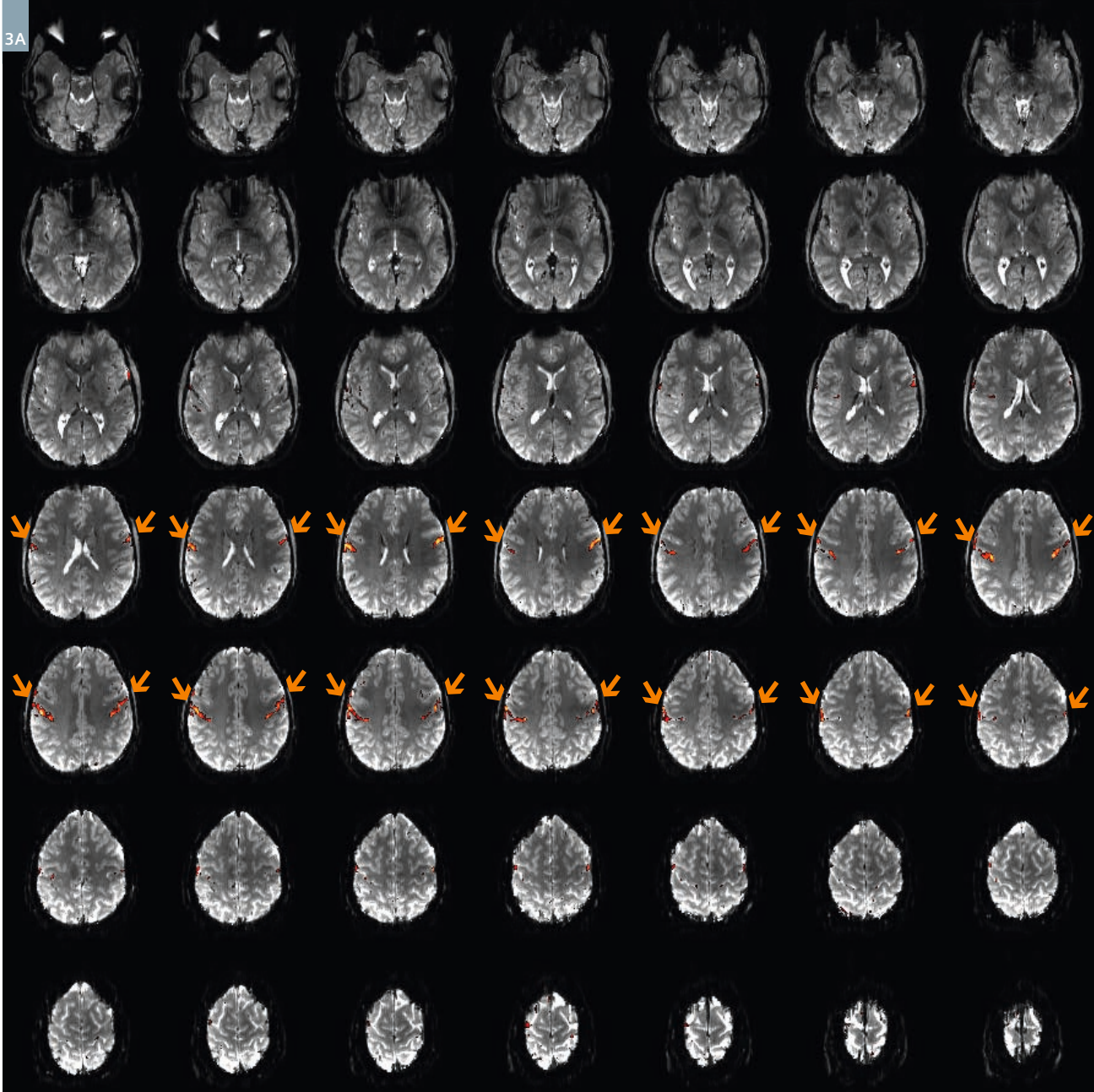
Geometric distortions of EPI scale proportionately with field strength. The clinical implications of image distortion depend on how analysis is performed. There is great divergence in analysis approaches in clinical fMRI, as there is in the neurosciences in general. For clinical reports, the local standard is to apply as little pre-processing as possible and perform all analysis in the native EPI space. If functional data is coregistered to individual anatomy, however, clinically relevant shifts in activation occur [15]. Even at 7T these can

be effectively corrected with multi-channel field mapping [16]. A residual confound occurs, however, when there is motion between the field map and the functional data. This motivates the development of dynamic approaches to distortion correction in which the field map is derived, or updated, from the fMRI data themselves [17].

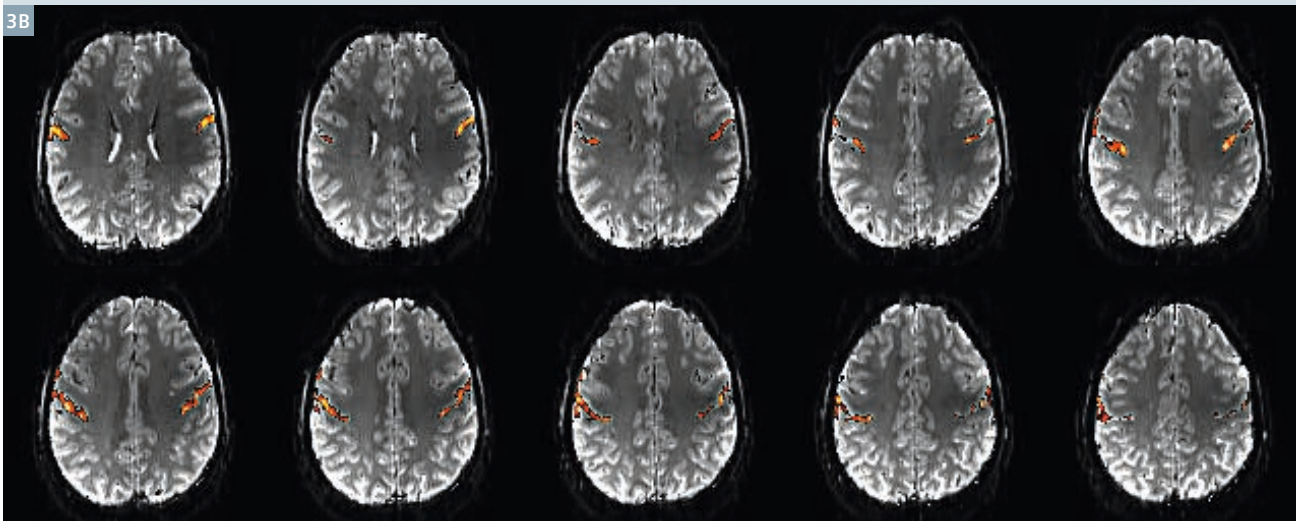
We end this description of methods of particular usefulness for ultra-high field clinical fMRI with an example of the quality of 7T fMRI data that is currently achievable with the approaches described. Five minutes of resting state EPI data was acquired from a single subject with a 7 Tesla MAGNETOM scanner using a 32-channel head coil (Nova Medical, Wilmington, MA, USA), with 50 slices of 1.5 mm isotropic resolution, using in-plane GRAPPA factor 2 and SMS factor 2, TE 22 ms, TR 1500 ms. Distortions were corrected using a multichannel field map [16]. ICA [18] reveals a component reflecting the motor resting state network [19] illustrated in Fig. 3, showing that reliable, high resolution mapping of primary motor regions is possible in just a few minutes, even in patients who are not able to perform a task [20, 21].



3A



3B



3

Fast, high-resolution mapping of primary motor areas using resting state functional connectivity (1.5 mm isotropic resolution, a single 5 minute run). Primary motor activation is highlighted on all slices (upper panel, at arrows) and selected slices are shown in the lower panel.



## Clinical application of 7T fMRI: An example from presurgical planning

We compared BOLD response at 3T and 7T during a simple motor task in 17 patients referred for presurgical diagnosis in the first ultra-high clinical fMRI study [5]. There was increased activation within the primary motor hand area at 7T compared to 3T despite increased ghosting and motion artifacts.

While motor tasks typically elicit robust activations in well-defined cortical regions, cognitive tasks such as

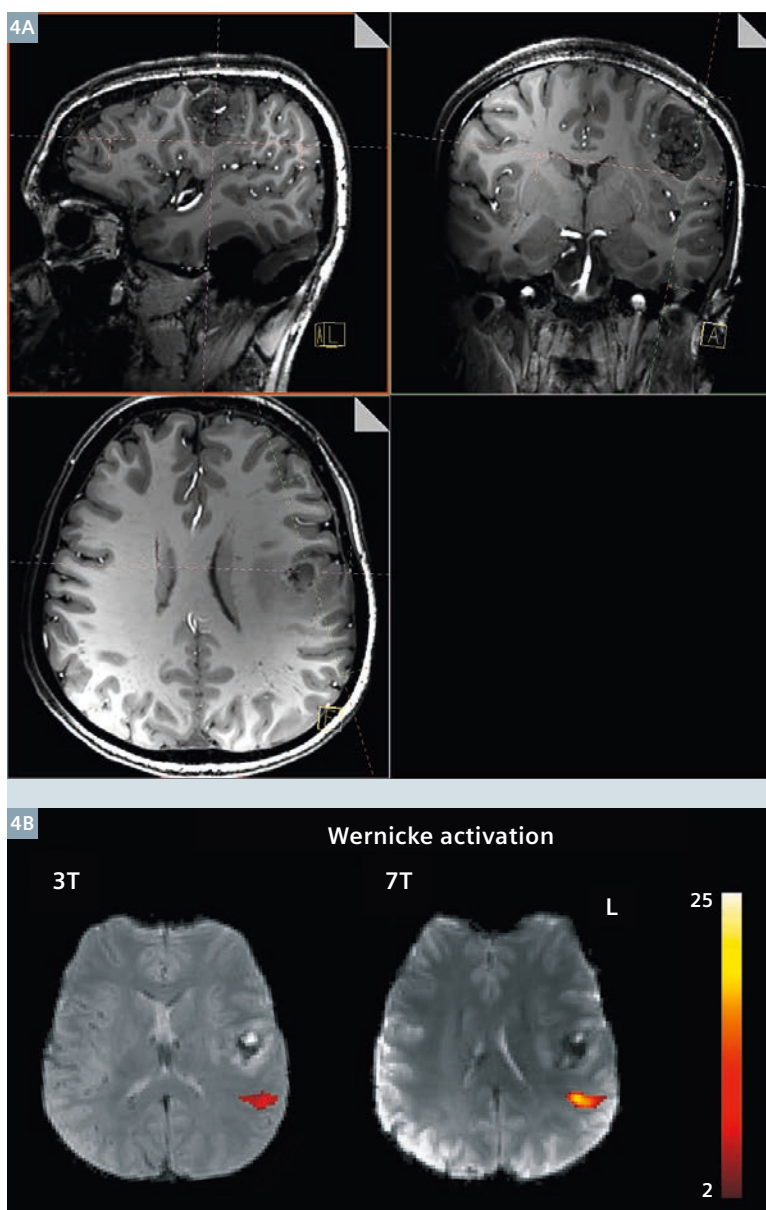
language evoke more complex activation patterns which often involve more problematic inferior frontal regions. There is significantly improved functional sensitivity in Wernicke's area at 7T compared to 3T as in the example in Fig. 4 of a 28-year-old patient with a left temporo-parietal tumor (the clinical language localization indicated left dominance in Wernicke and Broca). Contrary to the situation in Wernicke's area, there was no improvement in signal or activation statistics in Broca area at 7T because of increased signal loss [22].

We anticipate improvements in 7T results in such problematic regions with developments in coils and shimming, as well as more robust GRAPPA reconstruction and physiological noise correction methods.

## Clinical application of 7T fMRI: Outlook

Ultra-high field fMRI with high spatial and temporal resolution is particularly useful when investigating pathological alterations of neuronal tissue – tumors, lesions and neurodegeneration may weaken activation strengths as the vascular response is reduced [23]. This encourages the clinical use of 7T fMRI in presurgical functional localization, in assessing and monitoring neuroplasticity in various neuropathologies and in identifying non-invasive biomarkers for brain diseases. Moreover, higher sensitivity improves the detection of subtle differences between normal and pathological conditions, which is important for classification and prognosis in various neurological diseases (e.g. Alzheimer's disease).

The clinical importance of high sensitivity for weak functional activations also applies to the assessment and monitoring of neuroplastic changes in the cortex (e.g. tumor, stroke) as well as subcortical regions (e.g. Parkinson's disease, brainstem or cerebellar lesions) or peripheral nerve damage. The latter was investigated in patients suffering from a complete brachial plexus lesion who underwent a nerve reconstruction of the lesioned musculocutaneous nerve (innervating the biceps) via new inputs from the intact phrenic nerve (end to side connection) [24]. The healthy diaphragm area was able to add a new – phylogenetically not designed – function (moving the arm) to its already existing dedication (moving the diaphragm for breathing). Detecting such new types of neuroplasticity depends on the ability to monitor small brain activation changes. Ultra-high field fMRI was able to provide improved and earlier detection of neuronal reorganization.



4 MPRAGE of a patient with a tumor of unknown origin (4A) and activation in Wernicke's at 3T and 7T (4B), showing the improvement in functional statistics at ultra-high field.

Ultra-high field fMRI is opening up the possibility to study more subtle disruption and reorganization of function in an increasingly wide range of pathologies. The partnership between physicists and neurologists is essential to continue to realize the potential of ultra-high field fMRI and see it applied in the clinic.

## Acknowledgements

This work was funded by the Austrian Science Fund (FWF) project KLI264 and the "Vienna Advanced Clinical Imaging Center" (VIACLIC) project, part of the Vienna Spots of Excellence Program of the Center of Innovation and Technology, City of Vienna (ZIT), Austria.

### References

- Duffau, H., 2006. New concepts in surgery of WHO grade II gliomas: functional brain mapping, connectionism and plasticity – a review. *J Neurooncol* 79, 77-115.
- Haglund, M.M., Berger, M.S., Shamseldin, M., Lettich, E., Ojemann, G.A., 1994. Cortical localization of temporal lobe language sites in patients with gliomas. *Neurosurgery* 34, 567-576; discussion 576.
- Olman, C.A., Van de Moortele, P.F., Schumacher, J.F., Guy, J.R., Ugurbil, K., Yacoub, E., 2010. Retinotopic mapping with spin echo BOLD at 7T. *Magn Reson Imaging* 28, 1258-1269.
- van der Zwaag, W., Francis, S., Head, K., Peters, A., Gowland, P., Morris, P., Bowtell, R., 2009. fMRI at 1.5, 3 and 7 T: characterising BOLD signal changes. *NeuroImage* 47, 1425-1434.
- Beisteiner, R., Robinson, S., Wurnig, M., Hilbert, M., Merksa, K., Rath, J., Hollinger, I., Klinger, N., Marosi, C., Trattnig, S., Geissler, A., 2011. Clinical fMRI: Evidence for a 7T benefit over 3T. *NeuroImage* 57, 1015-1021.
- Merboldt, K.D., Finsterbusch, J., Frahm, J., 2000. Reducing inhomogeneity artifacts in functional MRI of human brain activation: thin sections vs gradient compensation. *J Magn Reson* 145, 184-191.
- Robinson, S., Pripfl, J., Bauer, H., Moser, E., 2008. The impact of EPI voxel size on SNR and BOLD sensitivity in the anterior medio-temporal lobe: a comparative group study of deactivation of the Default Mode. *MAGMA* 21, 279-290.
- Griswold, M.A., Jakob, P.M., Heidemann, R.M., Nittka, M., Jellus, V., Wang, J., Kiefer, B., Haase, A., 2002. Generalized autocalibrating partially parallel acquisitions (GRAPPA). *Magn Reson Med* 47, 1202-1210.
- Pruessmann, K., Weiger, M., Scheidegger, M., Boesiger, P., 1999. SENSE: sensitivity encoding for fast MRI. *Magn Reson Med* 42, 952-962.
- Robinson, S.D., Schopf, V., Cardoso, P., Geissler, A., Fischmeister, F.P., Wurnig, M., Trattnig, S., Beisteiner, R., 2013. Applying independent component analysis to clinical fMRI at 7 T. *Front Hum Neurosci* 7, 496.
- Talagala, S.L., Sarlls, J.E., Inati, S.J., 2013. Improved temporal SNR of accelerated EPI using a FLASH based GRAPPA reference scan. Proceedings of the Twenty-Third Annual Meeting of the ISMRM, Utah, U.S.A #2658.
- Polimeni, J., Bhat, H., Benner, T., Feiweier, T., Inati, S., Thomas, W., Heberlein, K., and Wald, L., 2013. Sequential-segment multi-shot auto-calibration for GRAPPA EPI: maximizing temporal SNR and reducing motion sensitivity. Proceedings of the Twenty-Third Annual Meeting of the ISMRM, Utah, U.S.A #2646.
- Poser, B.A., Barth, M., Goa, P.E., Deng, W., Stenger, V.A., 2013. Single-shot echo-planar imaging with Nyquist ghost compensation: interleaved dual echo with acceleration (IDEA) echo-planar imaging (EPI). *Magn Reson Med* 69, 37-47.
- Setsompop, K., Gagoski, B.A., Polimeni, J.R., Witzel, T., Wedeen, V.J., Wald, L.L., 2012. Blipped-controlled aliasing in parallel imaging for simultaneous multislice echo planar imaging with reduced g-factor penalty. *Magn Reson Med* 67, 1210-1224.
- Dymerska, B., Fischmeister, F., Geissler, A., Matt, E., Trattnig, S., Beisteiner, R., Robinson, S.D., 2014. Clinical Relevance of EPI distortion Correction in Presurgical fMRI at 7 Tesla. Proceedings of the Twenty-third Annual Meeting of the ISMRM, Milan, #1416.
- Robinson, S., Jovicich, J., 2011. B0 mapping with multi-channel RF coils at high field. *Magn Reson Med* 66, 976-988.
- Dymerska, B., Poser, B., Bogner, W., Visser, E., Cardoso, P., Barth, M., Trattnig, S., Robinson, S.D., 2014. Dynamic correction of geometric distortions in EPI: "CURED". Proceedings of the Twenty-third Annual Meeting of the ISMRM, Milan, #866.
- Beckmann, C.F., Smith, S.M., 2004. Probabilistic independent component analysis for functional magnetic resonance imaging. *IEEE Trans Med Imaging* 23, 137-152.
- Biswal, B., Yetkin, F.Z., Haughton, V.M., Hyde, J.S., 1995. Functional connectivity in the motor cortex of resting human brain using echo-planar MRI. *Magn Reson Med* 34, 537-541.
- Shimony, J.S., Zhang, D., Johnston, J.M., Fox, M.D., Roy, A., Leuthardt, E.C., 2009. Resting-state spontaneous fluctuations in brain activity: a new paradigm for presurgical planning using fMRI. *Acad Radiol* 16, 578-583.
- Zhang, D., Johnston, J.M., Fox, M.D., Leuthardt, E.C., Grubb, R.L., Chicoine, M.R., Smyth, M.D., Snyder, A.Z., Raichle, M.E., Shimony, J.S., 2009. Preoperative sensorimotor mapping in brain tumor patients using spontaneous fluctuations in neuronal activity imaged with functional magnetic resonance imaging: initial experience. *Neurosurgery* 65, 226-236.
- Beisteiner, R., Wurnig, M., Fischmeister, F., Matt, E., Knosp, E., Feucht, M., Auff, E., Trattnig, S., Robinson, S., Geissler, A., 2013. Are there benefits of ultra-high field MR for clinical language localization? *Journal of the neurological sciences* 333, e621.
- Ulmer, J.L., Haein-Bey, L., Mathews, V.P., Mueller, W.M., DeYoe, E.A., Prost, R.W., Meyer, G.A., Krouwer, H.G., Schmainda, K.M., 2004. Lesion-induced Pseudodominance at Functional Magnetic Resonance Imaging: Implications for Preoperative Assessments. *Neurosurgery* 55, 569-581.
- Beisteiner, R., Hollinger, I., Rath, J., Wurnig, M., Hilbert, M., Klinger, N., Geissler, A., Fischmeister, F., Wober, C., Klosch, G., Millesi, H., Grisold, W., Auff, E., Schmidhammer, R., 2011. New type of cortical neuroplasticity after nerve repair in brachial plexus lesions. *Arch Neurol* 68, 1467-1470.



Simon Robinson



Roland Beisteiner

## Contact

Assoc. Prof. Dr. Simon Robinson  
High Field Magnetic Resonance  
Centre  
Medical University of Vienna  
Lazarettgasse 14  
A-1090 Vienna, Austria  
Phone: +43-1-40400-6468  
simon.robinson@meduniwien.ac.at

# Expert Talks

Don't miss the talks of experienced and renowned experts on all aspects of MR imaging.



## MRI Technology and Methodology: A Look into the Future

**Peter Jezzard**  
University of Oxford (Oxford, UK)



## Whole-Body MRI: Changing Cancer Patient Management

**Anwar R. Padhani**  
Mount Vernon Cancer Centre (London, UK)



## Cartilage Evaluation

**Darshana Sanghvi**  
Kokilaben Dhirubhai Ambani (Mumbai, India)



## A 5 Minute Clinical Brain Protocol

**Lawrence Wald**  
Massachusetts General Hospital (Boston, MA, USA)



## Body MRI and Whole-Body Staging in Pediatric\* Patients

**Günther Schneider**  
Saarland University Hospital (Homburg, Germany)

Visit us at

[www.siemens.com/magnetom-world](http://www.siemens.com/magnetom-world)

Go to

**Clinical Corner > Clinical Talks**

\*MR scanning has not been established as safe for imaging fetuses and infants under two years of age.  
The responsible physician must evaluate the benefit of the MRI examination in comparison to other imaging procedures.



# Monitoring Bone Marrow Metastases Treatment with Whole-Body Diffusion MRI

Anwar R. Padhani, MB BS, FRCP, FRCR

Mount Vernon Cancer Centre, London, UK

Metastatic bone disease is a common manifestation of advanced cancers, with autopsy studies indicating a high prevalence in breast, prostate and lung cancers. Osteolytic metastases in particular cause bone and compressive nerve pain, impairs mobility, results in pathological fractures and causes spinal cord compression.

Other consequences of bone metastases include anemia and symptoms related to hypercalcemia. Once bony metastases have occurred, cancer cure becomes impossible and therapy is instituted with a palliative intent. Bone metastases therapies are a priority for development with many recent introductions into the clinic of active treatments for a variety of tumor types. Systemic therapies aimed at the bone matrix and tumor cells are administered for disseminated disease. Local treatments are used to control pain and to treat/prevent local complications.

## Skeletal therapy assessment tools

Accurate response evaluations of patients with bone metastases are notoriously difficult to perform because measureable bony soft tissue disease occurs infrequently. Symptom assessments and the development of skeletal-related events are preferred markers of therapeutic efficacy in clinical trials. More objectively, response can be gauged by a combination of imaging and clinical findings often used in combination with serum and urine biochemical markers of tumor burden and bone turnover. Serum tumor markers of response are not available or are ineffective for the vast majority of tumors that metastasize to bone.

Regardless of the method(s) used, current response biomarkers focus on assessing disease progression rather than positively addressing therapy benefit. Currently available assessment methods can have negative impacts on oncologists' thinking regarding therapy choices for patients with metastatic bone disease. <sup>99m</sup>Tc-MDP bone scans are the commonest imaging method for the follow-up of bone metastases. Unfortunately, bone scintigraphy informs only on the osseous/osteoblastic component of bone (not on the bone marrow). Drug trials utilizing bone scans have criteria for progression (two categories only: no new lesions/new lesions) but not for response. To mitigate against healing flare reactions, apparent progression needs to be confirmed by follow-up bone scans when new focal 'hot spots' have to be documented. Patients with diffuse metastatic bony disease and bone superscans cannot be followed for progression. Furthermore, the need to defer the decision of progression raises the issue of timeliness of the bone scan readouts for guiding clinical decision making.

A number of MRI sequences can evaluate bone for metastasis response assessments. Morphologic response criteria have been described for morphologic sequences [1]. However, a number of problems have also been noted including (1) arrested resolution of abnormalities despite effective therapy, (2) evaluating disease activity on scarred background is problematic (progression can only be documented on previously uninvolved marrow), (3) T1 – pseudoprogression due to bone edema, (4) the sclerotic progression phenomenon and, (5) mixed response patterns.

Therapy assessments on whole-body diffusion-weighted MR imaging (WB-DWI) are made by observing changes in the volume and symmetry of signal intensity abnormalities on high b-value images together with changes in ADC values [2]. Cross correlating DW imaging findings with morphological appearances on T1w, fat-saturated T2w/STIR is important. Distinct patterns of response can be recognized in the therapy assessment setting:

1. Increases in the volume of previously documented abnormal signal intensity lesions, new areas of abnormal signal intensity, or increases in the intensity of abnormalities on high b-value DW images can indicate disease progression. Modest increases, unchanged or slight decreases in ADC values compared to pretherapy values can occur in the setting of progression.
2. T2-shine through pattern: Occasionally unchanged high signal intensity on high b-value images is associated with marked rises in ADC values is observed. This pattern indicates a successful response to therapy.
3. Decreases in bone marrow disease signal intensity on high b-value images are generally observed with successful treatments. The extent of ADC increases seems to depend on the type of treatment given (see case study below). It has been noted that ADC increases are greater for cytotoxic chemotherapy and radiation. When patients are treated successfully with hormonal therapies, the ADC value increases seem to be less pronounced.
4. Occasionally high b-value signal intensity decreases are associated

with no ADC increases. Generally this pattern generally occurs in clinical responders (sclerotic response) although very occasionally we have noted it in non-responders (so called sclerotic progression). These appearances as thus considered indeterminate and currently we use morphologic and clinical assessments to assign the final response category.

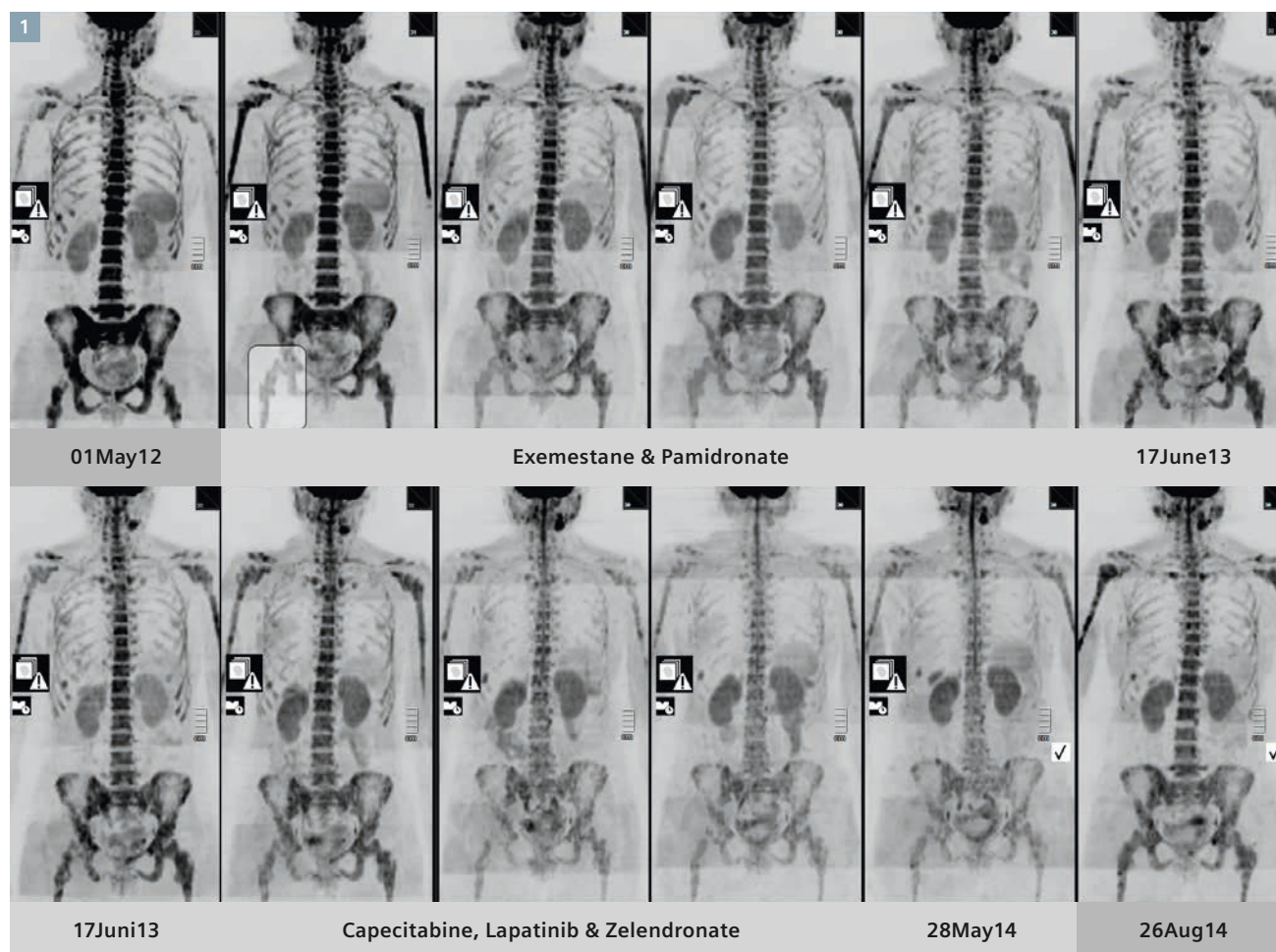
5. Stable disease is characterized by unchanging appearances on high b-value images. ADC changes can be variable, often remaining stable but

are sometimes slight decreased presumably because of increases in cell density within lesions that are unchanging in their extent within the confines of a fixed marrow space.

### Case study

58-year-old woman with metastatic invasive breast cancer, ER and HER-2 neu positive disease initially treated with hormone therapy (Exemestane) and bisphosphonates (Pamidronate) and then with chemotherapy (Capecitabine), HER-2 neu blockage (Lapatinib) and bisphosphonates

(Zoledronic acid). She remained moderately symptomatic with bone pain through the course of treatments, receiving a single fraction of radiotherapy to the right hip in May 2012. Chemotherapy was terminated in June 2014 because of toxicity. Serial examinations with whole-body diffusion MRI using b-values of b50 and 900 s/mm<sup>2</sup> together with spinal T1w and T2w (spectral fat suppression) were undertaken to monitor response to treatment. Eleven examinations were performed at 2–4 monthly intervals.

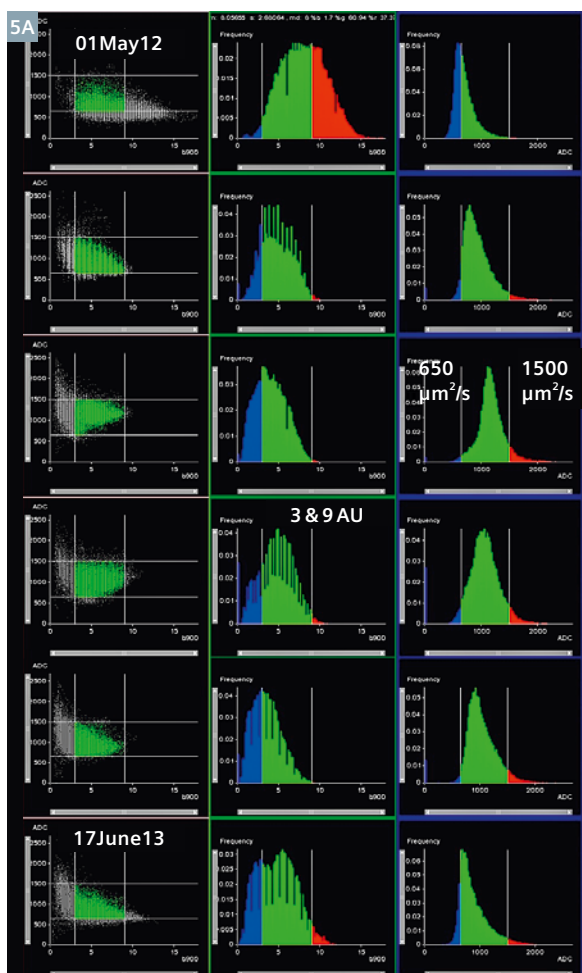


- 1 b900 3D MIP (inverted scale). The bone marrow is diffusely infiltrated in the axial skeleton with relative sparing of the humeri. Single fraction radiotherapy was administered to the right proximal femur to palliate bone pain. Decreases in the signal intensity of bone marrow with hormone therapy can be seen to occur slowly but there are focal areas of persistent hyperintensity indicating the presence of active disease (top row). By June 2013, the b900 signal intensity has increased indicating repopulation by cancer cells of the bone marrow and therapy failure. One year of therapy benefit with hormones is in line with the expected duration of patient benefit. The patient was switched to Capecitabine chemotherapy, augmented by HER-2 neu blockage with Lapatinib. The bisphosphonate was changed to Zoledronic acid. An impressive response to treatment is observed with marked reductions of signal intensity to levels lower than those achieved by hormone therapy alone (bottom row). However, when chemotherapy is stopped due to toxicity, rebound tumor growth can be seen between May and August 2014.

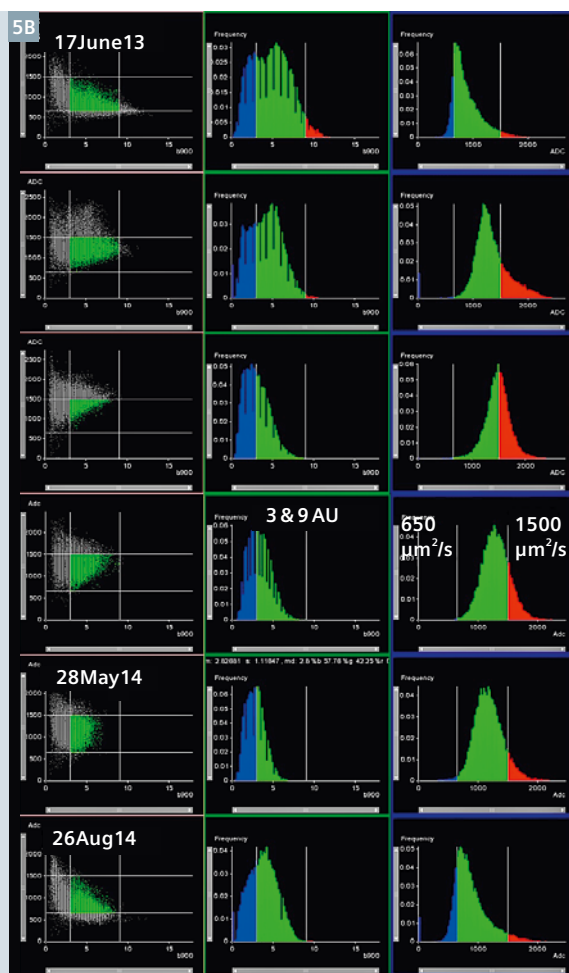








Exemestane & Pamidronate



Capecitabine, Lapatinib & Zoledronate

## 5 Histogram analysis of b900 signal intensity and of ADC values.

A whole pelvis volume-of-interest defined on examination 1 (using b900 images) and applied to all examinations after robust, elastic image registration. Left column: pixel scatter plots of muscle normalized b900 signal intensity (x-axis) and ADC values (y-axis). Middle and right columns: Relative frequency, muscle normalized b900 and ADC histograms showing serial changes over time (superior to inferior) for both treatments. The control lines on the histograms and scatter plots are placed on 3 and 9 for normalized b900 signal intensity and 650 and 1500  $\mu\text{m}^2/\text{s}$  for ADC. A unimodal, non-normal ADC histogram with a positive skewness and kurtosis is observed at baseline and each time the patient relapses. Hormone therapy results in a shift of the ADC histogram towards higher values (fewer blue pixels) but mean ADC increases are not large. With chemotherapy, the mean ADC values increase markedly with a negative skewness consistent with decreasing cellularity due to chemotherapy. ADC values decrease over time with chemotherapy but without high kurtosis developing consistent with bone marrow repair utilizing mechanisms including the removal of dead tumor cells, loss of tissue water, bone sclerosis, fat deposition and reduced perfusion (see Fig. 3 above for T2-weighted imaging correlate). However, once chemotherapy is stopped, positive skewness and increasing kurtosis of ADC histograms re-emerges consistent with disease relapse. Note how the scatter plot moves to the left each time the patient responds (decreases in normalized b900 signal intensity). All analyses were done using OncoCare\* software (Siemens Healthcare, Erlangen, Germany).

## References

- 1 Lecouvet FE, et al. MRI for response assessment in metastatic bone disease. *Eur Radiol.* 2013; 23(7): 1986-97.
- 2 Padhani AR, et al. Therapy monitoring of skeletal metastases with whole body diffusion MRI. *J Magn Reson Imaging* 2014; 39(5):1049-78.

\*Works-in-progress the product is currently under development and is not for sale in the US and other countries. Its future availability cannot be ensured.



## Contact

Professor Anwar R. Padhani, MB BS, FRCP, FRCR  
Paul Strickland Scanner Centre  
Mount Vernon Cancer Centre  
Rickmansworth Road, Northwood  
Middlesex HA6 2RN, United Kingdom  
Phone: +44 (0) 1923-844751  
Fax: +44 (0) 1923-844600  
anwar.padhani@stricklandscanner.org.uk

# Clinical Case: 3 Tesla MR Neurography-Guided Posterior Femoral Cutaneous Nerve Block

John Morelli; Jan Fritz

Musculoskeletal Radiology, Johns Hopkins University School of Medicine, Baltimore, MD, USA

## Background

The posterior femoral cutaneous nerve (PFCN), formerly known as the small sciatic nerve, is a sensory nerve formed by the sacral plexus (Fig. 1). It provides innervation to the posterior thigh into the popliteal area via its descending cutaneous branch and innervation to the proximal medial thigh, the perineum, scrotum/labia, and penis/clitoris via its perineal branch. Additionally, the inferior cluneal branches innervate the inferior buttocks.

Posterior femoral cutaneous neuropathy is an important differential consideration in the setting of posterior thigh, perineal, and gluteal pain. Causes include repetitive trauma such as from cycling or irritation in the setting of hamstring tendinopathy at the ischial tuberosity. Neuropathy

can affect the nerve at different levels throughout its course: Involvement of the cluneal branches manifests as clunealgia, the descending cutaneous branches as posterior thigh pain, and the perineal branches as pelvic pain. Isolated neuropathy of the perineal branch of the PFCN is difficult to distinguish from pudendal neuropathy due to the overlapping innervation of the perineum [1].

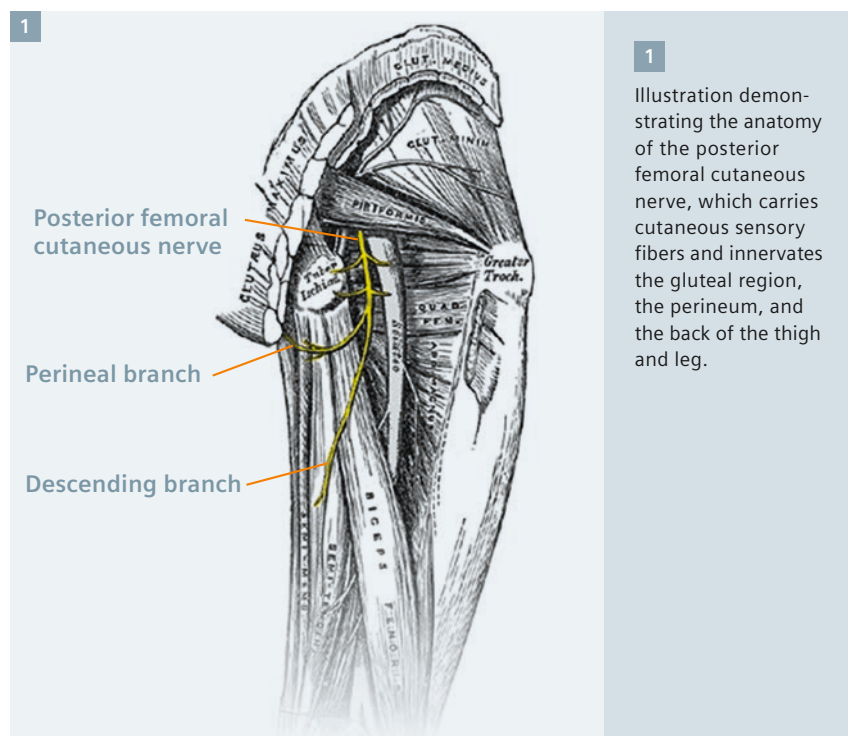
Selective diagnostic blocks of the PFCN can be helpful in this setting to assess the contribution of the nerve to patient symptoms and to localize a surgical target. Early injection techniques have been based on targeting near the ischial tuberosity without imaging guidance. While techniques utilizing computed tomography (CT) have also been described, high-reso-

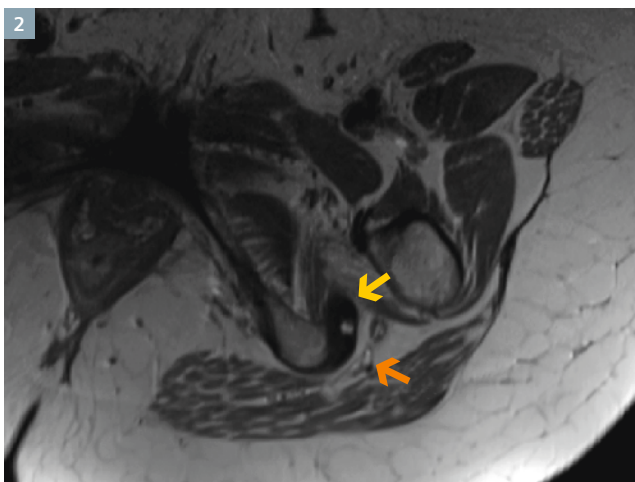
lution 3 Tesla (T) magnetic resonance neurography (MRN) enables highly accurate visualization of the PFCN [2]. As such, an MR-conditional needle can be utilized for precise targeting and monitored perineural drug delivery. The gains in signal-to-noise at 3T when compared to 1.5T or lower field open scanners, enable rapid acquisition of high-resolution MR images for definite identification, guidance and targeting of the PFCN, thus facilitating technically successful and highly valid injection.

## Case scenario

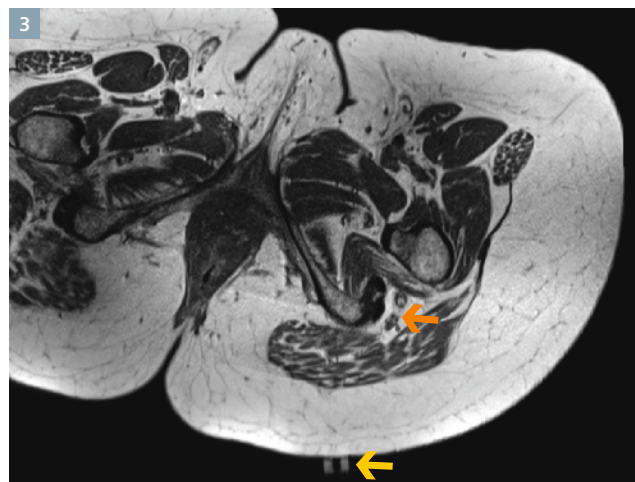
This 48-year-old African American woman with 9 out of 10 left buttocks pain that radiated into the perineum and posterior left thigh was referred by a peripheral nerve surgeon for a diagnostic perineural injection of the left posterior femoral cutaneous nerve with a long-acting local anesthetic agent. Leading differential diagnoses included PFCN and pudendal neuropathy. The PFCN block was requested to be performed proximally along the nerve's course near the ischial tuberosity, prior to the origin of the perineal branch of the PFCN.

The procedure was performed on a 3T MR imaging (MRI) system (MAGNETOM Skyra). For pre-procedural planning, high-resolution MR neurography was performed through the pelvis including the PFCN. Non-fat saturated proton density (PD) turbo spin echo (TSE) images (TR 7110 ms, TE 28 ms, matrix 640 × 400, FOV 35 × 28 cm, GRAPPA iPAT 2, slice thickness 2 mm) were acquired to evaluate and localize the posterior femoral cutaneous nerve using the body matrix coil and elements of the in-built spine matrix for signal reception posterior femoral

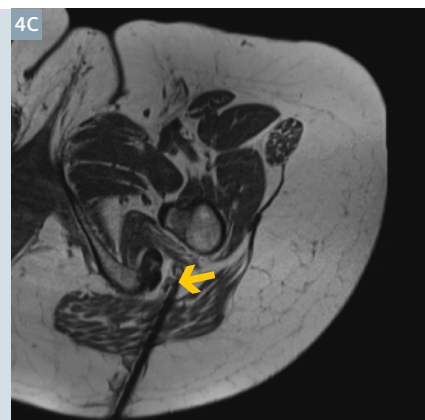
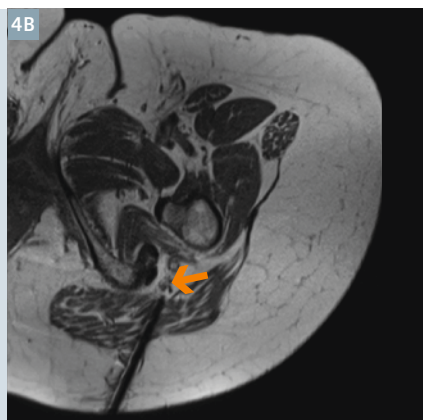
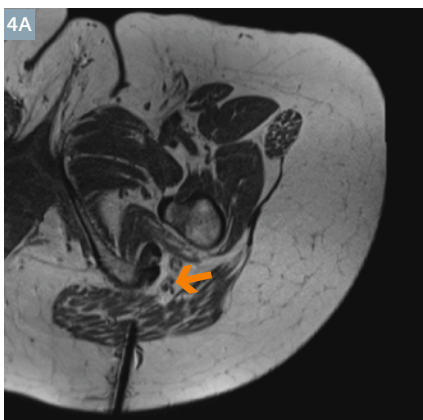




**2** Axial proton density-weighted MR image obtained for pre-procedural planning demonstrates tendinopathy at the left hamstring origin from the ischial tuberosity (yellow arrow) in addition to focal hyperintensity within the left posterior femoral cutaneous nerve (orange arrow). The latter finding is consistent with the patient's history of posterior femoral cutaneous neuropathy.



**3** Axial proton density-weighted MR image performed for skin entry site localization demonstrating the position of the skin marker (yellow arrow) relative to the posterior femoral cutaneous nerve (orange arrow).



**4** Sequential proton density-weighted MR images demonstrate advancement of the needle to the posterior femoral cutaneous nerve (orange arrows). In the final image (**4B**), the needle tip (yellow arrow) is located adjacent to the posterior femoral cutaneous nerve.

cutaneous (Fig. 2). On these initial images, an intermediate grade partial thickness tear of the left hamstring origin was noted as well as minimal hyperintensity involving the left posterior femoral cutaneous nerve. A modified PD TSE pulse sequence images (TR 2500 ms, TE 20 ms, matrix  $512 \times 384$ , FOV  $35 \times 22$  cm, GRAPPA iPAT 2, slice thickness 2 mm) aforementioned sequence was repeated for identification of the skin entry point and for subsequent monitoring of the needle position (Fig. 3)\*. Optimization of scan

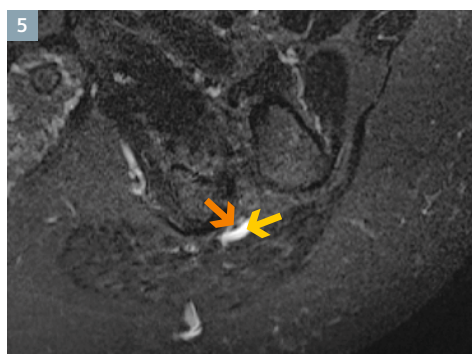
parameters and reduction of the number of slices to 5 resulted in a scan acquisition time of 20 seconds.

Once the skin entry site was selected, the skin over the left posterior proximal thigh was prepared and draped using sterile technique. Local anesthesia was achieved with a subcutaneous injection of 1% lidocaine. Under intermittent MRI guidance utilizing the aforementioned PD TSE sequence, a 10 cm 20 gauge needle was advanced adjacent to the left posterior femoral cutaneous nerve

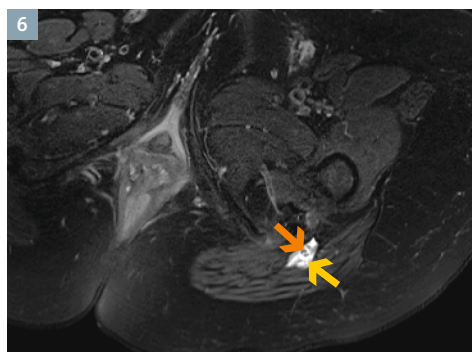
(Fig. 4). A test injection of 0.5 ml of sterile normal saline was performed followed by axial STIR images (TR 3500 ms, TE 68 ms, matrix  $384 \times 275$ , FOV  $35 \times 22$  cm, GRAPPA iPAT 2, slice thickness 4 mm) demonstrating appropriate fluid distribution around the PFCN (Fig. 5). Subsequently, circumferential perineural drug delivery was accomplished utilizing 3 ml of ropivacaine and 1 ml of Kenalog 40 as confirmed on post-procedural fat saturated T2-weighted images confirmed accumulation of fluid around

\*Metal: The MRI restrictions (if any) of the metal implant must be considered prior to patient undergoing MRI exam. MR imaging of patients with metallic implants brings specific risks. However, certain implants are approved by the governing regulatory bodies to be MR conditionally safe. For such implants, the previously mentioned warning may not be applicable. Please contact the implant manufacturer for the specific conditional information. The conditions for MR safety are the responsibility of the implant manufacturer, not of Siemens.

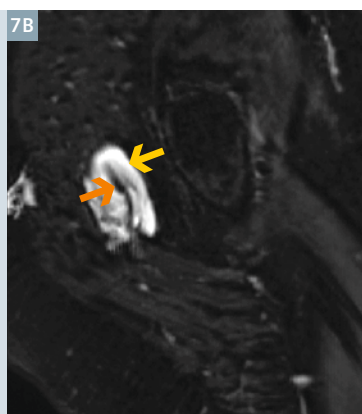
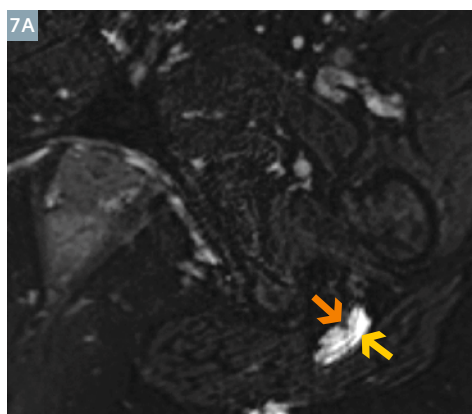




**5** Axial STIR MR image acquired following the injection of 0.5 ml of sterile normal saline demonstrate appropriate fluid distribution (yellow arrow) around the posterior femoral cutaneous nerve (orange arrow).



**6** Post-procedural T2-weighted images obtained with spectral fat saturation demonstrate the PFCN (orange arrow) bathing in ropivacaine and steroid following the injection of a total of 4 ml of the solution (yellow arrow).



**7** Three-dimensional fat saturated T2-weighted (TR 1600, TE 120) SPACE images with isotropic voxel sizes enables multi-planar reconstructions in any arbitrary plane. For post-injection imaging, this is useful as the nerve (orange arrows) can be evaluated both in standard planes (**7A**) and oblique planes along its longitudinal course (**7B**). The yellow arrows indicate the injectant.

the PFCN (TR 4000, TE 70, 488 × 384, FOV 35 × 22 cm, GRAPPA iPAT 2, 3 mm slice thickness) (Figs. 6, 7).

Following the procedure, the patient demonstrated exclusive anesthesia in PFCN distribution with post-procedural loss of light touch and pain sensation, confirming the technical success of the injection. The patient's pain improved to 2 out of 10, representing a positive pain and identifying the PFCN as a major contributor to the patient's pain syndrome. The patient was discharged the same day in excellent condition. No complications occurred.

## Discussion

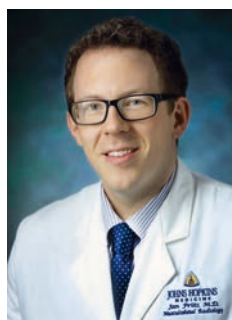
The high signal-to-noise ratio available with a state-of-the-art 3T MR imaging system provides the unprecedented ability to perform high-resolution MR neurography-guided perineural injections for highly accurate visualization of small nerve as well as needle targeting and perineural injection. This case report demonstrates how this techniques facilitates accurate targeting of the PFCN. High-resolution MR neurography is advantageous because of its unparalleled pairing of high contrast and spatial resolution, which is in contradistinction to blindly performed blocks or blocks performed under fluoroscopic or CT guidance. MRI is the preferred techniques due to exquisite nerve visualization, visualization of the injectants without the need of an additional contrast agent, unrestricted multiplanar imaging and finally the lack of ionizing radiation.

## Acknowledgement

We thank the Johns Hopkins Interventional MRI technologists Rose Butts RT(R)(CT)(MR), Lisa Martin RT(R)(MR), Krista Kahler RT(R)(MR), Amy Ring RT(R)(MR), and Kristen Whitson RT(R)(MR) for their superb expertise and dedicated patient care.

## References

- 1 Fritz, J., et al., Magnetic resonance neurography-guided nerve blocks for the diagnosis and treatment of chronic pelvic pain syndrome. *Neuroimaging Clin N Am*, 2014. 24(1): p. 211-34.
- 2 Fritz, J., et al., High-resolution magnetic resonance-guided posterior femoral cutaneous nerve blocks. *Skeletal Radiol*, 2013. 42(4): p. 579-86.



## Contact

Jan Fritz, M.D.  
Johns Hopkins University School of Medicine  
Russell H. Morgan Department of Radiology  
and Radiological Science  
601 N. Caroline Street, JHOC 5168  
Baltimore, MD 21287, USA  
jfritz9@jhmi.edu

# Case Series: Minimally Invasive 3 Tesla Interventional MRI

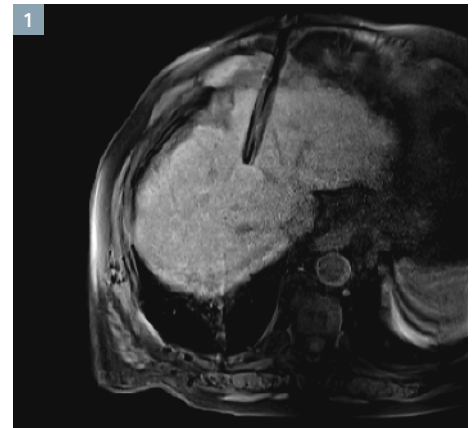
Kemal Tuncali, M.D.

Brigham and Women's Hospital, Dept. of Radiology, Boston, MA, USA

## Case 1

76-year-old man with cirrhosis was discovered to have a 2.5 cm lesion in segment 4/8 of the liver suspicious for a hepatocellular carcinoma (HCC). This was visualized on a 1.5 Tesla MRI study only with the use of i.v. contrast. It was not seen by ultrasound or CT scan. Hence, MRI-guided biopsy was performed in 3 Tesla MRI (MAGNETOM Verio, Siemens Healthcare, Erlangen, Germany).

Using spine coil elements and body matrix coil, the lesion is seen as a T1 hyperintense mass (Fig. 1). This was used to guide 22 gauge MRI-compatible needles into the mass and Fine-needle aspiration (FNA) biopsy was performed under local anesthesia and i.v. procedural sedation. The patient tolerated the procedure well without complications and the pathology proved the lesion to be an HCC.

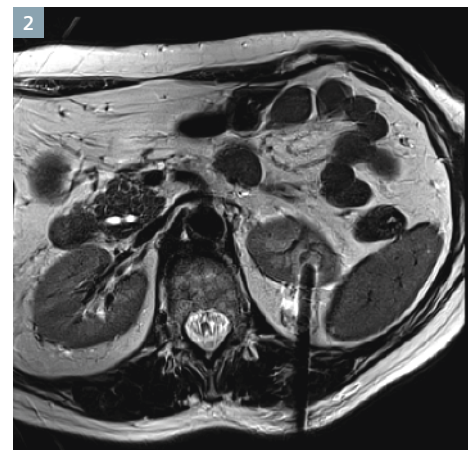


**1 MRI guided liver biopsy.**  
Intraprocedural axial T1-weighted SPGR (VIBE) shows liver lesion and biopsy needle\*.

## Case 2

65-year-old woman with history of breast cancer and a newly discovered 1.3 cm left kidney upper pole lesion suspicious for tumor. To differentiate between metastasis versus a renal origin tumor, percutaneous biopsy was indicated. However, this small renal mass was embedded in the renal parenchyma and very difficult to see with other imaging modalities except for MRI where it was well visualized even without the use of i.v. contrast material. 3T MRI (MAGNETOM Verio, Siemens Healthcare, Erlangen, Germany) with spine coil elements and body matrix coil was used for imaging.

Axial T2w TSE respiratory triggered sequence (BLADE) provided excellent visualization of the small lesion and needle location (18 gauge MRI-compatible) with minimal artifact (Fig. 2). The procedure was performed under local anesthesia and i.v. procedural sedation. The patient tolerated the procedure well without complications. Pathology showed mucinous tubular and spindle cell carcinoma, a low grade primary cancer of the kidney.



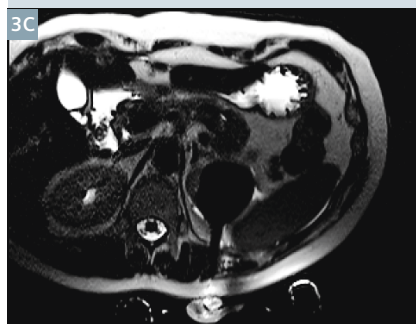
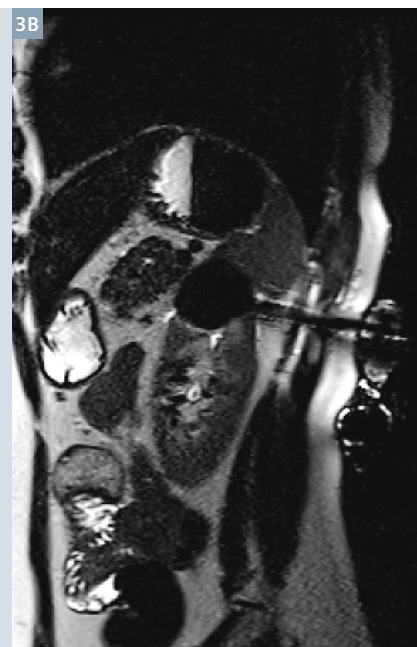
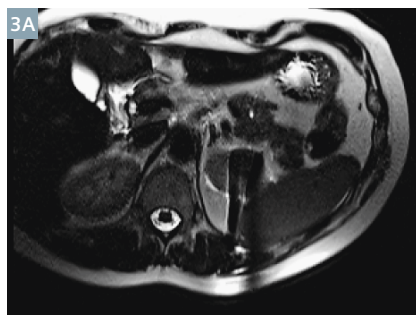
**2 MRI guided kidney biopsy.**  
Intraprocedural axial T2w respiratory triggered TSE (BLADE) shows the 18 gauge biopsy needle in the small renal mass.

\*Metal: The MRI restrictions (if any) of the metal implant must be considered prior to patient undergoing MRI exam. MR imaging of patients with metallic implants brings specific risks. However, certain implants are approved by the governing regulatory bodies to be MR conditionally safe. For such implants, the previously considered prior to patient undergoing MRI exam. MR imaging of patients with metallic implants brings specific risks. However, certain implants are approved by the governing regulatory bodies to be MR conditionally safe. For such implants, the previously mentioned warning may not be applicable. Please contact the implant manufacturer for the specific conditional information. The conditions for MR safety are the responsibility of the implant manufacturer, not of Siemens.

### Case 3

57-year-old woman with a 2 cm left kidney upper pole biopsy proven renal cell carcinoma. Its small size and intraparenchymal location in the upper pole renders it challenging for partial nephrectomy. Since it is well seen on MRI, cryoablation using MRI guidance was preferred as a minimally-invasive nephron-sparing treatment option. 3T MRI (MAGNETOM Verio, Siemens Healthcare, Erlangen, Germany) with spine coil elements and an 11 cm loop coil was used for imaging.

Axial and sagittal HASTE sequence was used to place three 17 gauge MRI-compatible cryoablation probes (Galil Medical, Plymouth, PA USA) and to monitor the ablation (Fig. 3). This helped cover the tumor completely while preventing injury to adjacent pancreas and adrenal gland. The procedure was performed in the prone position under general anesthesia without complications.



#### 3 Cryoablation of native renal mass.

(3A) Intraprocedural axial T2w HASTE shows two of the probes in the renal tumor. (3B) Sagittal T2w HASTE obtained 10 min into the 2<sup>nd</sup> freezing cycle shows the iceball close to adjacent pancreas but without overlap.

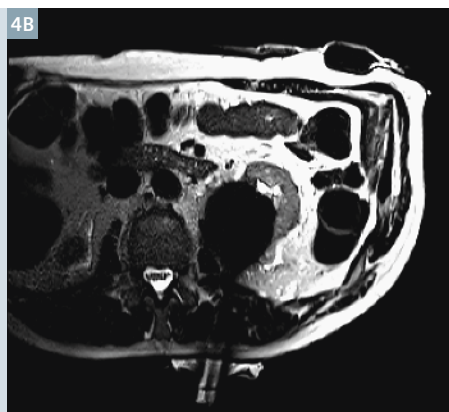
(3C) Axial T2w HASTE obtained at the end of the 2<sup>nd</sup> 15 min freezing cycle shows that the iceball has eclipsed the tumor and is close to the adjacent adrenal gland but without overlap.

### Case 4

68-year-old man with a 2.9 cm left lower pole biopsy proven renal cell carcinoma, discovered during hematuria workup. Due to comorbid coronary artery disease, patient was referred for minimally invasive, nephron sparing image-guided cryoablation. MRI guidance was preferred due to tumor proximity to ureter to minimize risk

of injury. 3T MRI (MAGNETOM Verio, Siemens Healthcare, Erlangen, Germany) with spine coil elements and body matrix coil was used for imaging. Axial T2W HASTE sequence was used to place three 17 gauge MRI-compatible cryoablation probes (Galil Medical, Plymouth, PA USA) and to monitor the ablation (Fig. 4).

This ensured covering the tumor completely while preventing injury to adjacent ureter. The procedure was performed in the prone position under local anesthesia and i.v. procedural sedation. The patient tolerated the procedure well without complications.



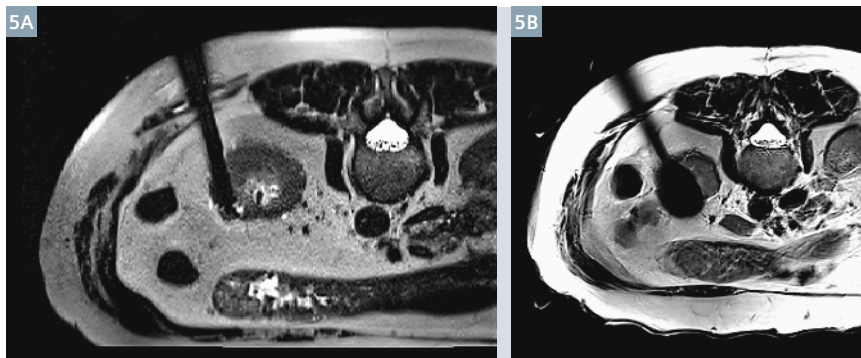
4

#### Cryoablation of native renal mass.

(4A) Intraprocedural axial T2w HASTE shows first of the three probes being placed in the renal tumor.

(4B) Intraprocedural axial T2w HASTE obtained at the end of the 2<sup>nd</sup> 15 min freezing cycle shows that the iceball has eclipsed the tumor without overlapping adjacent proximal ureter.





5

**Cryoablation of native renal mass.**

(5A) Intraprocedural axial T2w HASTE shows first of the three probes being placed in the renal tumor.

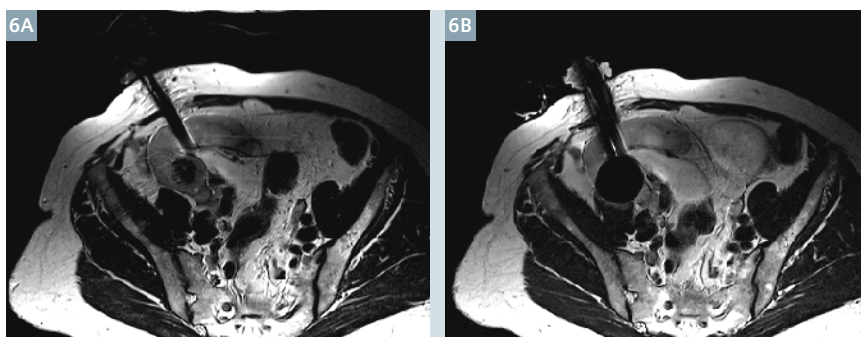
(5B) Intraprocedural axial T2w respiratory triggered TSE (BLADE) obtained at the end of the 2<sup>nd</sup> 15 min freezing cycle shows that the iceball has eclipsed the tumor without overlapping adjacent colonic wall.

**Case 5**

68-year-old man with 2.4 cm left lower pole renal cell carcinoma. Due to history of lung cancer, cutaneous T-cell lymphoma and chronic lymphocytic leukemia, he was referred for percutaneous cryoablation as a minimally invasive, nephron sparing treatment option.

3T MRI (MAGNETOM Verio, Siemens Healthcare, Erlangen, Germany) with spine coil elements and body matrix coil was used for imaging. Axial T2w HASTE sequence was used to place three 17 gauge MRI-compatible cryoablation probes (Galil Medical, Plymouth, PA USA) (Fig. 5A). Then, for more detailed monitoring of the ablation, we utilized an axial T2w

respiratory triggered TSE (BLADE) sequence (Fig. 5B). This ensured covering the tumor completely while preventing injury to adjacent colon. The procedure was performed in the prone position under local anesthesia and i.v. procedural sedation. The patient tolerated the procedure well without complications.



6

**Cryoablation of renal transplant mass.**

(6A) Intraprocedural axial T2w TSE shows first of the three probes being placed in the renal tumor.

(6B) Intraprocedural axial T2w TSE obtained at the end of the 2<sup>nd</sup> 15 min freezing cycle shows that the iceball has eclipsed the tumor without overlapping adjacent renal pelvis.

**Case 6**

66-year-old woman with a 2.1 cm biopsy proven renal cell carcinoma inside of a renal transplant located in her right lower abdomen. She was referred for percutaneous cryoablation as a minimally-invasive nephron-sparing treatment option. The tumor margins were not well seen on ultrasound or CT scan due to its small size and intraparenchymal location.

However, MRI showed the tumor very well. 3T MRI (MAGNETOM Verio, Siemens Healthcare, Erlangen, Germany) with spine coil elements and an 11 cm loop coil was used for imaging.

Axial T2w TSE sequence was used to place three 17 gauge MRI-compatible cryoablation probes (Galil Medical,

Plymouth, PA USA) and to monitor the ablation (Fig. 6). This ensured covering the tumor completely while preventing injury to adjacent renal pelvis and ureter. The procedure was performed in the supine position under local anesthesia and i.v. procedural sedation. The patient tolerated the procedure well without complications.

**Contact**

Kemal Tuncali, M.D.  
Brigham and Women's Hospital  
Department of Radiology  
75 Francis St  
Boston, MA 02115, USA  
ktuncali@partners.org

# 3T Multiparametric MRI and MR-Guided In-Bore Biopsy to Detect Prostate Cancer

Frederic Dietzel, M.D.; Lars Schimmöller, M.D.; Michael Quentin, M.D.; Dirk Blondin, M.D.

University Dusseldorf, Medical Faculty, Department of Diagnostic and Interventional Radiology, Dusseldorf, Germany

## Introduction

Multiparametric magnetic resonance imaging (mp-MRI) of the prostate gains increasing influence in prostate cancer detection, especially in patients with prior negative transrectal ultrasound (TRUS) biopsy and continuous suspicion of prostate cancer [1]. Prostate MRI can also be useful in active surveillance of low-grade tumors [2]. The European Society of Urogenital Radiology (ESUR) released in 2012 guidelines for prostate MRI in order to standardize evaluation and reporting [3]. As a consequence of defining suspect areas in the mp-MRI subsequent targeted biopsies (MR-GB) to verify these lesions should be performed. Currently three techniques are available that incorporate MRI information to define target structures for biopsy: Cognitive ultra-

sound biopsy (c-GB), MRI/ultrasound fusion biopsy (FUS-GB), and MR-guided in-bore biopsy (IB-GB) [1, 4].

## Patient history

A 62-year-old man was referred to our Institute of Diagnostic and Interventional Radiology with two negative TRUS-guided biopsies and remaining suspicion of prostate cancer due to continuously increasing prostate-specific antigen (PSA) values. The ultimate PSA value was 9.9 ng/ml. The prostate volume was only slightly enlarged (42 ml).

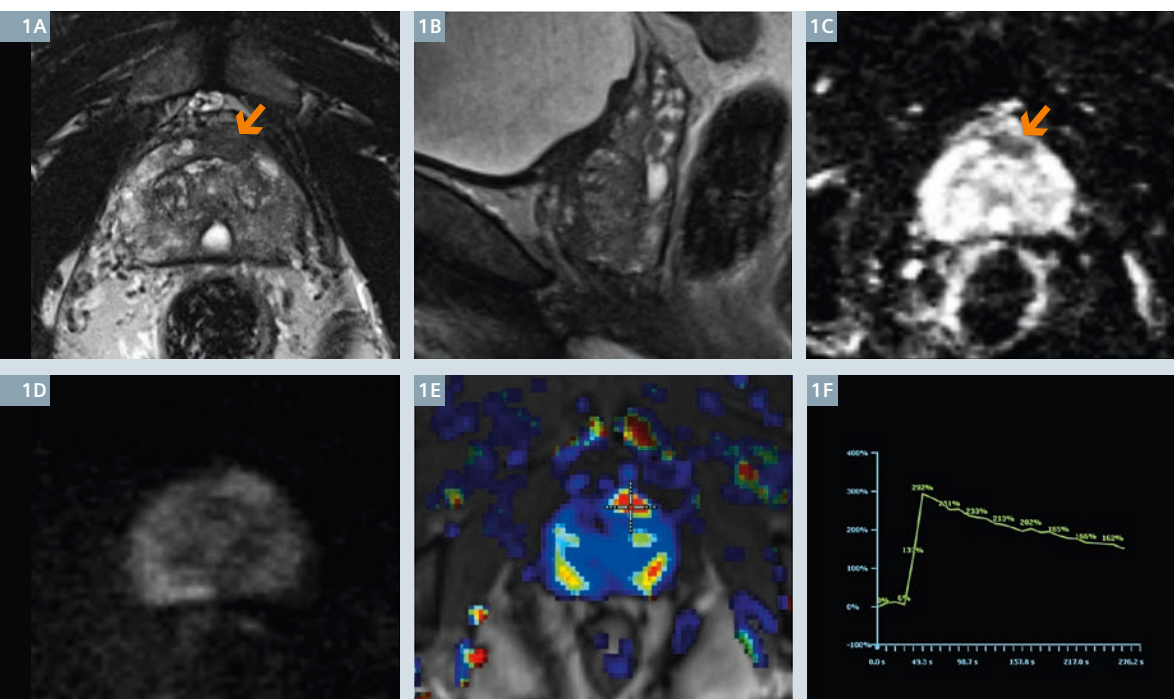
## MR imaging

In the apical anterior prostate gland mp-MRI detected a highly suspicious area, located in region 13as/14as on a 27-region localization scheme [5]

(Fig. 1). This lesion was rated according to the PI-RADS scoring system for each MR-sequence. The overall PI-RADS classification for this lesion was 5 (clinically significant disease is highly likely to be present) [6]. In addition, the MRI showed post-inflammatory transformations in the peripheral zone and considerable changes due to benign prostate enlargement (BPE) in the transition zone. The seminal vesicles were inconspicuous and no enlarged lymph nodes were found in the area under investigation.

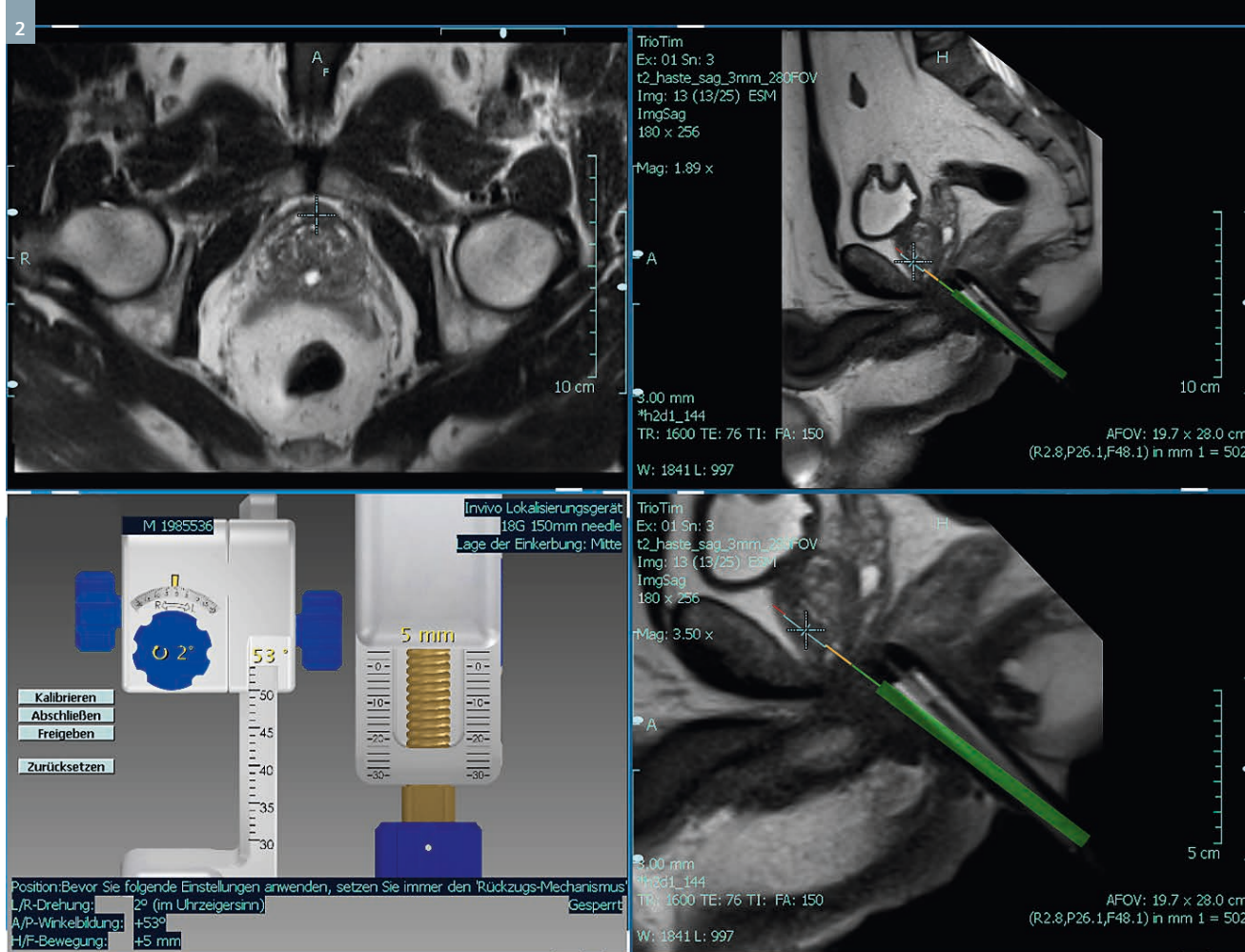
## Sequence details

Prostate mp-MRI was performed at a 3T MRI system (MAGNETOM Trio; Siemens Healthcare, Erlangen, Germany) with a 6-channel phased-array body coil. The imaging protocol



**1** Prostate mp-MRI including T2-weighted imaging (1A, B), apparent diffusion coefficient map derived from diffusion-weighted imaging (ADC) (1C), high b-value image of diffusion-weighted imaging (DWI) (1D), and dynamic contrast-enhanced imaging (DCE) (1E, F). Anteriorly located cancer suspect lesion (orange arrow; PI-RADS 5).





2 Setting of MR-guided in-bore biopsy (IB-GB) with a DynaTRIM biopsy device (Invivo, Gainesville, FL, USA) and DynaCAD workstation (Invivo).

was adapted according to the ESUR guidelines [3]. To suppress peristalsis the patient received 20 mg butylscopolamine (Buscopan; Boehringer, Ingelheim, Germany). Mp-MRI included T2-weighted (T2w) imaging, T1-weighted (T1w) imaging, diffusion-weighted imaging (DWI), and dynamic contrast-enhanced imaging (DCE-MRI).

T2-weighted turbo spin echo sequences were acquired in three standard orthogonal planes

**axial:** TR 10630 ms, TE 117 ms, FOV 12.8 cm, voxel size  $0.5 \times 0.5 \times 3.0$  mm, image matrix  $256 \times 256$ , turbo factor 23;  
**sagittal/coronal:** TR 11330 ms, TE 103 ms, FOV 17 cm, voxel size  $0.7 \times 0.7 \times 3.0$  mm, image matrix  $256 \times 256$ , turbo factor 25.

For T1w axial turbo-spin echo images (TR 650 ms, TE 13 ms, FOV 30 cm, voxel size  $1.3 \times 0.9 \times 5.0$  mm, gap 10%, image matrix  $240 \times 320$ , turbo factor 3), and for DWI single-shot spin-echo echo-planar sequence (TR 4600 ms,

TE 90 ms, FOV 20.4 cm, voxel size  $1.5 \times 1.5 \times 3.0$  mm, image matrix  $136 \times 136$ , GRAPPA parallel imaging scheme with acceleration factor 2) using 3 b-values (0, 500, 1000  $\text{s/mm}^2$ ) with eight averages, were performed. Apparent diffusion coefficient (ADC) parameter maps were calculated by the scanner software using the standard monoexponential model. For the DCE-MRI volume-interpolated gradient echo sequence (TR 5.26 ms, TE 1.76 ms, FOV 19.2 cm, voxel size  $1.5 \times 1.5 \times 3.0$  mm, image matrix  $128 \times 128$ , GRAPPA parallel imaging scheme with acceleration factor 2, 31 scans, scan time 5:05 min, temporal resolution 10 sec) were applied. Contrast media injection started after the second measurement using gadoteric acid (Dotarem®, Guerbet, Aulnay-sous-Bois, France) in a weight-adapted standard dose (0.2 mmol/kg body weight) with an injection rate of 3 ml/s. Total scan time was approximately 33 minutes.

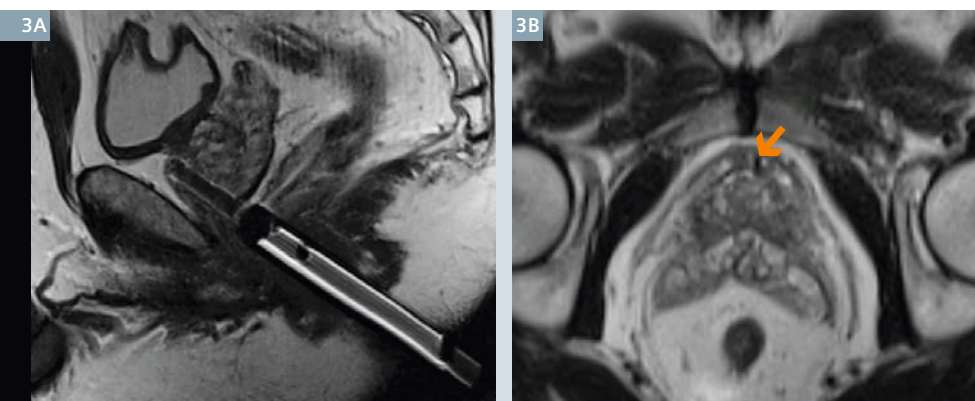
## MRI/US fusion guided biopsy (FUS-GB)

Subsequently to the suspect mp-MRI a targeted FUS-GB was performed using the Urostation® 3-dimensional ultrasound system (Koelis, La Tranche, France) to ensure biopsy cores were taken of the described suspicious area. The histological result revealed minor chronic prostatitis and no cancer verification.

## MR-guided in-bore biopsy (IB-GB)

Owing to the highly suspicious mp-MRI we decided in consent with the patient to perform another targeted biopsy. An IB-GB was performed on the same 3T MRI system (MAGNETOM Trio). The patient was placed in a prone position and a needle guide fixed to a portable biopsy device (DynaTRIM, Invivo, Gainesville, FL, USA) was introduced rectally. Image data were transferred to a DynaCAD workstation





3 Biopsy needle\* verification of the direct lesion hit in our patient (orange arrow).

(Invivo) for biopsy planning (Fig. 2). Two cores were taken of the anterior lesion in region 14as with an MR-compatible, 18-gauge, fully automatic biopsy gun (Invivo). Due to the negative results of the prior MRI/US fusion prostate biopsy we decided to perform a needle control scan. The needle control scan confirmed the correct positioning of the biopsy needle (Fig. 3). The histopathology resulted in a malignant gland forming prostate tumor (Gleason score 4+3=7), described as an acinar adenocarcinoma with high percentage of cancer involvement (80% per core).

## Discussion

The current gold standard for prostate diagnostics is the digital rectal examination, the PSA value, and TRUS followed by a systematic TRUS-guided biopsy. Mp-MRI is a promising complementary technique that allows in uncertain or problematic cases a good differentiation between tumor and benign lesions [1, 7]. It furthermore enables targeted MR-guided biopsy (MR-GB) procedures, as a logical consequence of describing suspicious lesions. MRI/US fusion-guided biopsy (FUS-GB) shows good results, however, 2D/3D models are only overlaid, and an exact peer-to-peer verification is still missing, especially if the suspicious lesion described in the MRI is not visible in ultrasound [8]. MR-guided in-bore biopsy (IB-GB) offers some advantages in comparison. Lesions are presented and biopsied in the

same modality, a direct control of taken biopsy cores is feasible, and an individual management of BPE or patient movement is possible. In our patient we could detect and histologically verify a significant prostate cancer by IB-GB alone.

## References

- 1 Hoeks CM, Schouten MG, Bomers JG, Hoogendoorn SP, Hulsbergen-van de Kaa CA, Hambrock T, Vergunst H, Sedelaar JP, Futterer JJ, Barentsz JO (2012) Three-Tesla magnetic resonance-guided prostate biopsy in men with increased prostate-specific antigen and repeated, negative, random, systematic, transrectal ultrasound biopsies: detection of clinically significant prostate cancers. *Eur Urol* 62:902-909.
- 2 Murphy G, Haider M, Ghai S, et al (2013) The expanding role of MRI in prostate cancer. *AJR* 201:1229-38.
- 3 Barentsz JO, Richenberg J, Clements R et al (2012) ESUR prostate MR guidelines 2012. *Eur Radiol* 22: 746-757.
- 4 Quentin M, Schimmöller L, Arsov C, Rabenalt R, Antoch G, Albers P, Blondin D (2013) 3-T in-bore MR-guided prostate biopsy based on a scoring system for target lesions characterization. *Acta Radiol* 54:1224-9.
- 5 Dickinson L, Ahmed HU, Allen C, Barentsz JO, Carey B, Futterer JJ, Heijmink SW, Hoskin P, Kirkham AP, Padhani AR, Persad R, Puech P, Punwani S, Sohaib A, Tombal B, Villers A, Emberton M (2013) Scoring systems used for the interpretation and reporting of multiparametric MRI for prostate cancer detection, localization, and characterization: could standardization lead to improved utilization of imaging within the diagnostic pathway? *J Magn Reson Imaging* 37:48-58.
- 6 Röthke M, Blondin D, Schlemmer HP, Franiel T (2013) PI-RADS Classification: Structured Reporting for MRI of the Prostate. *Rofo* 185:253-61.
- 7 Hambrock T, Somford DM, Hoeks C et al (2010) Magnetic resonance imaging guided prostate biopsy in men with repeat negative biopsies and increased prostate specific antigen. *J Urol* 183: 520-527.
- 8 Siddiqui MM, Rais-Bahrami S, Truong H, Stamatakis L, Vourganti S, Nix J, Hoang AN, Walton-Diaz A, Shuch B, Weintraub M, Kruecker J, Amalou H, Turkbey B, Merino MJ, Choyke PL, Wood BJ, Pinto PA (2013) Magnetic resonance imaging/ultrasound-fusion biopsy significantly upgrades prostate cancer versus systematic 12-core transrectal ultrasound biopsy. *Eur Urol* 64:713-719.

## Contact

Lars Schimmöller, M.D.  
University Dusseldorf,  
Medical Faculty  
Department of Diagnostic and  
Interventional Radiology  
Moorenstrasse 5  
40225 Düsseldorf  
Germany  
Phone: +49-211-81-17752  
lars.schimmoller@med.  
uni-duesseldorf.de



Left to right: Frederic Dietzel, Lars Schimmöller, Michael Quentin, Dirk Blondin

\*Metal: The MRI restrictions (if any) of the metal implant must be considered prior to patient undergoing MRI exam. MR imaging of patients with metallic implants brings specific risks. However, certain implants are approved by the governing regulatory bodies to be MR conditionally safe. For such implants, the previously mentioned warning may not be applicable. Please contact the implant manufacturer for the specific conditional information. The conditions for MR safety are the responsibility of the implant manufacturer, not of Siemens.

# High-Resolution Diffusion-Weighted Imagings of the Prostate Using RESOLVE at 3T

Liang Li<sup>1</sup>; Liang Wang<sup>1</sup>; Hui Liu<sup>2</sup>

<sup>1</sup>Department of Radiology, Tongji Hospital, Tongji Medical College, Huazhong University of Science and Technology, Wuhan, China

<sup>2</sup>MR Collaboration NE Asia, Siemens Healthcare, Shanghai, China

## Introduction

Diffusion-weighted imaging (DWI) is becoming an increasingly robust tool in the assessment and exclusion of prostate disease [1]. However, multiple recent studies have raised concerns regarding the anatomical distortion of single-shot DWI. A novel approach to distortion reduction using RESOLVE, resulting in a high-resolution DWI examination, is described [2-5]. In our hospital, we performed hundreds of prostate examinations of patients using RESOLVE. The technique achieves a low level of susceptibility artifact by allowing a very short echo spacing in the EPI echo train and the artifacts are further reduced by combining the technique with parallel imaging using GRAPPA [6].

## Protocol

Prostate DWI examinations were performed on a clinical 3T scanner (MAGNETOM Skyra, Siemens Healthcare, Erlangen, Germany) with an 18-channel body-matrix coil placed over, and a spine coil underneath, the pelvis. The patients were positioned in a head-first supine position.

At 3T MRI, RESOLVE images were acquired with the following parameters: parallel imaging using GRAPPA with an acceleration factor of 2, FOV 260 mm, matrix 128 × 176, pixel size 1.2 mm × 1.2 mm, 20 slices, slice thickness 3 mm, number of readout segments 13, TR 4800 ms, TE 60 ms, b-values of 0 s/mm<sup>2</sup> (1 average) and 800 s/mm<sup>2</sup> (2 averages), total scanning time 6 min 11 s.

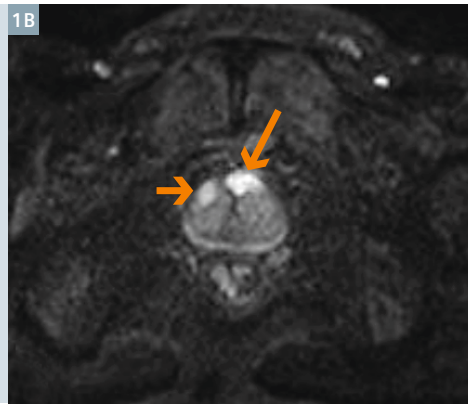
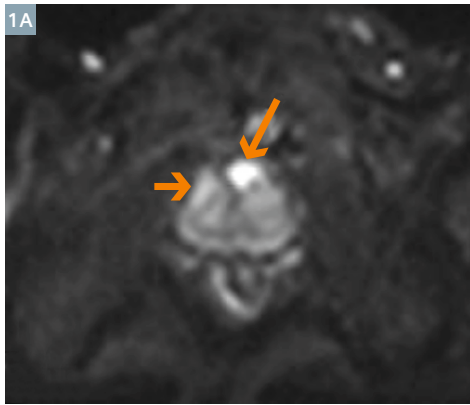
In addition, our past clinical standard single-shot DWI images were also acquired for comparison using the following parameters: Parallel imaging using GRAPPA with an acceleration factor of 2, FOV 260 mm, matrix 64 × 88, phase partial Fourier factor 6/8, pixel size 2.4 mm × 2.4 mm, 20 slices, slice thickness 3 mm, TR 4500 ms, TE 85 ms, b-values of 0 s/mm<sup>2</sup> (1 average) and 800 s/mm<sup>2</sup> (2 averages), total scanning time 1 min 20 s.

## Case 1

A 57-year-old man presented to his primary care provider in January 2014 with a 2-month history of increasing urinary frequency and poor stream. He denied any gross hematuria, bone pain, or significant weight loss. Digital rectal examination (DRE) revealed an asymmetrically enlarged, firm, and nontender prostate. Serum prostate-specific

antigen (PSA) was 12.8 ng/ml. Tamsulosin hydrochloride (Flomax®, Boehringer, Ingelheim, Germany) 0.4 mg daily was started and the patient was referred for initial urologic evaluation. The patient denied any occupational exposures or family history of prostate cancer or other genitourinary malignancy. On the first day, prostate ss-EPI DWI imaging

revealed a lesion in anterior fibromuscular stroma (AFS) region of his prostate. On the second day, we found two lesions in DWI using RESOLVE technology. Transrectal ultrasound (TRUS)-guided prostate biopsy and pathological examinations were performed subsequently. The two lesions were confirmed as prostate adenocarcinoma (left: Gleason 4+4, right: Gleason 3+4).



1

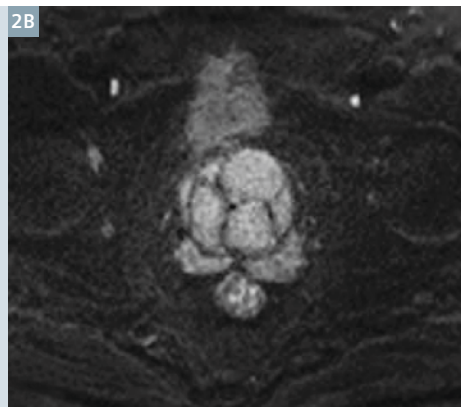
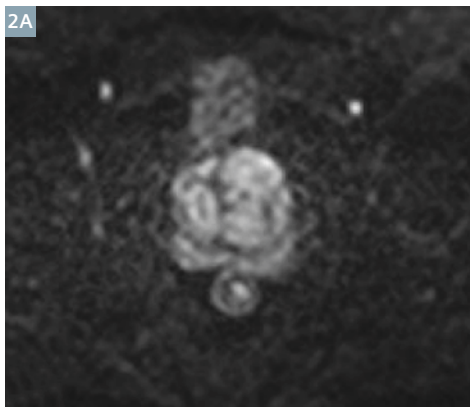
**(1A)** Conventional ss-EPI DWI revealing only a lesion in the anterior fibromuscular stroma (AFS) region (long white arrow). **(1B)** RESOLVE EPI DWI showing excellent high-resolution image quality and revealing another lesion (short white arrow) without anatomical distortion.

## Case 2

A 69-year-old man presented with a chief complaint of refractory urinary retention. DRE was performed with prostate gland of 4 finger breadths, firm consistency and smooth surface.

The PSA level was 5.16 ng/ml. A Doppler ultrasound examination demonstrated an enlargement of the prostate volume ( $48 \times 52 \times 60 \text{ mm}^3$ ), asymmetric shape, with multiple

hypointense nodules. The biopsy sample confirmed benign prostatic hyperplasia (BPH) and chronic prostatitis.



2

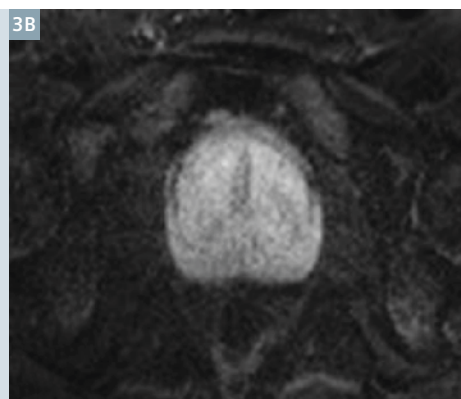
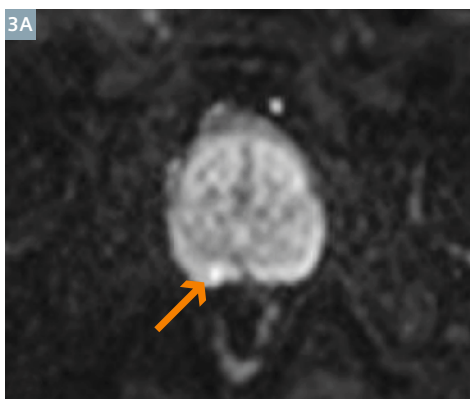
**(2A)** Conventional ss-EPI DWI displaying a low-resolution prostate image. **(2B)** RESOLVE EPI DWI showing clearly excellent high-resolution image with multiple hyperplastic nodules.

## Case 3

A 70-year-old man suffered from acute urinary retention requiring urethral catheterization, with no evidence of hematuria or fever. He had a history of chronic urinary retention, which was treated with oral medicine (Flomax®) for 2 months, but no history of urinary

trauma or infection. Laboratory testing such as blood count, serum biochemistry, and urinalysis were in the normal range. A urine culture was negative, and the serum level of PSA was 3.1 ng/ml. The single-shot DWI revealed a nodular lesion with focal

high signal-intensity in the right peripheral zone of his prostate, while RESOLVE DWI examination found no abnormal lesions. TRUS-guided prostate biopsy confirmed benign prostatic hyperplasia (BPH).



3

**(3A)** Conventional ss-EPI DWI revealing a suspicious lesion in the right peripheral zone (long white arrow). **(3B)** RESOLVE EPI DWI showing no abnormal lesions. The suspicious lesion being misdiagnosed as prostate cancer due to susceptibility effect.



## Conclusion

Results from hundreds of examinations of our prostate patients indicate that anatomic depiction and overall image quality were improved with the RESOLVE sequence when compared with the single-shot DWI sequence. Prostate DWI applications with RESOLVE demonstrated reduced artifacts and improved lesion detection.

In our previous unpublished study, we had obtained a number of diagnostic-quality prostate DWIs based on RESOLVE. For image sharpness, anatomical distortion, imaging contrast, lesion conspicuity, detailed anatomical visualization and diagnostic confidence, RESOLVE EPI was considered the to be overall superior in 90% of the cases. In the past, to assist workflow, we needed to have rectum preparation in a certain number of patients where the susceptibility artifacts coming from the rectum was strong. However, we have now eliminated the need for this preparation when using RESOLVE, because of less susceptibility impact on the prostate imaging.

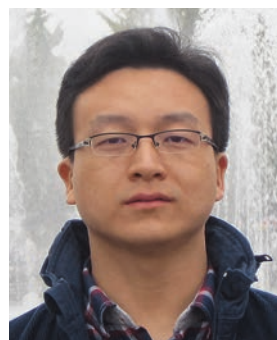
In summary, the new high-resolution RESOLVE protocol provides significant benefits compared with the mostly clinically used single-shot DWI. The higher spatial resolution results in better lesion conspicuity, better defined internal architecture, and better overall image quality. In the future, this method may have potential as a tool to predicate prostate cancer at an earlier stage or to obtain an image-guided prostate biopsy.

## References

- 1 Jin G, Su DK, Luo NB, et al. Meta-analysis of diffusion-weighted magnetic resonance imaging in detecting prostate cancer. *J Comput Assist Tomogr.* 2013;37(2): 195-202.
- 2 Holdsworth SJ, Skare S, Newbould RD, Bammer R. Robust GRAPPA-accelerated diffusion-weighted readout-segmented (RS)-EPI. *Magn Reson Med.* 2009; 62(6): 1629-40.
- 3 Frost R, Porter DA, Miller KL, Jezzard P. Implementation and assessment of diffusion-weighted partial Fourier readout-segmented echo-planar imaging. *Magn Reson Med.* 2012;68(2):441-51.
- 4 Yeom KW, Holdsworth SJ, Van AT, et al. Comparison of readout-segmented echo-planar imaging (EPI) and single-shot EPI in clinical application of diffusion-weighted imaging of the pediatric brain. *AJR Am J Roentgenol.* 2013;200(5):W437-43.
- 5 Bogner W, Pinker-Domenig K, Bickel H, et al. Readout-segmented echo-planar imaging improves the diagnostic performance of diffusion-weighted MR breast examinations at 3.0 T. *Radiology.* 2012;263(1):64-76.
- 6 Griswold MA, Jakob PM, Heidemann RM, et al. Generalized autocalibrating partially parallel acquisitions (GRAPPA). *Magn Reson Med.* 2002;47(6):1202-10.
- 7 Porter DA, Heidemann RM. High resolution diffusion-weighted imaging using readout-segmented echo-planar imaging, parallel imaging and a two-dimensional navigator-based reacquisition. *Magn Reson Med.* 2009;62(2):468-75.
- 8 Holdsworth SJ, Skare S, Newbould RD, et al. Readout-segmented EPI for rapid high resolution diffusion imaging at 3 T. *Eur J Radiol.* 2008;65(1):36-46.



Wang Liang



Li Liang

## Contact

Professor Liang Wang, M.D., Ph.D.  
Vice-Chairman, Department of Radiology  
Tongji Hospital, Tongji Medical College  
Huazhong University of Science & Technology  
Wuhan 430030  
China  
Phone: +86 (27) 83663737  
wangliang2001@gmail.com

# How Breast MRI Changed the Operative Management

Marymol Koshy<sup>1</sup>, Mohammad Hanafiah<sup>1</sup>, Clemens Kaiser<sup>2</sup>

<sup>1</sup>Medical Imaging Unit, Faculty of Medicine, Universiti Teknologi MARA, Malaysia

<sup>2</sup>Institute of Clinical Radiology and Nuclear Medicine, University Medical Centre Mannheim, Medical Faculty Mannheim - University of Heidelberg, Mannheim, Germany

## *“Women should not suffer or die from breast cancer”*

Professor W. A. Kaiser

### Introduction

With advancing imaging technology there has been increasing interest in the use of breast magnetic resonance imaging (MRM – MR-Mammography) worldwide. Traditionally mammography complemented by ultrasound has remained the mainstay for the diagnosis and evaluation of breast carcinoma. The aim of breast MRI is to obtain a reliable evaluation of any lesion within the breast. It is currently used as an adjunct to the standard diagnostic procedures of breast, i.e., clinical examination, mammography and ultrasound [1]. According to the American College of Radiology the current indications for Breast MR are, however, only patients following operation or radiation, preoperative staging, cancer of unknown primary (CUP syndrome), high-risk patients (e.g. BRCA1 or 2) and MRI guided biopsies [2]. This is mainly attributed to the high costs, availability and reader-dependent specificity of MRM. In Malaysia, MRM is still a relatively new field, with gradually increasing interest shown by some of the larger institutions.

We herein wish to report a case of infiltrating ductal carcinoma in a woman whose pre-operative

planning and surgical management changed after performing dynamic MRM.

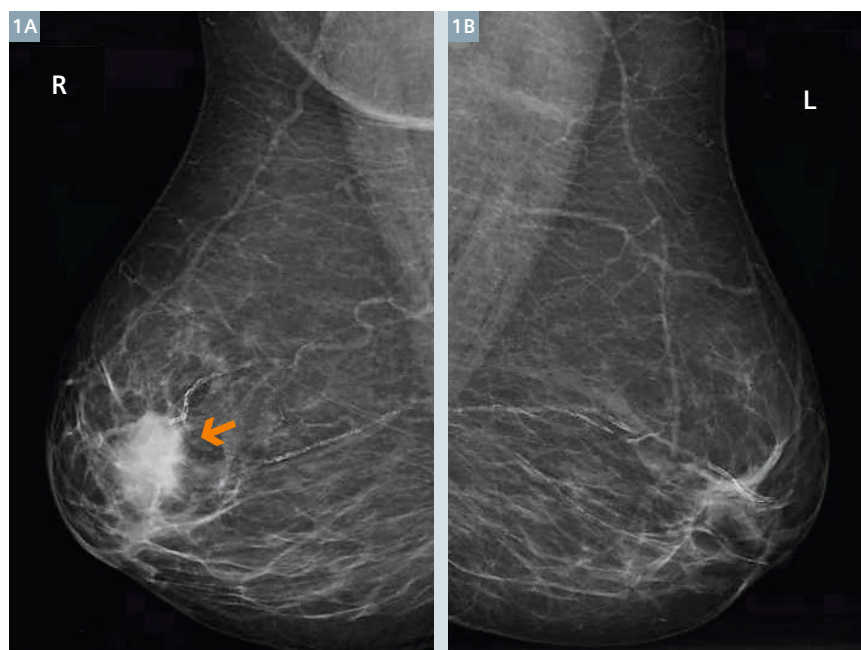
### Case report

A 69-year-old postmenopausal woman was presented to our breast clinic with a palpable mass in her right breast just above the nipple. She first noticed this mass one month prior to presentation. The mass was firm and non-tender.

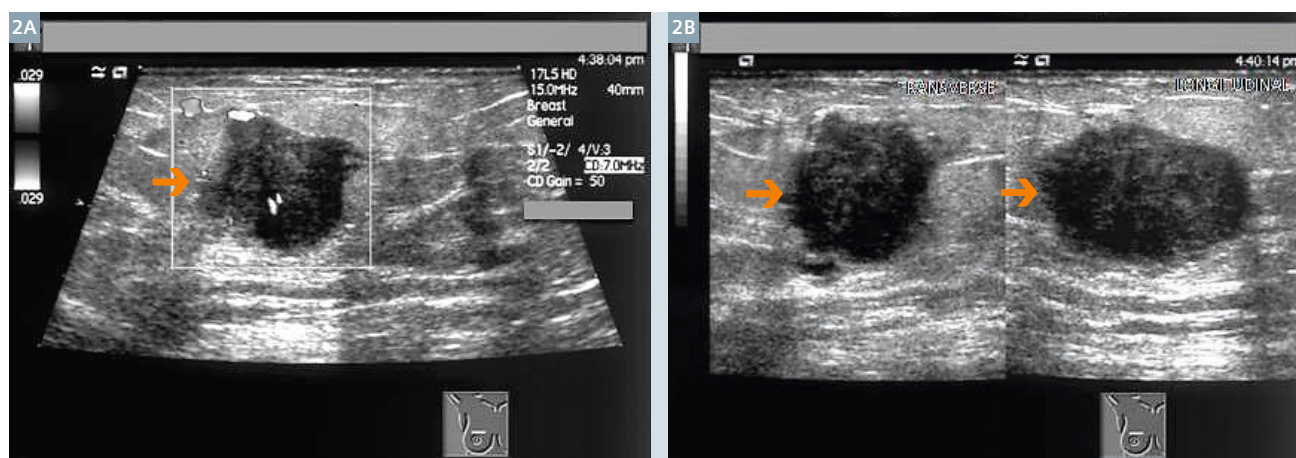
She received a mammogram, which revealed a 2.5 cm irregular, spiculated mass in the upper mid quadrant of the right breast (Fig. 1). Subsequent

ultrasound demonstrated an irregular heterogeneous mass in the area of the mammographic abnormality (Fig. 2). The axillary lymph nodes appeared to be normal.

MRM was performed, using a 1.5T MRI system (MAGNETOM Aera, Siemens Healthcare, Erlangen, Germany) and a dedicated breast coil. The images were obtained using a 2D dynamic protocol as described in Table 1. The images were evaluated and interpreted using the morphological and kinetic signs, described by Prof. Werner Kaiser [3]. MRI confirmed the presence of the mass that was demonstrated on mammo-



**1** Mammogram of both breasts in mediolateral oblique (MLO) view. A spiculated mass is seen in the right breast (arrow).



2 Sonographic image showing the mass in the right breast (arrows). It has heterogeneous echo-texture.

gram and ultrasound. It showed a centripetally enhancing, spiculated mass ('hook sign') measuring  $3.2 \times 2.4$  cm with heterogeneous internal enhancement and perifocal oedema (Fig. 3), dark in the T2-weighted images, specifically indicating a malignant lesion. However, the MRI additionally displayed a linear path of enhancement extending posteriorly from the mass towards the pectoralis muscle, invisible in mammography or ultrasound.

In the kinetic analysis (Fig. 4), this path of enhancement also displayed a suspicious washout in the delayed phase consistent with a type 3 curve. The underlying pectoralis muscles and the pectoral fatty layer were preserved.

The patient was then planned for conservative breast surgery (wide local excision – WLE) followed by radiotherapy. A periareolar incision

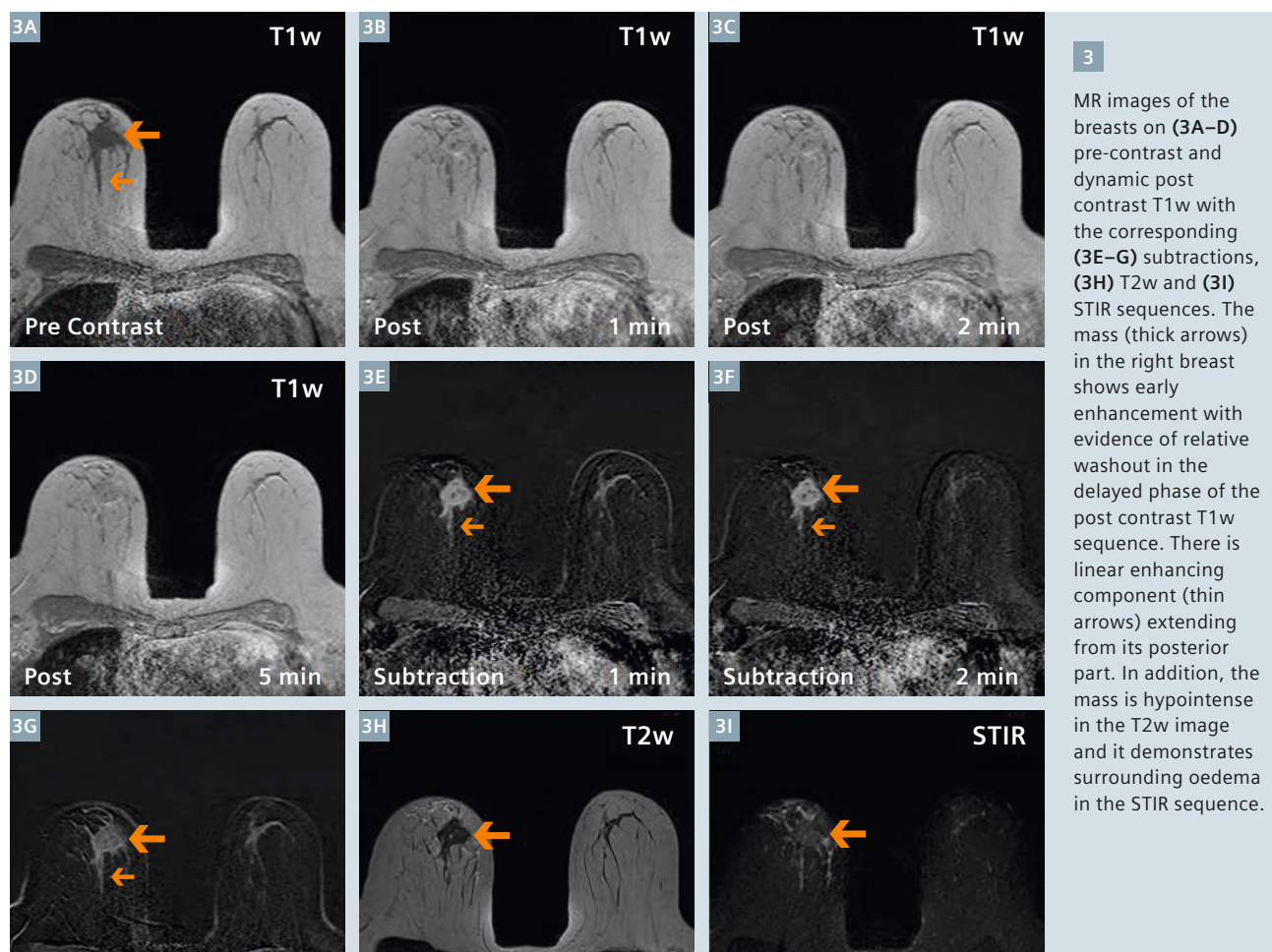
was made and a wide local excision of the tumor was performed including 1 cm rim of the tissue around the tumor. However in view of the suspicious linear extension of the tumor at its posterior aspect as seen on MRI, the excision posteriorly was extended up to the pectoralis major muscle. The sentinel node biopsy that was performed through an incision in the lower axillary hairline

Table 1: MRI examination protocol

Sequence no.	1. Nat cor	2. Dynamic* tra	3. CM cor	4. T2-TSE	5. STIR
Weighting	T1	T1	T1	T2	T2 (T1, 150 ms)
Puls sequence	FLASH	FLASH	FLASH	TSE	TSE
Orientation	coronal	transversal	coronal	transversal	transversal
TR (ms)	113	113	113	8900	8420
TE (ms)	4,6	4,6	4,6	207	70
Flip angle (°)	80	80	80	191	180
Slice thickness (mm)	3	3	3	3	3
Gap (mm)	0	0	0	0	0
Field-of-view (mm)	350	350	350	350	350
No. of slices	44	44	44	44	44
Matrix (pixels)	230 × 256	307 × 384	230 × 256	435 × 512	326 × 384

\*Connotation: dynamic study before and after the i.v. application of 0,1 mmol Gd-DTPA per kg body weight within 10 sec, followed by the injection of 30 ml saline via an automatic injector (Medrad, Spectris, Pittsburgh, USA) with 3 ml/s .





showed evidence of malignancy. A Level 2 axillary dissection was then carried out.

The histopathological examination of the mass revealed a poorly encapsulated malignant tumor. The cells were large and highly pleomorphic with minimal glandular formation. Further histopathological analysis of the resected tissue revealed deep extension of the tumor at its posterior part, corresponding to the aforementioned linear enhancement as demonstrated on MRI. Some of the sentinel nodes and the axillary nodes that were sent for sampling revealed involvement by the malignant tumor.

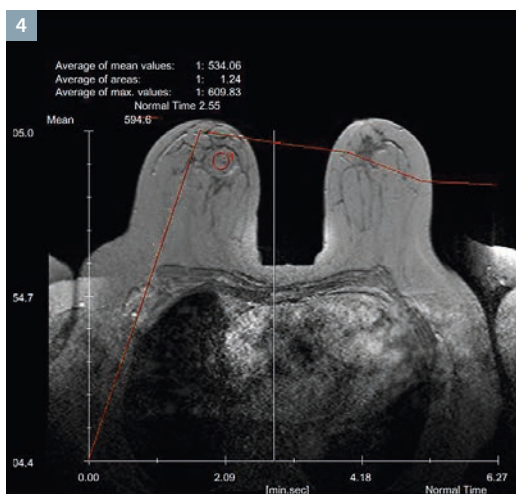
## Discussion

Breast cancer is the most common cancer in females in Malaysia. Malaysian women present at later stages

of breast cancer compared to counterparts in the developing countries where 30–40% present at stage 3 to stage 4 [4]. Mastectomy was the routine treatment for breast cancer until the 1980s [5]. The arrival of breast conservation surgery combined with radiation therapy offered major advantages with similarly low mortality rates [6]. Current surgical options for treating breast cancer are breast-conserving surgery (wide local excision and quadrantectomy) or mastectomy, taking into account the tumor size, multifocality or multicentricity, local extent versus distant spread, nodal status, and patient preference.

In patients with known malignancies further imaging with MRI can help in the preoperative choice of surgery and prevent increased reoperation rates.

The use of preoperative breast MRI for patients with newly diagnosed breast cancer is greatly controversial worldwide. Some articles published in major journals claim that routine preoperative breast MRI appears to confer no advantage over the standard diagnostic evaluations for newly diagnosed breast cancer [7]. Evaluation of the literature, however, reveals many differences in terms of technical aspects as well as reader experience. Nevertheless, studies have shown MRM to be more accurate than mammography and ultrasonography in defining the extent of tumor burden as characterized by tumor size and multifocality or multicentricity [3]. Some major multicenter studies claim that once MRM has been performed, conventional mammography and ultrasound are of no additional diagnostic use [8, 9]. Knowledge of the extent of disease prior to the



4 Time intensity curve showing suspicious washout in the delayed phase consistent with a type 3 curve.

surgery will help the surgeon and patient to make a more informed decision when presented with treatment options [3].

In the case of WLE the surgeon removes only the cancer and some of the normal-looking tissue around it (the margin). In our specific case, however, in view of the suspicious linear extension of the tumor at its posterior aspect as seen on MRI, the excision posteriorly was extended up to the pectoralis major. The posterior linear enhancement was confirmed to be the extension of the tumor on pathological diagnosis. MRM helped the surgeons in the preoperative planning and surgical approach of this case as the posterior extension

of the breast tumor could only and clearly be seen in MRI – not in mammogram or ultrasound. Following the surgery, the patient completed the chemoradiotherapy as part of the treatment. She was clinically well with no signs of recurrence during the last review at the clinic.

## Conclusion

In our case, the preoperative diagnosis of the posterior extension of the breast cancer was established by MRI. Our patient clearly benefited from MRM. For those battling cancer, preventing recurrence is of top priority. MRM can be an important imaging tool in helping women maintain that vigilance, even though some studies have not recommended preoperative MRI. Although the rate of recurrence after breast conservation is low, high-quality MRM (optimal technical standards and reader experience) is useful to minimize reoperation rates. Above all, women diagnosed with breast carcinoma should be offered the best possible chance for a successful treatment.

## Acknowledgement

We would like to acknowledge the Surgery Unit, Faculty of Medicine, Universiti Teknologi MARA.

*This article is dedicated to the late Professor Werner A. Kaiser who came to Malaysia and started Breast MRI services in our centre.*

## References

- 1 Mann RM, Kuhl CK, Kinkel K, Boetes C. Breast MRI: guidelines from the European Society of Breast Imaging. *Eur Radiol* 2008; 18:1307-18.
- 2 American College of Radiology. Breast Imaging Reporting and Data System® (BI-RADS®) 4. Reston, Va: American College of Radiology; 2003.
- 3 Kaiser WA. Signs in MR-Mammography. 1st ed. 2008. Corr. 2nd printing. Springer; 2009.
- 4 Dahlui M, Ramli S, Bulgiba AM. Breast cancer prevention and control programs in Malaysia. *Asian Pac J Cancer Prev* 2011; 12(6):1631-4.
- 5 Halsted WS. The Results of Operations for the Cure of Cancer of the Breast Performed at the Johns Hopkins Hospital from June, 1889, to January, 1894. *Ann Surg* 1894 Nov; 20(5):497-555.
- 6 Veronesi U, Cascinelli N, Mariani L, Greco M, Saccozzi R, Luini A, Aguilar M, Marubini E. Twenty-year follow-up of a randomized study comparing breast-conserving surgery with radical mastectomy for early breast cancer. *N Engl J Med*. 2002 Oct 17; 347(16):1227-32.
- 7 Houssami N, Turner R, Morrow M. Preoperative magnetic resonance imaging in breast cancer: meta-analysis of surgical outcomes. *nn Surg*. 2013 Feb; 257(2): 249-55. doi: 10.1097/SLA.0b013e31827a8d17.
- 8 Kuhl C, Weigel S, Schrading S, Arand B, Bieling H, König R, u. a. Prospective multicenter cohort study to refine management recommendations for women at elevated familial risk of breast cancer: the EVA trial. *J. Clin. Oncol*. 2010 March; 28(9):1450-7.
- 9 Sardanelli F, Podo F, Santoro F, Manoukian S, Bergonzi S, Trecate G, u. a. Multicenter surveillance of women at high genetic breast cancer risk using mammography, ultrasonography, and contrast-enhanced magnetic resonance imaging (the high breast cancer risk Italian 1 study): final results. *Invest Radiol*. 2011 Feb; 46(2): 94-105.

## Contact

Dr. Marymol Koshy  
Medical Imaging Unit  
Faculty of Medicine,  
Universiti Teknologi MARA  
Jalan Hospital, 47000  
Sungai Buloh  
Selangor Darul Ehsan  
Malaysia  
marymolkoshy@yahoo.com.sg



Dr. Marymol Koshy



Dr. Mohammad Hanafiah



Dr. Clemens Kaiser

# <sup>18</sup>F-FDG MR/PET as Compared with <sup>18</sup>F-FDG PET/CT. Initial Experiences in Patients with Metastatic Breast Cancer

Amy Melsaether, M.D.; Akshat C. Pujara, M.D.; Linda Moy, M.D.

New York University School of Medicine, Department of Radiology, New York, NY, USA

## Introduction

Current staging and surveillance for patients with metastatic breast cancer often involves <sup>18</sup>F-Fludeoxyglucose (FDG) PET/CT imaging. Limitations may include sensitivity for small bone metastases and decreased visualisation of brain and liver lesions due to high local physiological uptake [1, 2]. Moreover, breast cancer surveillance commonly entails serial <sup>18</sup>F-FDG PET/CT examinations. Given the relatively young age at diagnosis, cumulative radiation exposure is of particular concern in breast cancer patients [3]; the lifetime attributable risk of radiation induced cancer following a single <sup>18</sup>F-FDG PET/CT scan has been estimated to be 2/1000, and higher in young American women [3]. MR imaging involves no ionizing radiation and provides improved soft tissue contrast. Given these advantages, the effectiveness of MR for the initial staging of breast cancer and monitoring of distant metastases is being investigated [4-6].

The recent advent of combination 3T MRI and PET imaging in a state-of-the-art scanner potentiates fusion of the improved tissue contrast of MRI with functional PET data as well as increased patient safety by elimination of the radiation dose due to CT. With this new MR/PET hybrid technology, we acquired initial data comparing <sup>18</sup>F-FDG MR/PET to <sup>18</sup>F-FDG PET/CT in the evaluation of multi-organ metastatic disease in patients with a history of breast cancer on the basis of lesion detection and radiation dose. Imaging follow-up and comparison with prior studies served as our reference standard in cases where biopsy was not performed. Early findings

suggest lesion detection is high on PET/MRI for brain, liver and breast lesions, important sites of metastases and recurrences in breast cancer. Lung metastases appear to be seen equally well on PET/MRI and PET/CT, although infectious and non-specific lesions were better seen on PET/CT (not shown in these examples). In this article, we describe our imaging technique and demonstrate cases illustrative of our experience.

## Methods and imaging technique

This investigation is a Health Insurance Portability and Accountability Act-compliant and Institutional Review Board-approved protocol allows patients undergoing clinical <sup>18</sup>F-FDG PET/CT for evaluation for metastatic breast cancer to undergo <sup>18</sup>F-FDG PET/MRI immediately following their clinical PET/CT protocol. Informed written consent is obtained from all patients.

### PET/CT

Patients fasted for a minimum of four hours before imaging. Insulin was withheld six hours prior to imaging, and blood glucose concentration was verified to be less than 200 mg/dL. Approximately 60 minutes following intravenous administration of <sup>18</sup>F-FDG, patients underwent PET/CT imaging from skull to mid thighs (Siemens Biograph mCT). CT acquisition parameters were as follows: 120 kVp, 95 mA, 5.0 mm slice width, 50 cm transaxial field-of-view (FOV), 512 × 512 transaxial image matrix, B40f convolution kernel. PET acquisition parameters were as follows: Mean <sup>18</sup>F-FDG dose 14.8 ± 0.5 mCi,

2 minutes per bed position, 814 mm transaxial FOV, 221 mm axial FOV, 200 × 200 transaxial matrix, and 3 mm Gaussian post-reconstruction image filter. IV contrast was not routinely administered as per normal clinical usage. PET images were reconstructed with CT for attenuation correction with the attenuation-weighting ordered subsets expectation-maximization 3D (OSEM3D) algorithm at 2 iterations and 24 subsets. With these parameters, the transaxial voxel size was 4.07 × 4.07 mm and the axial voxel size was 2.03 mm. Total scan time is 15 minutes.

### PET/MRI

Immediately following PET/CT, patients were transferred to a nearby site for PET/MR imaging. No additional <sup>18</sup>F-FDG was injected. MRI and PET data were simultaneously acquired using the Siemens Biograph mMR system. The PET detector is composed of lutetium oxyorthosilicate scintillation (LSO) crystals attached to avalanche photodiodes (APD), replacing typical photomultiplier tubes for compatibility with MRI. Each block detector consists of 64 crystal elements, and each crystal measures 4 × 4 × 20 mm. In each ring there are 56 block detectors, and a total of 64 detector element rings arranged on the z-axis. The MRI unit is equipped with a 3 Tesla magnet.

After whole-body gradient echo scout, a whole-body PET/MRI exam was conducted including 6–7 bed positions from thighs to vertex, with the following protocols per station:

- 1) 3D coronal volumetric interpolated breath-hold examination (VIBE) Dixon for MR attenuation correction,



- 2) Prototype T1-weighted radial 3D gradient echo (Radial VIBE)\*, and
- 3) 2D double-refocused echo-planar, diffusion-weighted imaging (TR 6000 ms, TE 65 ms, FOV 450 mm,  $2.3 \times 2.3 \times 6.0$  mm voxel, spectral attenuated inversion recovery (SPAIR) fat-suppression, three diffusion directions (3-scan trace), and b-values 0, 350, and 700 s/mm<sup>2</sup>). Corresponding apparent diffusion coefficient (ADC) maps were generated. MR images were acquired prone with a set of flexible body matrix coils. PET events were simultaneously accumulated for six minutes per bed position and images were reconstructed on the vendor platform incorporating  $\mu$ -maps from the attenuation correction scan. Total scan time is 47 minutes.

### Image interpretation

PET/CT scans and PET/MRI scans were interpreted by board-certified radiologists on dedicated Miranda-64 workstations (Mirada). MRI images were separated from the PET/MRI study, sent to our PACS workstation (Philips) and also interpreted by a board-certified radiologist. All readers were blinded to patient history, pathology results and prior radiologic studies. The reference standard for metastatic lesion detection was a combination of comparison with prior and follow-up imaging and consensus amongst experienced nuclear medicine and MRI readers. Radiation dose was calculated using DLP conversion for CT [7] and mCi conversion for PET [8].

### Case 1

48-year-old woman with a history of left breast cancer diagnosed in 2003, which was treated with lumpectomy

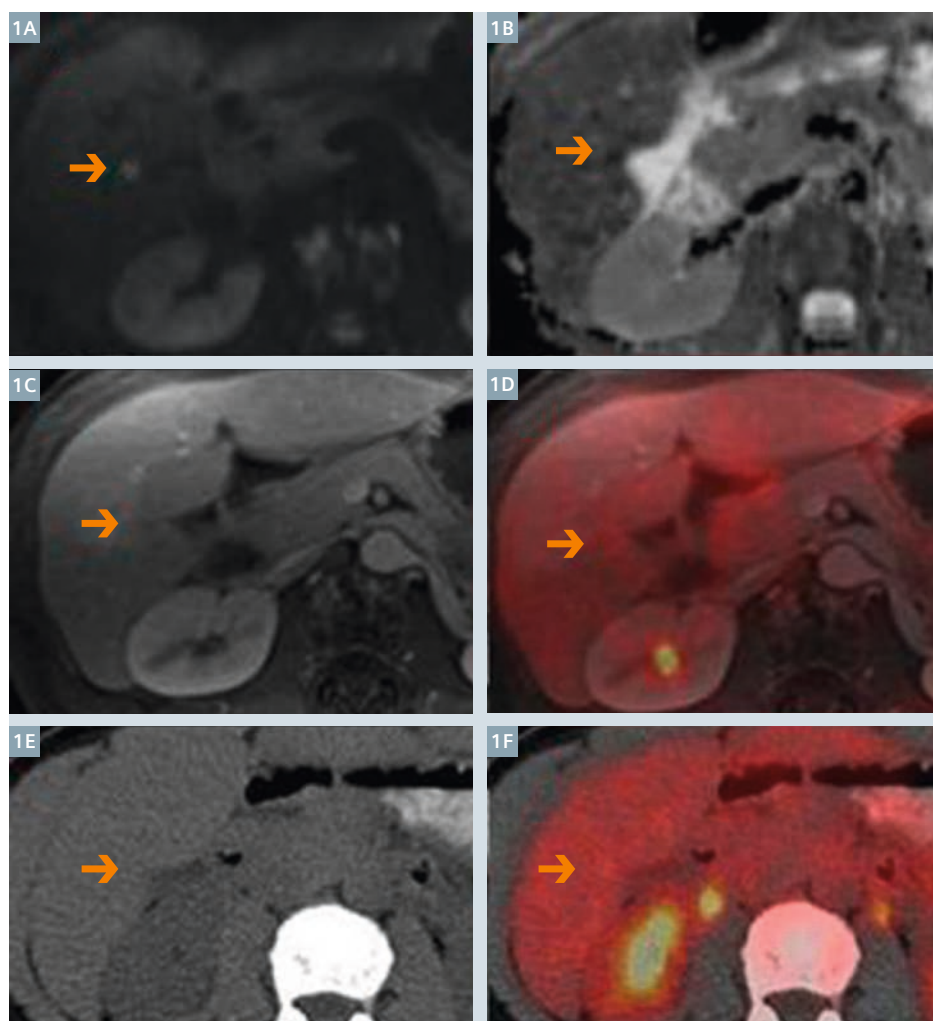
and radiation. The patient then presented with cough in December 2012, which was not responsive to over-the-counter medications. A chest radiograph in January 2013 demonstrated multiple masses consistent with metastatic disease. A core biopsy of a lung mass in February of 2013 yielded metastatic breast cancer.

### Imaging findings:

PET/MRI demonstrates widespread metastatic disease including osseous, nodal, pulmonary and hepatic metastases. These findings and comparison PET/CT images are detailed in figures 1 and 2.

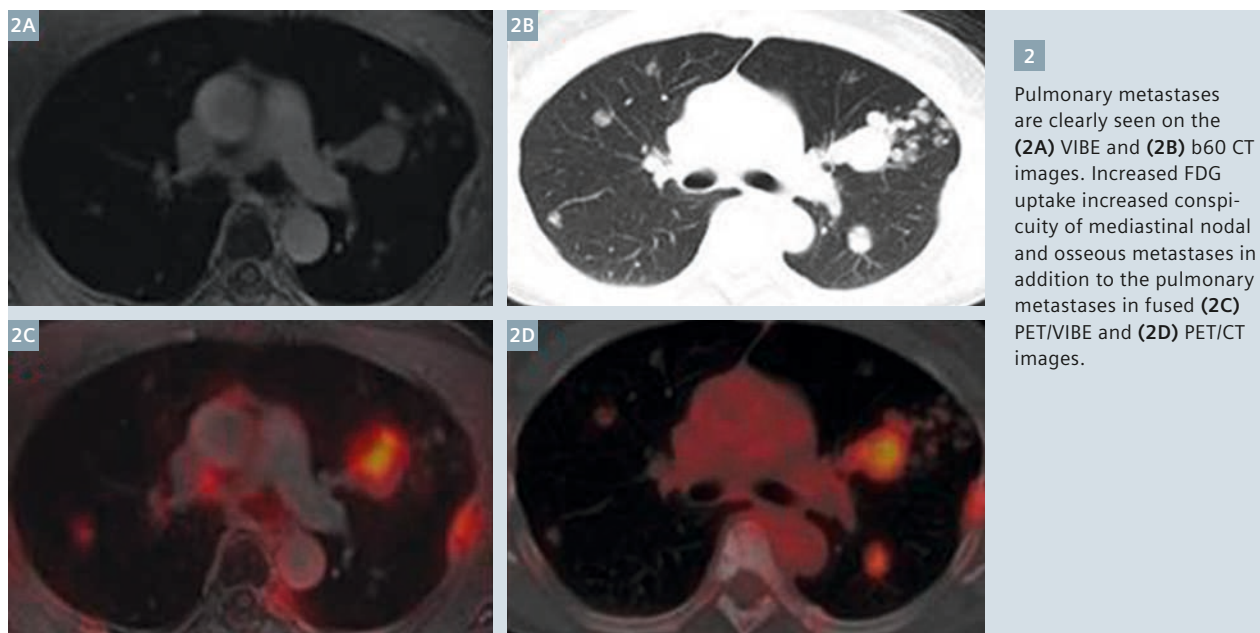
### Clinical follow-up:

In the setting of multi-organ metastatic disease, detection of liver metastases did not change treatment. The patient is maintained on Tamoxifen, Lupron and Xgeva.



1

A hepatic metastasis seen on PET/MRI but undetected on the PET/CT. The metastasis shown here is best seen as (1A) increased signal on the b350 sequence in the diffusion-weighted series and (1B) corresponding decreased signal on the apparent diffusion coefficient (ADC) map. The mass is less conspicuous on the (1C) VIBE image and (1D) faintly increased FDG uptake is seen on the fused PET/VIBE image. (1E) CT image, (1F) fused PET/CT. The faintly increased FDG uptake relative to background hepatic activity on the PET/MRI as compared with the PET/CT is likely related to the increased time to imaging.



## Case 2

53-year-old woman with history of locally advanced left breast cancer with positive axillary nodes diagnosed in August 2011, treated with neoadjuvant chemotherapy, mastectomy and free flap reconstruction. Prophylactic right mastectomy was also performed. Patient was also treated with Adriamycin, Herceptin

and Cytoxan, last cycle November 2012, and 5 weeks of radiation therapy, last cycle May 2012. New palpable left chest wall nodules underwent biopsy in August 2013 and were positive for recurrent disease.

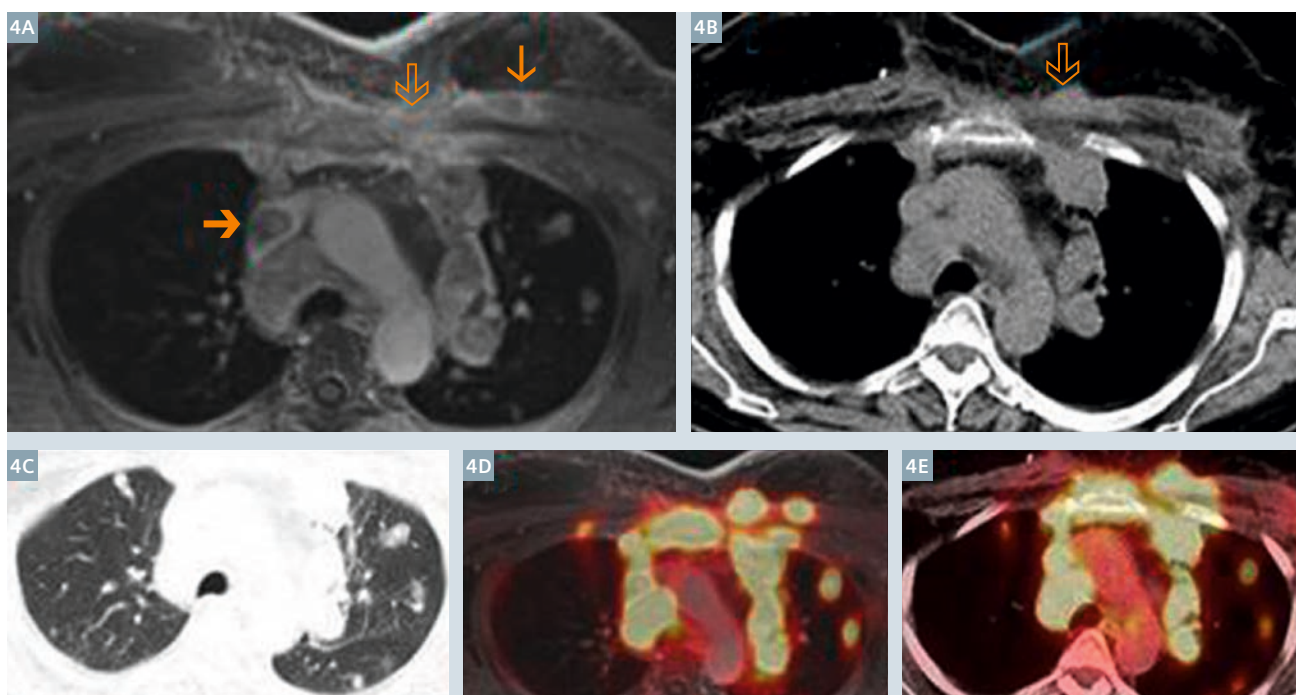
Imaging findings are detailed in figures 3 and 4.

### Clinical follow-up:

Patient underwent gamma knife radiation to the brain as a result of the PET/MRI findings. Due to the omission of CT, the estimated exposure was reduced by about 50%.



**3** (3A) PET/CT image near the level of the 4th ventricle. The tilt of the head is different on CT vs. MRI scans. MRI demonstrates cerebellar metastasis. The mass is clearly seen (3B) on a contrast-enhanced VIBE image. Corresponding PET data (3C).



**4** Chest wall, mediastinal nodal and pulmonary metastases are well seen on both PET/MRI and PET/CT. Notably, **(4A)** the VIBE image provides increased contrast resolution, clearly demonstrating muscle enhancement (thin arrow), chest wall invasion (open arrow) and nodal necrosis (thick arrow) while the **(4B)** b40 CT image demonstrates chest wall invasion (open arrow). Pulmonary metastases, as in the former case, are nearly as well seen on the VIBE image **(4A)** as on the b40 CT image **(4C)**. Fused **(4D)** PET/VIBE and **(4E)** PET/CT images highlight the markedly increased FDG uptake of these metastases.

### Case 3

50-year-old woman with a history of right breast cancer, diagnosed in August 2011. Her disease was metastatic to bone and liver at the time of diagnosis. Subsequently identified ovarian metastases were treated with oophorectomy. The patient is

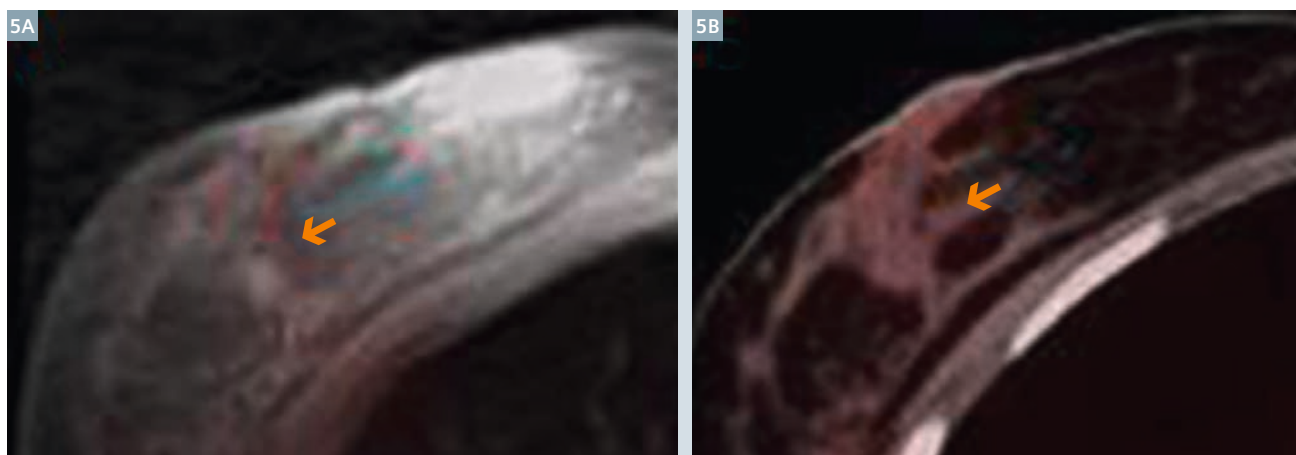
currently being treated with Arimidex and Xgeva.

Imaging findings are detailed in figures 5 and 6.

Clinical follow-up:

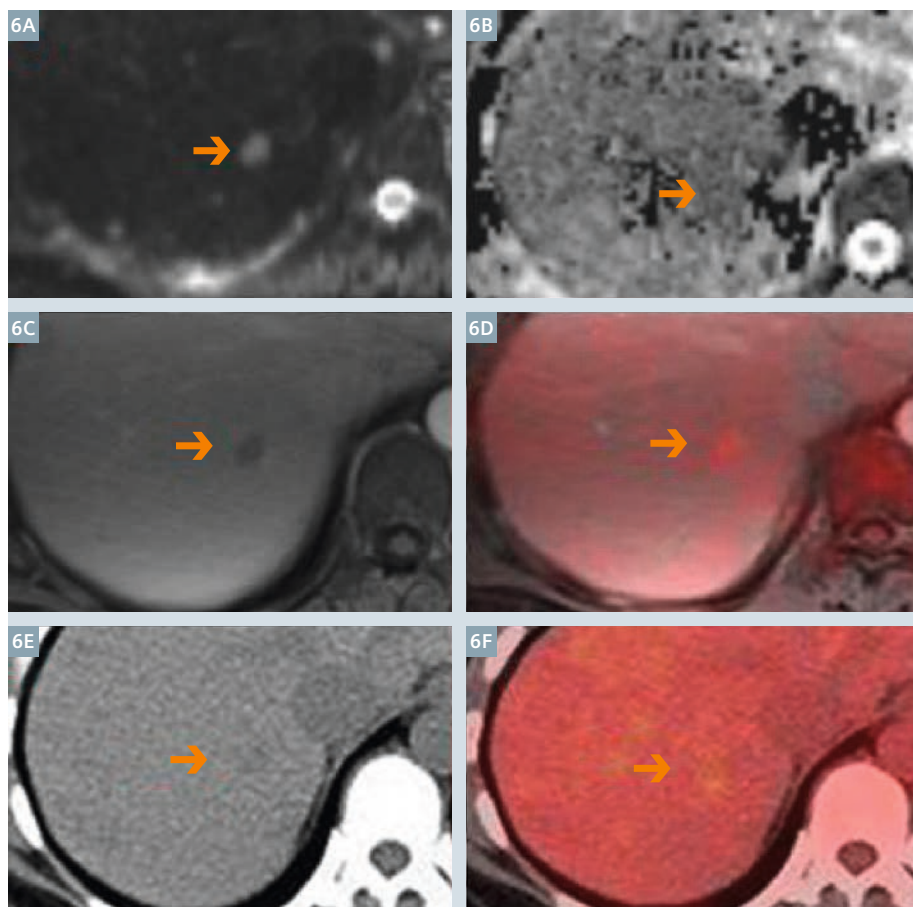
The patient is well maintained on

Xgeva. While the presence of residual liver metastases did not change drug choice, the patient is now followed with MR- rather than CT-based imaging in order to assess disease stability. Due to omission of CT, the estimated exposure was reduced by about 40%.



**5** In the right breast, the **(5A)** PET/VIBE sequence demonstrates a 5 mm spiculated breast mass, morphologically consistent with breast cancer and **(5B)** is not seen on PET/CT.





6

PET/MRI demonstrates liver metastases interpreted as resolved on PET/CT. Liver metastases are best seen (6A) as increased signal on the b350 sequence of the diffusion-weighted series and (6B) corresponding decreased signal on the ADC map. This mass can be delineated on the (6C) VIBE sequence and demonstrates mildly increased FDG uptake on (6D) the fused PET/VIBE image. Although the mass can be seen in retrospect on (6E) CT, it was not appreciated on the initial read. As in the first case, the increased PET activity relative to background hepatic activity on the (6D) PET/VIBE as compared with the (6F) PET/CT is likely related to the increased time to imaging.

## References

- 1 Moon DH, Maddahi J, Silverman DH, Glaspy JA, Phelps ME, Hoh CK. Accuracy of whole-body fluorine-<sup>18</sup>-FDG PET for the detection of recurrent or metastatic breast carcinoma. *J Nucl Med*. 1998 Mar;39(3):431-5.
- 2 Gallowitsch HJ, Kresnik E, Gasser J, Kumnig G, Igerc I, Mikosch P, Lind P. F-<sup>18</sup> fluorodeoxyglucose positron-emission tomography in the diagnosis of tumor recurrence and metastases in the follow-up of patients with breast carcinoma: a comparison to conventional imaging. *Invest Radiol*. 2003 May;38(5):250-6.
- 3 Huang B, Law MW, Khong PL. Whole-Body PET/CT Scanning: Estimation of Radiation Dose and Cancer Risk. *Radiology*. 2009 April;251(1):166-74.
- 4 Hausmann D, Kern C, Schröder MT, Sütterlin M, Schönberg SO, Neff KW, Dinter DJ. Whole-body MRI in preoperative diagnostics of breast cancer – a comparison with staging methods according to the s 3 guidelines. *Rofo*. 2011 Dec;183(12):1130-7.
- 5 Ohlmann-Knafo S, Kirschbaum M, Fenzl G, Pickuth D. Diagnostic value of whole-body MRI and bone scintigraphy in the detection of osseous metastases in patients with breast cancer – A Prospective Double-Blinded Study at two Hospital Centers. *Rofo*. 2009 Mar;181(3):255-63.
- 6 Schmidt GP, Baur-Melnyk A, Huag A, Heinemann V, Bauerfeind I, Reiser MF, Schoenberg SO. Comprehensive imaging of tumor recurrence in breast cancer patients using whole-body MRI at 1.5 and 3T compared to FDG-PET-CT. *Eur J Radiol*. 2008 Jan;65(1):47-58.
- 7 Huda W, Ogden KM, Khorasani MR. Converting dose-length product to effective dose at CT. *Radiology*. 2008 Sep;248(3):995-1003.
- 8 Brix G, Lechel U, Glatting G, Ziegler SI, Munzing W, Muller SP, Beyer T. Radiation exposure of patients undergoing whole-body dual-modality <sup>18</sup>F-FDG PET/CT examinations. *J Nucl Med* 2005 Apr;46(4):608-13.

\* Radial VIBE is a prototype for StarVIBE. StarVIBE is available for 1.5T MAGNETOM Aera and 3T MAGNETOM Skyra. Radial VIBE is WIP, the product is currently under development and is not for sale in the US and in other countries. Its future availability cannot be ensured.



## Contact

Amy Melsaether, M.D.  
New York University School of Medicine  
Department of Radiology  
Breast Imaging Section  
160 E 34<sup>th</sup> St, 3<sup>rd</sup> floor  
New York, NY 10014  
USA  
[amy.melsaether@nyumc.org](mailto:amy.melsaether@nyumc.org)

**HIGHLIGHTS OF PRESCRIBING****INFORMATION**

These highlights do not include all the information needed to use Fludeoxyglucose F 18 Injection safely and effectively. See full prescribing information for Fludeoxyglucose F 18 Injection.

**Fludeoxyglucose F 18 Injection, USP****For intravenous use**

Initial U.S. Approval: 2005

**RECENT MAJOR CHANGES****Warnings and Precautions**

(5.1, 5.2) 7/2010

Adverse Reactions (6) 7/2010

**INDICATIONS AND USAGE**

Fludeoxyglucose F18 Injection is indicated for positron emission tomography (PET) imaging in the following settings:

- **Oncology:** For assessment of abnormal glucose metabolism to assist in the evaluation of malignancy in patients with known or suspected abnormalities found by other testing modalities, or in patients with an existing diagnosis of cancer.
- **Cardiology:** For the identification of left ventricular myocardium with residual glucose metabolism and reversible loss of systolic function in patients with coronary artery disease and left ventricular dysfunction, when used together with myocardial perfusion imaging.
- **Neurology:** For the identification of regions of abnormal glucose metabolism associated with foci of epileptic seizures (1).

**DOSAGE AND ADMINISTRATION**

Fludeoxyglucose F 18 Injection emits radiation. Use procedures to minimize radiation exposure. Screen for blood glucose abnormalities.

- In the oncology and neurology settings, instruct patients to fast for 4 to 6 hours prior to the drug's injection. Consider medical therapy and laboratory testing to assure at least two days of normoglycemia prior to the drug's administration (5.2).
- In the cardiology setting, administration of glucose-containing food or liquids (e.g., 50 to 75 grams) prior to the drug's injection facilitates localization of cardiac ischemia (2.3).

Aseptically withdraw Fludeoxyglucose F 18 Injection from its container and administer by intravenous injection (2).

The recommended dose:

- for adults is 5 to 10 mCi (185 to 370 MBq), in all indicated clinical settings (2.1).
- for pediatric\* patients is 2.6 mCi in the neurology setting (2.2).

Initiate imaging within 40 minutes following drug injection; acquire static emission images 30 to 100 minutes from time of injection (2).

**DOSAGE FORMS AND STRENGTHS**

Multi-dose 30mL and 50mL glass vial containing 0.74 to 7.40 GBq/mL (20 to 200 mCi/mL) Fludeoxyglucose

F 18 Injection and 4.5mg of sodium chloride with 0.1 to 0.5% w/w ethanol as a stabilizer (approximately 15 to 50 mL volume) for intravenous administration (3).

**CONTRAINDICATIONS**

None

**WARNINGS AND PRECAUTIONS**

- Radiation risks: use smallest dose necessary for imaging (5.1).
- Blood glucose abnormalities: may cause suboptimal imaging (5.2).

**ADVERSE REACTIONS**

Hypersensitivity reactions have occurred; have emergency resuscitation equipment and personnel immediately available (6).

**To report SUSPECTED ADVERSE**

**REACTIONS, contact PETNET Solutions, Inc. at 877-473-8638 or FDA at 1-800-FDA-1088 or [www.fda.gov/medwatch](http://www.fda.gov/medwatch).**

**USE IN SPECIFIC POPULATIONS**

Pregnancy Category C: No human or animal data. Consider alternative diagnostics; use only if clearly needed (8.1).

- Nursing mothers: Use alternatives to breast feeding (e.g., stored breast milk or infant formula) for at least 10 half-lives of radioactive decay, if Fludeoxyglucose F 18 Injection is administered to a woman who is breast-feeding (8.3).

- Pediatric Use: Safety and effectiveness in pediatric patients have not been established in the oncology and cardiology settings (8.4).

**See 17 for PATIENT COUNSELING INFORMATION**

Revised: 1/2011

**FULL PRESCRIBING INFORMATION: CONTENTS\*****1 INDICATIONS AND USAGE**

- 1.1 Oncology
- 1.2 Cardiology
- 1.3 Neurology

**2 DOSAGE AND ADMINISTRATION**

- 2.1 Recommended Dose for Adults
- 2.2 Recommended Dose for Pediatric Patients
- 2.3 Patient Preparation
- 2.4 Radiation Dosimetry
- 2.5 Radiation Safety – Drug Handling
- 2.6 Drug Preparation and Administration
- 2.7 Imaging Guidelines

**3 DOSAGE FORMS AND STRENGTHS****4 CONTRAINDICATIONS****5 WARNINGS AND PRECAUTIONS**

- 5.1 Radiation Risks
- 5.2 Blood Glucose Abnormalities

**6 ADVERSE REACTIONS****7 DRUG INTERACTIONS****8 USE IN SPECIFIC POPULATIONS**

- 8.1 Pregnancy

**8.3 Nursing Mothers****8.4 Pediatric Use****11 DESCRIPTION****11.1 Chemical Characteristics****11.2 Physical Characteristics****12 CLINICAL PHARMACOLOGY****12.1 Mechanism of Action****12.2 Pharmacodynamics****12.3 Pharmacokinetics****13 NONCLINICAL TOXICOLOGY****13.1 Carcinogenesis, Mutagenesis, Impairment of Fertility****14 CLINICAL STUDIES****14.1 Oncology****14.2 Cardiology****14.3 Neurology****15 REFERENCES****16 HOW SUPPLIED/STORAGE AND DRUG HANDLING****17 PATIENT COUNSELING INFORMATION**

\* Sections or subsections omitted from the full prescribing information are not listed.

**FULL PRESCRIBING INFORMATION****1 INDICATIONS AND USAGE**

Fludeoxyglucose F 18 Injection is indicated for positron emission tomography (PET) imaging in the following settings:

**1.1 Oncology**

For assessment of abnormal glucose metabolism to assist in the evaluation of malignancy in patients with known or suspected abnormalities found by other testing modalities, or in patients with an existing diagnosis of cancer.

**1.2 Cardiology**

For the identification of left ventricular myocardium with residual glucose metabolism

and reversible loss of systolic function in patients with coronary artery disease and left ventricular dysfunction, when used together with myocardial perfusion imaging.

**1.3 Neurology**

For the identification of regions of abnormal glucose metabolism associated with foci of epileptic seizures.

**2 DOSAGE AND ADMINISTRATION**

Fludeoxyglucose F 18 Injection emits radiation. Use procedures to minimize radiation exposure. Calculate the final dose from the end of synthesis (EOS) time using proper radioactive decay factors. Assay the final dose in a properly calibrated dose calibrator before administration to the patient [see Description (11.2)].

**2.1 Recommended Dose for Adults**

Within the oncology, cardiology and neurology settings, the recommended dose for adults is 5 to 10 mCi (185 to 370 MBq) as an intravenous injection.

**2.2 Recommended Dose for Pediatric Patients**

Within the neurology setting, the recommended dose for pediatric patients is 2.6 mCi, as an intravenous injection. The optimal dose adjustment on the basis of body size or weight has not been determined [see Use in Special Populations (8.4)].

**2.3 Patient Preparation**

- To minimize the radiation absorbed dose to the bladder, encourage adequate hydration. Encourage the patient to drink water or other fluids (as tolerated) in the 4 hours before their PET study.
- Encourage the patient to void as soon as the imaging study is completed and as often as possible thereafter for at least one hour.
- Screen patients for clinically significant blood glucose abnormalities by obtaining a history and/or laboratory tests [see Warnings and Precautions (5.2)]. Prior to Fludeoxyglucose F 18 PET imaging in the oncology and neurology settings, instruct patient to fast for 4 to 6 hours prior to the drug's injection.
- In the cardiology setting, administration of glucose-containing food or liquids (e.g., 50 to 75 grams) prior to Fludeoxyglucose F18 Injection facilitates localization of cardiac ischemia

**2.4 Radiation Dosimetry**

The estimated human absorbed radiation doses (rem/mCi) to a newborn (3.4 kg), 1-year old (9.8 kg), 5-year old (19 kg), 10-year old (32 kg), 15-year old (57 kg), and adult (70 kg) from intravenous administration of Fludeoxyglucose F 18 Injection are shown in Table 1. These estimates were calculated based on human<sup>2</sup> data and using the data published by the International Commission on Radiological Protection<sup>4</sup> for Fludeoxyglucose <sup>18</sup>F. The dosimetry data show that there are slight variations in absorbed radiation dose for various organs in each of the age groups. These dissimilarities in absorbed radiation dose are due to developmental age variations (e.g., organ size, location, and overall metabolic rate for each age group). The identified critical organs (in descending order) across all age groups evaluated are the urinary bladder, heart, pancreas, spleen, and lungs.

**Table 1. Estimated Absorbed Radiation Doses (rem/mCi) After Intravenous Administration of Fludeoxyglucose F-18 Injection<sup>a</sup>**

Organ	Newborn (3.4 kg)	1-year old (9.8 kg)	5-year old (19 kg)	10-year old (32 kg)	15-year old (57 kg)	Adult (70 kg)
Bladder wall <sup>b</sup>	4.3	1.7	0.93	0.60	0.40	0.32
Heart wall	2.4	1.2	0.70	0.44	0.29	0.22
Pancreas	2.2	0.68	0.33	0.25	0.13	0.096
Spleen	2.2	0.84	0.46	0.29	0.19	0.14
Lungs	0.96	0.38	0.20	0.13	0.092	0.064
Kidneys	0.81	0.34	0.19	0.13	0.089	0.074
Ovaries	0.80	0.8	0.19	0.11	0.058	0.053
Uterus	0.79	0.35	0.19	0.12	0.076	0.062
LLI wall *	0.69	0.28	0.15	0.097	0.060	0.051
Liver	0.69	0.31	0.17	0.11	0.076	0.058
Gallbladder wall	0.69	0.26	0.14	0.093	0.059	0.049
Small intestine	0.68	0.29	0.15	0.096	0.060	0.047
ULI wall **	0.67	0.27	0.15	0.090	0.057	0.046
Stomach wall	0.65	0.27	0.14	0.089	0.057	0.047
Adrenals	0.65	0.28	0.15	0.095	0.061	0.048
Testes	0.64	0.27	0.14	0.085	0.052	0.041
Red marrow	0.62	0.26	0.14	0.089	0.057	0.047
Thymus	0.61	0.26	0.14	0.086	0.056	0.044
Thyroid	0.61	0.26	0.13	0.080	0.049	0.039
Muscle	0.58	0.25	0.13	0.078	0.049	0.039
Bone surface	0.57	0.24	0.12	0.079	0.052	0.041
Breast	0.54	0.22	0.11	0.068	0.043	0.034
Skin	0.49	0.20	0.10	0.060	0.037	0.030
Brain	0.29	0.13	0.09	0.078	0.072	0.070
Other tissues	0.59	0.25	0.13	0.083	0.052	0.042

<sup>a</sup> MIRDOSE 2 software was used to calculate the radiation absorbed dose. Assumptions on the biodistribution based on data from Gallagher et al.1 and Jones et al.2

<sup>b</sup> The dynamic bladder model with a uniform voiding frequency of 1.5 hours was used. \*LLI = lower large intestine; \*\*ULI = upper large intestine

\* MR scanning has not been established as safe for imaging fetuses and infants under two years of age.

The responsible physician must evaluate the benefit of the MRI examination in comparison to other imaging procedures.

**2.5 Radiation Safety – Drug Handling**

- Use waterproof gloves, effective radiation shielding, and appropriate safety measures when handling Fludeoxyglucose F 18 Injection to avoid unnecessary radiation exposure to the patient, occupational workers, clinical personnel and other persons.
- Radiopharmaceuticals should be used by or under the control of physicians who are qualified by specific training and experience in the safe use and handling of radionuclides, and whose experience and training have been approved by the appropriate governmental agency authorized to license the use of radionuclides.
- Calculate the final dose from the end of synthesis (EOS) time using proper radioactive decay factors. Assay the final dose in a properly calibrated dose calibrator before administration to the patient [see Description (11.2)].
- The dose of Fludeoxyglucose F 18 used in a given patient should be minimized consistent with the objectives of the procedure, and the nature of the radiation detection devices employed.

**2.6 Drug Preparation and Administration**

- Calculate the necessary volume to administer based on calibration time and dose.
- Aseptically withdraw Fludeoxyglucose F 18 Injection from its container.
- Inspect Fludeoxyglucose F 18 Injection visually for particulate matter and discoloration before administration, whenever solution and container permit.
- Do not administer the drug if it contains particulate matter or discoloration; dispose of these unacceptable or unused preparations in a safe manner, in compliance with applicable regulations.
- Use Fludeoxyglucose F 18 Injection within 12 hours from the EOS.

**2.7 Imaging Guidelines**

- Initiate imaging within 40 minutes following Fludeoxyglucose F 18 Injection administration.
- Acquire static emission images 30 to 100 minutes from the time of injection.

**3 DOSAGE FORMS AND STRENGTHS**

Multiple-dose 30 mL and 50 mL glass vial containing 0.74 to 7.40 GBq/mL (20 to 200 mCi/mL) of Fludeoxyglucose F 18 Injection and 4.5 mg of sodium chloride with 0.1 to 0.5% w/w ethanol as a stabilizer (approximately 15 to 50 mL volume) for intravenous administration.

**4 CONTRAINDICATIONS**

None

**5 WARNINGS AND PRECAUTIONS****5.1 Radiation Risks**

Radiation-emitting products, including Fludeoxyglucose F 18 Injection, may increase the risk for cancer, especially in pediatric patients. Use the smallest dose necessary for imaging and ensure safe handling to protect the patient and health care worker [see Dosage and Administration (2.5)].

**5.2 Blood Glucose Abnormalities**

In the oncology and neurology setting, suboptimal imaging may occur in patients with inadequately regulated blood glucose levels. In these patients, consider medical therapy and laboratory testing to assure at least two days of normoglycemia prior to Fludeoxyglucose F 18 Injection administration.

**6 ADVERSE REACTIONS**

Hypersensitivity reactions with pruritus, edema and rash have been reported in the post-marketing setting. Have emergency resuscitation equipment and personnel immediately available.

**7 DRUG INTERACTIONS**

The possibility of interactions of Fludeoxyglucose F 18 Injection with other drugs taken by patients undergoing PET imaging has not been studied.

**8 USE IN SPECIFIC POPULATIONS****8.1 Pregnancy**

Pregnancy Category C

Animal reproduction studies have not been conducted with Fludeoxyglucose F 18 Injection. It is also not known whether Fludeoxyglucose F 18 Injection can cause fetal harm when administered to a pregnant woman or can affect reproduction capacity. Consider alternative diagnostic tests in a pregnant woman; administer Fludeoxyglucose F 18 Injection only if clearly needed.

**8.3 Nursing Mothers**

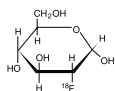
It is not known whether Fludeoxyglucose F 18 Injection is excreted in human milk. Consider alternative diagnostic tests in women who are breast-feeding. Use alternatives to breast feeding (e.g., stored breast milk or infant formula) for at least 10 half-lives of radioactive decay, if Fludeoxyglucose F 18 Injection is administered to a woman who is breast-feeding.

**8.4 Pediatric Use**

The safety and effectiveness of Fludeoxyglucose F 18 Injection in pediatric patients with epilepsy is established on the basis of studies in adult and pediatric patients. In pediatric patients with epilepsy, the recommended dose is 2.6 mCi. The optimal dose adjustment on the basis of body size or weight has not been determined. In the oncology or cardiology settings, the safety and effectiveness of Fludeoxyglucose F 18 Injection have not been established in pediatric patients.

**11 DESCRIPTION****11.1 Chemical Characteristics**

Fludeoxyglucose F 18 Injection is a positron emitting radiopharmaceutical that is used for diagnostic purposes in conjunction with positron emission tomography (PET) imaging. The active ingredient 2-deoxy-2-[<sup>18</sup>F]fluoro-D-glucose has the molecular formula of C<sub>6</sub>H<sub>11</sub><sup>18</sup>FO<sub>5</sub> with a molecular weight of 181.26, and has the following chemical structure:



Fludeoxyglucose F 18 Injection is provided as a ready to use sterile, pyrogen free, clear, colorless solution. Each mL contains between 0.740 to 7.40GBq (20.0 to 200 mCi) of

2-deoxy-2-[<sup>18</sup>F]fluoro-D-glucose at the EOS, 4.5 mg of sodium chloride and 0.1 to 0.5% w/w ethanol as a stabilizer. The pH of the solution is between 4.5 and 7.5. The solution is packaged in a multiple-dose glass vial and does not contain any preservative.

**11.2 Physical Characteristics**

Fluorine F 18 decays by emitting positron to Oxygen O 16 (stable) and has a physical half-life of 109.7 minutes. The principal photons useful for imaging are the dual 511 keV gamma photons, that are produced and emitted simultaneously in opposite direction when the positron interacts with an electron (Table 2).

**Table 2. Principal Radiation Emission Data for Fluorine F18**

Radiation/Emission	% Per Disintegration	Mean Energy
Positron (b+)	96.73	249.8 keV
Gamma (±)*	193.46	511.0 keV

\*Produced by positron annihilation

From: Kocher, D.C. Radioactive Decay Tables DOE/TIC-11026, 89 (1981)

The specific gamma ray constant (point source air kerma coefficient) for fluorine F 18 is 5.7 R/hr/mCi (1.35 x 10<sup>-6</sup> Gy/hr/kBq) at 1 cm. The half-value layer (HVL) for the 511 keV photons is 4 mm lead (Pb). The range of attenuation coefficients for this radionuclide as a function of lead shield thickness is shown in Table 3. For example, the interposition of an 8 mm thickness of Pb, with a coefficient of attenuation of 0.25, will decrease the external radiation by 75%.

**Table 3. Radiation Attenuation of 511 keV Photons by lead (Pb) shielding**

Shield thickness (Pb) mm	Coefficient of attenuation
0	0.00
4	0.50
8	0.25
13	0.10
26	0.01
39	0.001
52	0.0001

For use in correcting for physical decay of this radionuclide, the fractions remaining at selected intervals after calibration are shown in Table 4.

**Table 4. Physical Decay Chart for Fluorine F18**

Minutes	Fraction Remaining
0*	1.000
15	0.909
30	0.826
60	0.683
110	0.500
220	0.250

\*calibration time

**12 CLINICAL PHARMACOLOGY****12.1 Mechanism of Action**

Fludeoxyglucose F 18 is a glucose analog that concentrates in cells that rely upon glucose as an energy source, or in cells whose dependence on glucose increases under pathological conditions. Fludeoxyglucose F 18 is transported through the cell membrane by facilitative glucose transporter proteins and is phosphorylated within the cell to [<sup>18</sup>F] FDG-6-phosphate by the enzyme hexokinase. Once phosphorylated it cannot exit until it is dephosphorylated by glucose-6-phosphatase. Therefore, within a given tissue or pathophysiological process, the retention and clearance of Fludeoxyglucose F 18 reflect a balance involving glucose transporter, hexokinase and glucose-6-phosphatase activities. When allowance is made for the kinetic differences between glucose and Fludeoxyglucose F 18 transport and phosphorylation (expressed as the 'lumped constant' ratio), Fludeoxyglucose F 18 is used to assess glucose metabolism.

In comparison to background activity of the specific organ or tissue type, regions of decreased or absent uptake of Fludeoxyglucose F 18 reflect the decrease or absence of glucose metabolism. Regions of increased uptake of Fludeoxyglucose F 18 reflect greater than normal rates of glucose metabolism.

**12.2 Pharmacodynamics**

Fludeoxyglucose F 18 Injection is rapidly distributed to all organs of the body after intravenous administration. After background clearance of Fludeoxyglucose F 18 Injection, optimal PET imaging is generally achieved between 30 to 40 minutes after administration.

In cancer, the cells are generally characterized by enhanced glucose metabolism partially due to (1) an increase in activity of glucose transporters, (2) an increased rate of phosphorylation activity, (3) a reduction of phosphatase activity or, (4) a dynamic alteration in the balance among all these processes. However, glucose metabolism of cancer as reflected by Fludeoxyglucose F 18 accumulation shows considerable variability. Depending on tumor type, stage, and location, Fludeoxyglucose F 18 accumulation may be increased, normal, or decreased. Also, inflammatory cells can have the same variability of uptake of Fludeoxyglucose F 18.

In the heart, under normal aerobic conditions, the myocardium meets the bulk of its energy requirements by oxidizing free fatty acids. Most of the exogenous glucose taken up by the myocyte is converted into glycogen. However, under ischemic conditions, the oxidation of free fatty acids decreases, exogenous glucose becomes the preferred myocardial substrate, glycolysis is stimulated, and glucose taken up by the myocyte is metabolized immediately instead of being converted into glycogen. Under these condi-



tions, phosphorylated Fludeoxyglucose F 18 accumulates in the myocyte and can be detected with PET imaging.

In the brain, cells normally rely on aerobic metabolism. In epilepsy, the glucose metabolism varies. Generally, during a seizure, glucose metabolism increases. Interictally, the seizure focus tends to be hypometabolic.

### 12.3 Pharmacokinetics

**Distribution:** In four healthy male volunteers, receiving an intravenous administration of 30 seconds in duration, the arterial blood level profile for Fludeoxyglucose F 18 decayed triexponentially. The effective half-life ranges of the three phases were 0.2 to 0.3 minutes, 10 to 13 minutes with a mean and standard deviation (STD) of 11.6 ( $\pm$ ) 1.1 min, and 80 to 95 minutes with a mean and STD of 88 ( $\pm$ ) 4 min.

Plasma protein binding of Fludeoxyglucose F 18 has not been studied.

**Metabolism:** Fludeoxyglucose F 18 is transported into cells and phosphorylated to [ $^{18}$ F]-FDG-6-phosphate at a rate proportional to the rate of glucose utilization within that tissue. [F18]-FDG-6-phosphate presumably is metabolized to 2-deoxy-2-[F18]fluoro-6-phospho-D-mannose([F 18]FDM-6-phosphate).

Fludeoxyglucose F 18 Injection may contain several impurities (e.g., 2-deoxy-2-chloro-D-glucose (CIDG)). Biodistribution and metabolism of CIDG are presumed to be similar to Fludeoxyglucose F 18 and would be expected to result in intracellular formation of 2-deoxy-2-chloro-6-phospho-D-glucose (CIDG-6-phosphate) and 2-deoxy-2-chloro-6-phospho-D-mannose (CIDM-6-phosphate). The phosphorylated deoxyglucose compounds are dephosphorylated and the resulting compounds (FDG, FDM, CIDG, and CIDM) presumably leave cells by passive diffusion. Fludeoxyglucose F 18 and related compounds are cleared from non-cardiac tissues within 3 to 24 hours after administration. Clearance from the cardiac tissue may require more than 96 hours. Fludeoxyglucose F 18 that is not involved in glucose metabolism in any tissue is then excreted in the urine.

**Elimination:** Fludeoxyglucose F 18 is cleared from most tissues within 24 hours and can be eliminated from the body unchanged in the urine. Three elimination phases have been identified in the reviewed literature. Within 33 minutes, a mean of 3.9% of the administered radioactive dose was measured in the urine. The amount of radiation exposure of the urinary bladder at two hours post-administration suggests that 20.6% (mean) of the radioactive dose was present in the bladder.

#### Special Populations:

The pharmacokinetics of Fludeoxyglucose F 18 Injection have not been studied in renally-impaired, hepatically impaired or pediatric patients. Fludeoxyglucose F 18 is eliminated through the renal system. Avoid excessive radiation exposure to this organ system and adjacent tissues.

The effects of fasting, varying blood sugar levels, conditions of glucose intolerance, and diabetes mellitus on Fludeoxyglucose F 18 distribution in humans have not been ascertained [see Warnings and Precautions (5.2)].

### 13 NONCLINICAL TOXICOLOGY

#### 13.1 Carcinogenesis, Mutagenesis, Impairment of Fertility

Animal studies have not been performed to evaluate the Fludeoxyglucose F 18 Injection carcinogenic potential, mutagenic potential or effects on fertility.

### 14 CLINICAL STUDIES

#### 14.1 Oncology

The efficacy of Fludeoxyglucose F 18 Injection in positron emission tomography cancer imaging was demonstrated in 16 independent studies. These studies prospectively evaluated the use of Fludeoxyglucose F 18 in patients with suspected or known malignancies, including non-small cell lung cancer, colo-rectal, pancreatic, breast, thyroid, melanoma, Hodgkin's and non-Hodgkin's lymphoma, and various types of metastatic cancers to lung, liver, bone, and axillary nodes. All these studies had at least 50 patients and used pathology as a standard of truth. The Fludeoxyglucose F 18 Injection doses in the studies ranged from 200 MBq to 740 MBq with a median and mean dose of 370 MBq.

In the studies, the diagnostic performance of Fludeoxyglucose F 18 Injection varied with the type of cancer, size of cancer, and other clinical conditions. False negative and false positive scans were observed. Negative Fludeoxyglucose F 18 Injection PET scans do not exclude the diagnosis of cancer. Positive Fludeoxyglucose F 18 Injection PET scans can not replace pathology to establish a diagnosis of cancer. Non-malignant conditions such as fungal infections, inflammatory processes and benign tumors have patterns of increased glucose metabolism that may give rise to false-positive scans. The efficacy of Fludeoxyglucose F 18 Injection PET imaging in cancer screening was not studied.

#### 14.2 Cardiology

The efficacy of Fludeoxyglucose F 18 Injection for cardiac use was demonstrated in ten independent, prospective studies of patients with coronary artery disease and chronic left ventricular systolic dysfunction who were scheduled to undergo coronary revascularization. Before revascularization, patients underwent PET imaging with Fludeoxyglucose F 18 Injection (74 to 370 MBq, 2 to 10 mCi) and perfusion imaging with other diagnostic radiopharmaceuticals. Doses of Fludeoxyglucose F 18 Injection ranged from 74 to 370 MBq (2 to 10 mCi). Segmental, left ventricular, wall-motion assessments of asynergic areas made before revascularization were compared in a blinded manner to assessments made after successful revascularization to identify myocardial segments with functional recovery.

Left ventricular myocardial segments were predicted to have reversible loss of systolic function if they showed Fludeoxyglucose F 18 accumulation and reduced perfusion (i.e., flow-metabolism mismatch). Conversely, myocardial segments were predicted to have irreversible loss of systolic function if they showed reductions in both Fludeoxyglucose F 18 accumulation and perfusion (i.e., matched defects).

Findings of flow-metabolism mismatch in a myocardial segment may suggest that successful revascularization will restore myocardial function in that segment. However, false-positive tests occur regularly, and the decision to have a patient undergo revascularization should not be based on PET findings alone. Similarly, findings of a matched defect in a myocardial segment may suggest that myocardial function will not recover in that segment, even if it is successfully revascularized. However, false-negative tests occur regularly, and the decision to recommend against coronary revascularization, or to recommend a cardiac transplant, should not be based on PET findings alone. The reversibility of segmental dysfunction as predicted with Fludeoxyglucose F 18 PET imaging depends on success-

ful coronary revascularization. Therefore, in patients with a low likelihood of successful revascularization, the diagnostic usefulness of PET imaging with Fludeoxyglucose F 18 Injection is more limited.

### 14.3 Neurology

In a prospective, open label trial, Fludeoxyglucose F 18 Injection was evaluated in 86 patients with epilepsy. Each patient received a dose of Fludeoxyglucose F 18 Injection in the range of 185 to 370 MBq (5 to 10 mCi). The mean age was 16.4 years (range: 4 months to 58 years; of these, 42 patients were less than 12 years and 16 patients were less than 2 years old). Patients had a known diagnosis of complex partial epilepsy and were under evaluation for surgical treatment of their seizure disorder. Seizure foci had been previously identified on ictal EEGs and sphenoidal EEGs. Fludeoxyglucose F 18 Injection PET imaging confirmed previous diagnostic findings in 16% (14/87) of the patients; in 34% (30/87) of the patients, Fludeoxyglucose F 18 Injection PET images provided new findings. In 32% (27/87), imaging with Fludeoxyglucose F 18 Injection was inconclusive. The impact of these imaging findings on clinical outcomes is not known. Several other studies comparing imaging with Fludeoxyglucose F 18 Injection results to subsphenoidal EEG, MRI and/or surgical findings supported the concept that the degree of hypometabolism corresponds to areas of confirmed epileptogenic foci. The safety and effectiveness of Fludeoxyglucose F 18 Injection to distinguish idiopathic epileptogenic foci from tumors or other brain lesions that may cause seizures have not been established.

### 15 REFERENCES

- Gallagher B.M., Ansari A., Atkins H., Casella V., Christman D.R., Fowler J.S., Ido T., MacGregor R.R., Som P., Wan C.N., Wolf A.P., Kuhl D.E., and Reivich M. "Radiopharmaceuticals XXVII. 18F-labeled 2-deoxy-2-fluoro-D-glucose as a radiopharmaceutical for measuring regional myocardial glucose metabolism in vivo: tissue distribution and imaging studies in animals," J Nucl Med, 1977; 18, 990-6.
- Jones S.C., Alavi A., Christman D., Montanez, I., Wolf, A.P., and Reivich M. "The radiation dosimetry of 2 [F-18] fluoro-2-deoxy-D-glucose in man," J Nucl Med, 1982; 23, 613-617.
- Kocher, D.C. "Radioactive Decay Tables: A handbook of decay data for application to radiation dosimetry and radiological assessments," 1981, DOE/ITIC-1 1026, 89.
- ICRP Publication 53, Volume 18, No. I-4, 1987, pages 75-76.

### 16 HOW SUPPLIED/STORAGE AND DRUG HANDLING

Fludeoxyglucose F 18 Injection is supplied in a multi-dose, capped 30 mL and 50 mL glass vial containing between 0.740 to 7.40 GBq/mL (20 to 200 mCi/mL), of no carrier added 2-deoxy-2-[F 18] fluoro-D-glucose, at end of synthesis, in approximately 15 to 50 mL. The contents of each vial are sterile, pyrogen-free and preservative-free.

NDC 40028-511-30; 40028-511-50

Receipt, transfer, handling, possession, or use of this product is subject to the radioactive material regulations and licensing requirements of the U.S. Nuclear Regulatory Commission, Agreement States or Licensing States as appropriate.

Store the Fludeoxyglucose F 18 Injection vial upright in a lead shielded container at 25°C (77°F); excursions permitted to 15-30°C (59-86°F).

Store and dispose of Fludeoxyglucose F 18 Injection in accordance with the regulations and a general license, or its equivalent, of an Agreement State or a Licensing State.

The expiration date and time are provided on the container label. Use Fludeoxyglucose F 18 Injection within 12 hours from the EOS time.

### 17 PATIENT COUNSELING INFORMATION

Instruct patients in procedures that increase renal clearance of radioactivity. Encourage patients to:

- drink water or other fluids (as tolerated) in the 4 hours before their PET study.
- void as soon as the imaging study is completed and as often as possible thereafter for at least one hour.

Manufactured by: PETNET Solutions Inc.  
810 Innovation Drive  
Knoxville, TN 37932

Distributed by: PETNET Solutions Inc.  
810 Innovation Drive  
Knoxville, TN 37932

## PETNET Solutions

PN0002262 Rev. A  
March 1, 2011

# Clinical Multiparametric MR Imaging of Breast Tumors at 7 Tesla

Wolfgang Bogner<sup>1</sup>; Lenka Minarikova<sup>1</sup>; Katja Pinker<sup>2</sup>; Pascal Baltzer<sup>2</sup>; Olgica Zaric<sup>1,2</sup>; Marek Chmelik<sup>1</sup>; Stefan Zbýň<sup>1</sup>; Thomas Helbich<sup>2</sup>; Siegfried Trattnig<sup>1</sup>; Stephan Gruber<sup>1</sup>

<sup>1</sup>MR Center of Excellence (MRCE), Department of Biomedical Imaging and Image-Guided Therapy, Medical University Vienna, Austria

<sup>2</sup>Division of Molecular and Gender Imaging, Department of Biomedical Imaging and Image-Guided Therapy, Medical University Vienna, Austria

## Abstract

Magnetic Resonance Imaging (MRI) of the breast is a powerful imaging tool for the characterization, diagnosis, staging, and treatment monitoring of breast cancer. Applications at clinical magnetic field strengths ( $\leq 3T$ ) have been extensively described. At 7T\*, substantial improvements in image quality could be provided, if technical challenges can be overcome. In this article, the authors discuss the technical considerations and challenges, and present preliminary imaging examples obtained in patients on a 7T MAGNETOM MR scanner using dynamic contrast-enhanced MRI, diffusion-weighted MRI, and sodium MRI.

## Introduction

While only a few ultra-high field MR (7T) systems were installed ten years ago, between fifty and sixty 7T whole-body MR systems are currently available worldwide. The majority of these systems are dedicated primarily to

method development (sequence and hardware design). Only recently clinical studies have become possible. Body MRI, in particular, has been challenging at 7T.

At 7T, the increased signal-to-noise ratio (SNR) may provide images with higher spatial resolution and dynamic imaging with higher temporal resolution. Significant improvements have already been described in morphological MRI, diffusion-weighted imaging (DWI) and MR Spectroscopy (MRS) of the brain and in musculoskeletal imaging [1-4]. If technical challenges can be overcome, 7T has the potential to substantially improve multiparametric breast MRI. This would allow better detection of small and

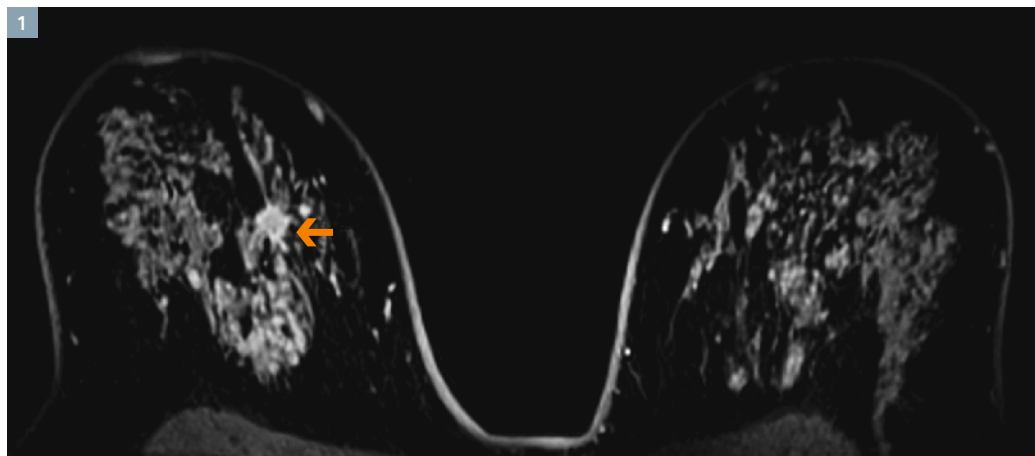
non-mass lesions that are challenging to identify with other existing clinical breast imaging modalities.

To give an overview this article provides initial clinical results of breast MRI performed at 7T, with special focus on dynamic contrast-enhanced (DCE) MRI, DWI, and sodium imaging. Results and images published in this article were acquired at the MRCE in Vienna, Austria.

## Dynamic contrast-enhanced imaging

Dynamic contrast-enhanced (DCE) MRI of the breast is an important clinical imaging tool for detection and characterization of breast lesions. By DCE-MRI, differentiation between benign and malignant contrast-enhanced breast cancer lesions is possible with an excellent diagnostic sensitivity close to 100% [5-10]. In early reports of clinical DCE-MRI performed at 1.5 or 3T a wide range of specificities were reported that ranged from 29% to 100% [8-10].

\*MAGNETOM 7T is ongoing research. All data shown are acquired using a non-commercial system under institutional review board permission. MAGNETOM 7T is still under development and not commercially available yet. Its future availability cannot be ensured.



**1** An example of bilateral DCE MRI obtained with  $0.7 \times 0.7 \times 0.7 \text{ mm}^3$  isotropic resolution at 7T of a 45-year-old breast cancer patient with malignant grade 2 invasive ductal carcinoma (arrow) with ring enhancement.

However, with appropriate techniques and experienced readers specificities not lower than 80% can be achieved at 1.5T or 3T [11, 12].

DCE-MRI provides both, morphologic assessment and enhancement characteristics of the lesions. On the one hand, using high spatial resolution enables the analysis of the morphological features of the lesions after contrast agent application and increases the sensitivity and specificity for detection of single and multiple breast lesions. On the other hand, high temporal resolution is advantageous for the analysis of contrast behavior during contrast agent uptake and wash-out phase [13]. Most malignant lesions show a strong contrast increase in the wash-in phase, followed by wash-out.

Due to limited SNR per time at field strengths  $\leq 3T$ , a trade-off between spatial and temporal resolution is necessary [14]. Kuhl et al. compared different temporal resolutions, suggesting that a higher spatial resolution is preferable, even at the expense of temporal resolution [14]. Other studies have demonstrated that an accurate assessment of both lesion morphology and enhancement kinetics is crucial for optimal diagnosis [11, 15-19]. Pinker and co-workers used a block design at 3T to acquire high spatial (pre- and post-contrast) and high temporal resolution (wash-in and post-contrast) to achieve high diagnostic accuracy [13].

Higher magnetic fields (i.e.,  $\geq 3T$ ) offer increased SNR that can be translated into higher spatial resolution [20].

Recently, several studies explored the increased SNR at 7T compared to 1.5T or 3T promising increased spatial and/or temporal resolution. In a preliminary study, Stehouwer et al. measured one patient with a mammographically suspicious breast mass (BI-RADS 5) at 3T and 7T using DCE-MRI with a unilateral breast coil [21]. They found a contrast-enhancement-to-noise ratio of 4.6 at 7T and 2.8 at 3T. Umutlu et al. reported high spatial resolution data from ten healthy subjects and five patients using a single-loop surface coil at 7T [22]. Van de Bank et al. reported ultra-high spatial and temporal resolution contrast-enhanced breast MR imaging using parallel imaging at 7T [23, 24]. A direct comparison of contrast-enhanced breast MRI between 3T and 7T showed excellent diagnostic accuracy at both field strengths in the same patients ( $n=24$ ), and comparable SNR when using a 3.2-fold higher spatial resolution at 7T, compared to 3T [25]. At 7T the authors used an isotropic spatial resolution of  $0.7 \times 0.7 \times 0.7 \text{ mm}^3$  combined with a temporal resolution of 14 s resulting in images without significant artifacts and satisfactory fat suppression (Fig. 1). This resulted in a sensitivity of 100% and a specificity of 92% demonstrating the high potential of breast-MRI at 7T [26]. Figure 2 shows a DCE MRI at 3T with lower resolution ( $1.4 \times 1.4 \times 1.4 \text{ mm}^3$ ) but similar SNR than in 7T with the resolution of  $0.7 \times 0.7 \times 0.7 \text{ mm}^3$  in the same patient with grade 3 invasive ductal carcinoma (IDC).

There are still several technical challenges of breast-MRI at 7T. The majority of authors found that the  $B_1$  field decreases toward the chest wall, which was observed and confirmed in their studies when performing (DCE-) breast MRI at 7T [27, 28]. Gruber et al. observed an SNR drop toward the chest at 7T of about 50% from the center of the breast. Measurements in the breast of healthy female subjects revealed that  $B_1^+$  dropped by 21% in the pre-pectoral region and 33% in the lateral region compared to the central region at 7T [27]. This may hamper the overall image quality, influence curve kinetics and hinder the diagnostic use of 7T MRI in those regions.

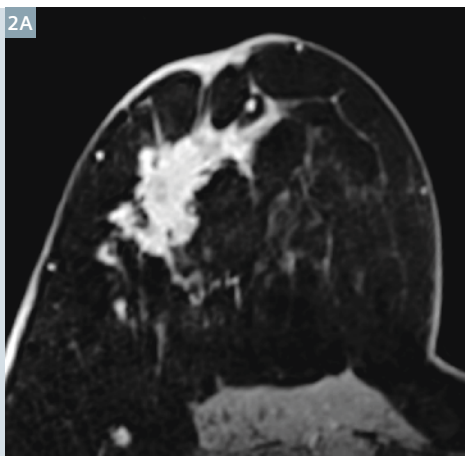
The use of T2-weighted sequences for breast MRI at 7T was not reported, because T2-weighted sequences based on turbo spin echo have significant  $B_1^+$  problems due to the use of multiple refocusing pulses. In addition, the use of multiple refocusing pulses and inversion recovery increases the specific absorption rate (SAR) requirements substantially and fat suppression is complicated. This was already a problem even at 3T. 3D T1-weighted sequences at 7T are limited to the use of low flip angles to minimize  $B_1^+$  inhomogeneities and SAR.

Promising results for DCE-MRI of the breast at 7T were shown by several groups, indicating that high spatial and temporal resolution are possible and result in high diagnostic accuracy. As soon as  $B_1$  inhomogeneities and

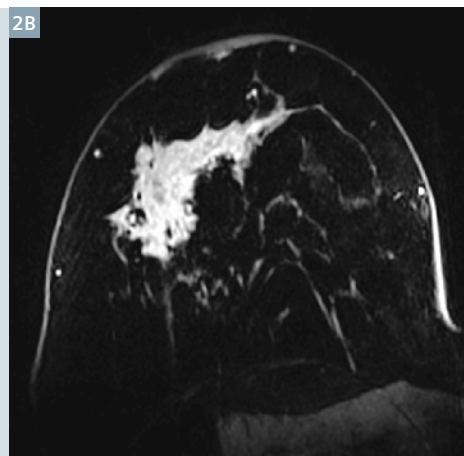
2

Comparison of DCE-MRI of a 63-year-old breast cancer patient. The pictures represent a malignant grade 3 invasive ductal carcinoma measured at 3T (2A) with spatial resolution of  $1.4 \times 1.4 \times 1.4 \text{ mm}^3$  isotropic and at 7T (2B) with spatial resolution of  $0.7 \times 0.7 \times 0.7 \text{ mm}^3$ .

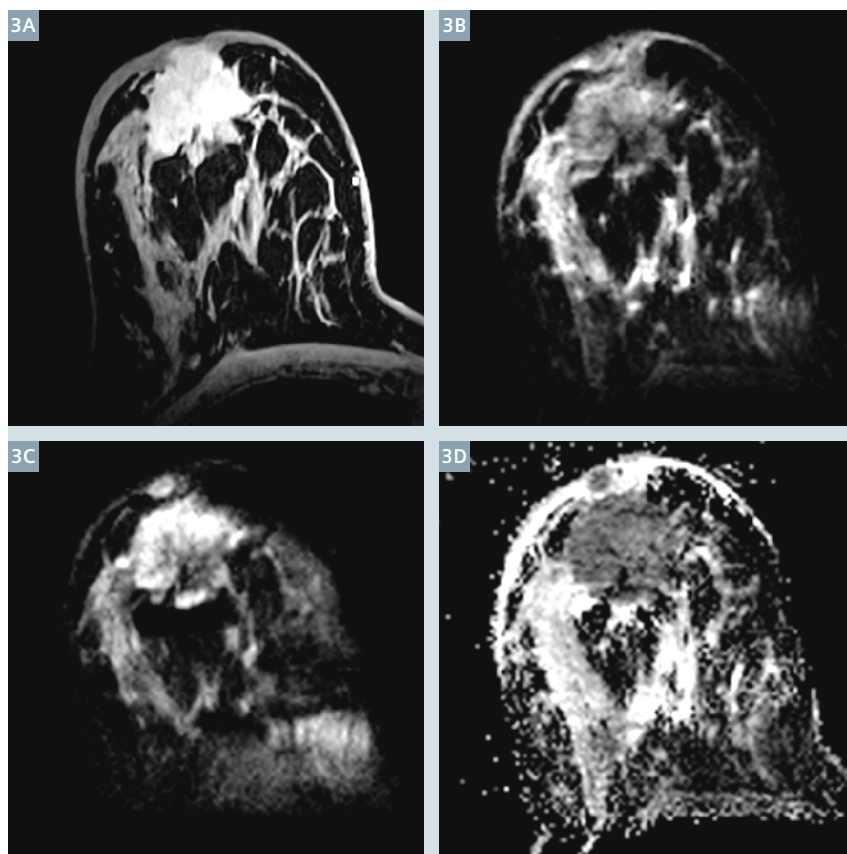
2A



2B







**3** A DWI example of a 36-year-old breast cancer patient with grade 3 invasive ductal carcinoma. The first image depicts the lesion on the contrast-enhanced T1-weighted image (3A). Following are the DWI images: (3B)  $b = 0 \text{ s/mm}^2$ , (3C)  $b = 850 \text{ s/mm}^2$  and (3D) the ADC map.

excessive local SAR are mitigated by improved coil design (pTX technology and  $B_1^+$  shimming) and sequence techniques the potential of breast MRI at 7T can be fully explored. This will allow to measure breast lesions that are more difficult to diagnose at lower field strengths (e.g., small lesions, non-mass-like enhancing lesions, ductal carcinoma in situ).

### Diffusion-weighted imaging

Diffusion-weighted imaging (DWI) is the most promising adjunct MRI method to improve the diagnostic specificity of the established DCE-MRI examinations of the breast [29, 30].

By assessing the apparent diffusion coefficient (ADC) of water molecules, DWI probes tissue microstructure on a cellular level. Low ADC values in breast tissue reflect the higher cellular

density that is present in malignant lesions [30]. Therefore, DWI has a high potential for characterizing breast tumors and monitoring/predicting treatment response [31].

However, DWI suffers from lower spatial resolution than DCE-MRI. For adequate morphologic assessment of breast lesions, the EUSOMA working group recommends to use spatial resolutions not below  $1 \times 1 \times 2.5 \text{ mm}^3$  for CE-MRI [32]. If this degree of anatomical detail can be also reached by DWI sequences, it may allow, both, the detection of smaller lesions and the morphological evaluation of breast DWI beyond simple ADC measures. This prospect of combining molecular and morphologic information has driven the urge to improve imaging techniques, hardware, and measure at higher static magnetic field strength.

While there is some initial clinical experience published on DCE-MRI of the breast at 7T [26, 27, 33], reported experience on breast DWI at 7T is scarce. Promising, but preliminary unilateral breast DWI results of three patients [34] and a volunteer [35] have so far been shown at 7T, but larger patients studies have not been reported. Yet, an up to 5.7-fold SNR increase compared to 3T indicates the available potential, but the spatial resolution and image quality were hampered by the use of single-shot echo planar imaging (ss-EPI), fat suppression failure, and motion artifacts [34].

Routine breast DWI at  $\leq 3\text{T}$  is based on ss-EPI, but ss-EPI is known to be prone to image artifacts (i.e., geometric distortions,  $T_2^*$  image blurring, ghosting artifacts, and insufficient fat suppression) and these artifacts become stronger at 7T [36-39]. Strong  $T_2^*$  image blurring, in particular, prevents the anticipated increase in spatial resolution at 7T.

Recent sequence developments for DWI of the brain at 7T, have conclusively illustrated that most of these artifacts can be effectively overcome even at ultra-high magnetic field strength, when using a novel 2D-navigator-corrected readout-segmented EPI sequence known as RESOLVE (REadout Segmentation Of Long Variable Echo trains) in combination with GRAPPA (GeneRalized Autocalibrating Partially Parallel Acquisitions) [40]. Our initial experiences show that this sequence can also significantly improve the image quality of breast DWI at 7T (Fig. 3). A combination of RESOLVE and GRAPPA may overcome former restrictions in spatial resolution by providing high-quality DWI with sub-millimeter in-plane resolution (FOV  $320 \times 160 \text{ mm}^2$ , matrix  $340 \times 170$ ,  $0.9 \times 0.9 \times 5 \text{ mm}^3$ ) for characterization of breast lesions in only 3:35 min. Our data show that this combination allows for clinical breast DWI protocols that reduce the amount of artifacts by a factor of 7 and significantly improve the apparent spatial resolution compared to regular ss-EPI sequences (Fig. 4).

One additional aspect that we observed in our data, is the fact that acquired RESOLVE images without diffusion weighting (i.e.,  $b=0$  s/mm<sup>2</sup>) had already very similar spatial resolution and contrast as regular STIR. This raises the question whether such RESOLVE-based T2-weighted images could not possibly replace additionally acquired STIR images soon. This would make the additional acquisition of STIR obsolete and save valuable measurement time.

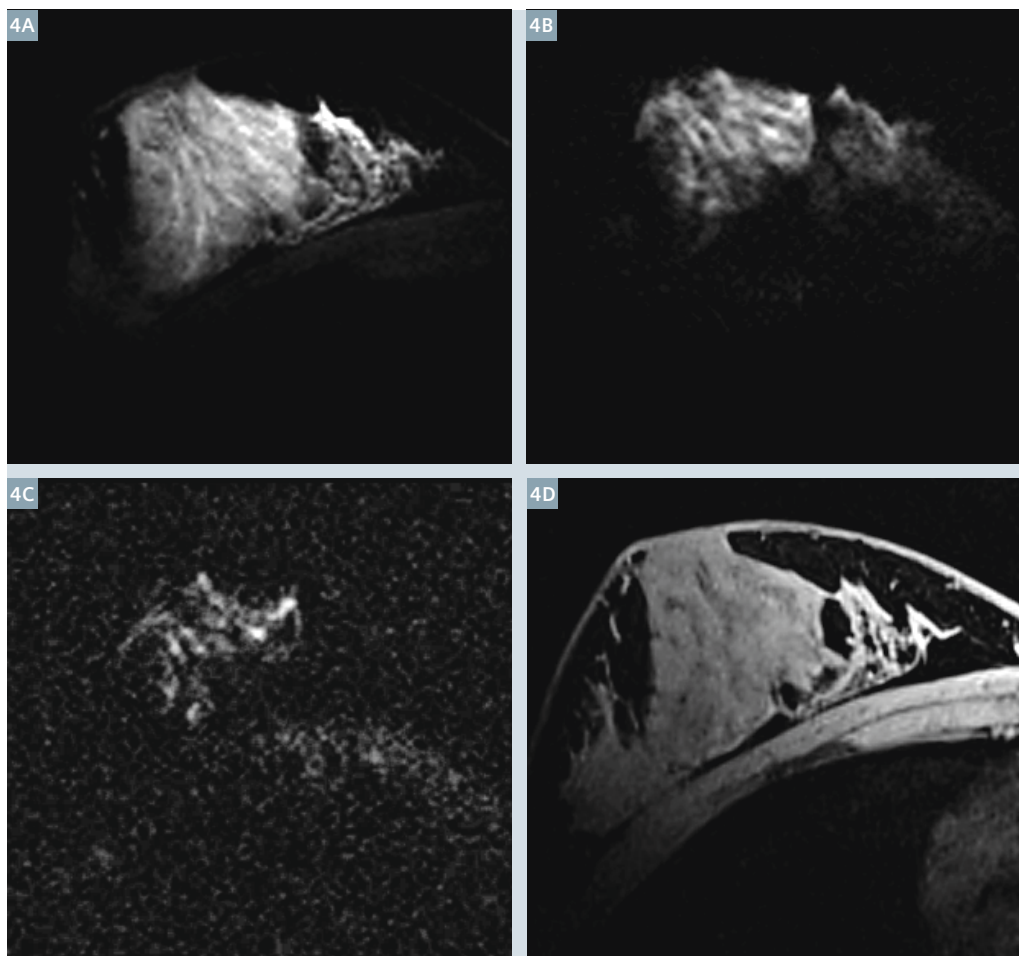
With spatial resolutions of DWI reaching those recommended for DCE-MRI of the breast [41, 42], future DWI evaluation may not anymore be limited to ADC quantification alone, but could allow the additional assessment of morphologic features, which is a cornerstone of current DCE-MRI evaluation. This new aspect of DWI could further improve the specificity of breast MRI and should be the subject of future investigations.

Our preliminary data are still far from what could be possible at 7T. Currently, our image quality improvements were predominantly achieved via sequence improvements. However, our hardware was limited. We used a dual tuned four-<sup>1</sup>H-channel receive breast coil (Stark, Erlangen, Germany) that provided reasonably good  $B_1$  homogeneity, but can be easily outperformed with respect to SNR by modern multi-array coil design with  $\geq 16$  channels, and which would in combination with multi transmit technology, mitigate  $B_1$  errors to reduce sensitivity dropouts e.g. near the axilla. Stronger diffusion gradients than used for our preliminary study (max gradient strength, 45 mT/m; slew rate, 150 T/m/s) will further shorten TE and substantially improve the SNR of DWI, in particular since T2 decay in breast parenchyma is twice as fast as in brain tissue [43]. Partial Fourier reconstruction could

further shorten the TE or scan time of RESOLVE [44]. Further improvements in hardware and software may, therefore, double or even triple the SNR obtained in our preliminary study, paving the way for further improvements in spatial resolution.

## Sodium imaging

Proliferating cells have an abnormally high sodium content, because the normally very low intracellular sodium concentration of about 10–15 mmol/l is elevated several fold as a result of altered  $\text{Na}^+/\text{H}^+$  transport kinetics and pH [45]. Outside the cells continuous perfusion of living tissue will ensure a constant sodium concentration of ~140 mmol/l. Thus, an increase in the extracellular volume fraction through the increased vascularization (angiogenesis) and the increased interstitial space in tumors will also lead to an increase in tissue sodium concentration (TSC) in tumors. While the total



4

Sample DWI images with  $b=0$  s/mm<sup>2</sup> of a 23-year-old female volunteer were obtained for **(4A)** rsEPI with GRAPPA factor 2; **(4B)** ssEPI with GRAPPA factor 2; **(4C)** ssEPI without parallel imaging, compared to a T1-weighted reference image obtained with  $0.7 \times 0.7 \times 0.7$  mm isotropic resolution **(4D)**. Although all DWI sequences were adjusted to the same spatial resolution (i.e.,  $0.9 \times 0.9$  mm in-plane), rsEPI with GRAPPA showed significantly less T2\* blurring **(4A)** than both versions of ssEPI **(4A, B)**, as well as lower distortion. (Reproduced with permission from Bogner, Radiology, 2014)

TSC (extracellular and intracellular) is known to be a good measure of altered cell metabolism [46-49], it is expected that the quantification of only intracellular sodium concentration (IC-TSC) is an even more specific marker of pathology, since changes in IC-TSC are more pronounced than changes in total TSC [50].

The unique sensitivity of  $^{23}\text{Na}$ -MRI to both extra-cellular volume and intracellular changes related to cell proliferation can provide information that is supplemental to high resolution CE-MRI.

While  $^{23}\text{Na}$ -MRI is interesting for characterization, it is expected that it could play a much bigger role in treatment prediction/monitoring. Lack of substrate and oxygen can cause very significant changes in TSC. As soon as the energy dependent  $\text{Na}^+/\text{K}^+$ -ATPase stops pumping sodium out of the

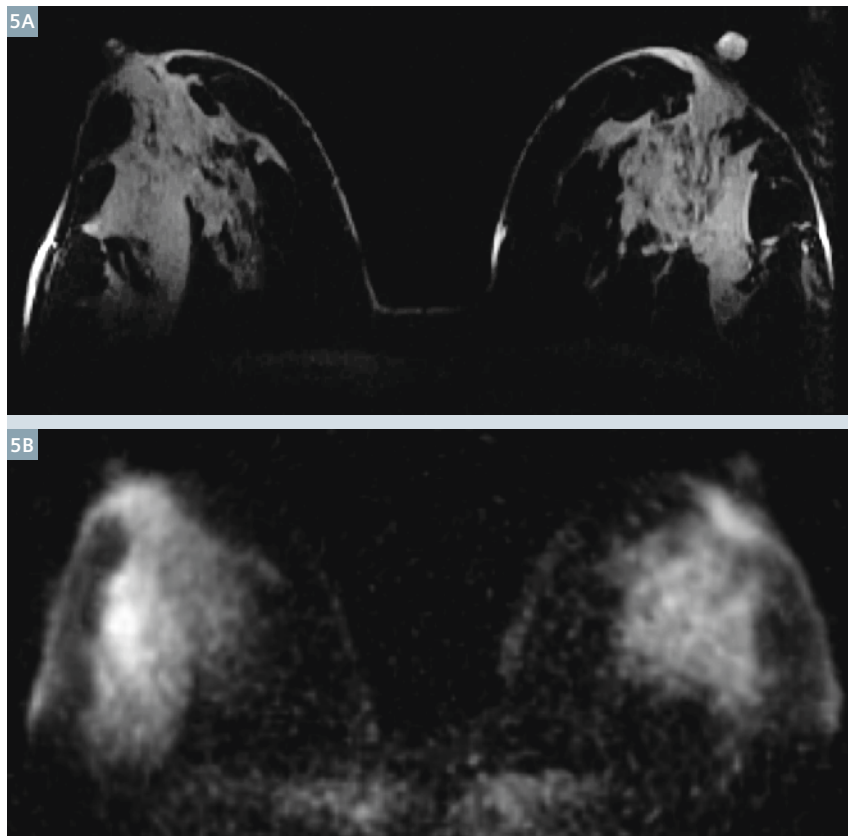
cell, passive sodium influx from the extracellular environment will rapidly raise the intracellular levels of sodium several fold. This effect is exacerbated if a stress on the cells increases the permeability of the cell wall for sodium ions. It was also shown recently that  $\text{Na}^+/\text{K}^+$ -ATPase is a critical factor in multi drug resistance of cancer cells [51, 52].  $\text{Na}^+/\text{K}^+$ -ATPase is thus an important target in drug development for cancer treatment. Also in treatment monitoring the discrimination of IC-TSC and EC-TSC may potentially improve the possibility to observe even small changes in IC-TSC.

The acute effect of a therapy that causes cell death on an appreciable scale should therefore be easy to monitor with  $^{23}\text{Na}$ -MRI. Several animal studies found significantly increased TSC a few days after therapy [48, 49]. Only one treatment

response study extracted information on both IC-TSC and EC-TSC one day after treatment [50]. Long-term effects of such therapies remain to be investigated. In a limited number of breast cancer patients that underwent pre-operative adjuvant therapy the effect of the therapy in responders showed an increase in the tumor TSC along with a decline in lesion size as reported recently [53].

While  $^{23}\text{Na}$  with reasonably good spatial resolution was not possible at  $\leq 3\text{T}$ , we can show that at 7T breast  $^{23}\text{Na}$  MRI can reach spatial resolutions that are already similar to that of DWI at lower field strengths. With a bilateral dual tuned  $^1\text{H}/^{23}\text{Na}$  phased array breast coil (i.e., 16- $^{23}\text{Na}$  receive-channels) in combination with a highly sensitive ultra-short echo-time sequence, AWSOS (Acquisition Weighted Stack Of Spirals) [54] were able to acquire high resolution  $^{23}\text{Na}$  images in both healthy volunteers and patients with high in-plane spatial resolution of  $1.5 \times 1.5 \text{ mm}^2$  (FOV  $320 \times 320 \text{ mm}^3$ , matrix  $208 \times 208$ ,  $1.5 \times 1.5 \times 5 \text{ mm}^3$ ) in a reasonable scan time of 16:19 min.

Our preliminary results show that even the low  $^{23}\text{Na}$  content in healthy glandular breast tissue can be well imaged using advanced imaging techniques/hardware at 7T (Fig. 5). Due to the low gyromagnetic ratio of  $^{23}\text{Na}$  compared to  $^1\text{H}$  nuclei, there are no significant problems related to expected  $B_1$  inhomogeneities, however the very short relaxation times are challenging for the design of sensitive MR sequences. It can be expected that the significantly higher  $^{23}\text{Na}$  content in malignant breast lesions can be imaged with further improved spatial resolution. Satisfactory image resolution, SNR and reasonable imaging time, enable this technique to be potentially implemented in routine MRI protocols. However, future sequence development will have to target a more specific quantification of IC-TSC concentration [55]. With such IC-TSC sensitive methods in hand,  $^{23}\text{Na}$  could become a powerful imaging tool for characterization of breast tumors and particularly assessment of treatment status,



**5** An example of sodium imaging of a healthy subject. (5A) Is a localized  $^1\text{H}$  image and (5B) a sodium image with the resolution of  $1.5 \times 1.5 \times 5 \text{ mm}^3$ .



since changes in IC-TSC are known to appear even far before they can be depicted by other modern MRI techniques such as DCE-MRI, DWI, MR spectroscopy. In combination with other  $^1\text{H}$  MRI techniques  $^{23}\text{Na}$  imaging may, thus, become an attractive tool for the investigations of breast tumors with a particular focus on the early treatment prediction and monitoring.

## Conclusion

Although in the near future, MRI of the breast at 7T will remain technically challenging, our recent patient results show already significant image quality improvements with a high potential for clinical application.

With the additional use of the most recent hardware (stronger gradients, parallel transmit technology, improved coil design) and further improved MR sequences, we will soon be able to

fully exploit the imaging potential of 7T MRI even for the assessment of breast cancer. 7T MRI of the breast will simultaneously provide high temporal and spatial resolution DCE-MRI, allow increased spatial resolution of DWI that can compete with that of CE-MRI at lower field strength, and even make additional imaging contrasts such as  $^{23}\text{Na}$  imaging available that were impossible to perform in the past. While this will likely not change routine breast cancer diagnosis, it remains to be shown, what impact multi-parametric MRI of the breast at 7T can have in the fine-tuning of expensive, but life-saving neoadjuvant treatments.



## Contact

Siegfried Trattnig, M.D.  
Medical University of Vienna  
Department of Biomedical  
Imaging and Image-guided  
Therapy  
MRCE  
Lazarettgasse 14,  
1090 Vienna, Austria  
siegfried.trattnig@akhwien.at

## Further Information

Visit [www.siemens.com/7t-meduni](http://www.siemens.com/7t-meduni) where Professor Trattnig presents some impressive findings in the fields of Neuro-, Orthopedic- and Body MR imaging.

### References

- Moser E, Stahlberg F, Ladd ME, Trattnig S. 7-T MR--from research to clinical applications? *NMR Biomed*. 2012;25(5):695-716.
- Trattnig S, Zbyn S, Schmitt B, et al. Advanced MR methods at ultra-high field (7 Tesla) for clinical musculoskeletal applications. *Eur Radiol*. 2012;22(11):2338-46.
- Heidemann RM, Porter DA, Anwender A, et al. Diffusion imaging in humans at 7T using readout-segmented EPI and GRAPPA. *Magn Reson Med*. 2010;64(1):9-14.
- Bogner W, Gruber S, Trattnig S, Chmelik M. High-resolution mapping of human brain metabolites by free induction decay ( $^1\text{H}$ ) MRSI at 7 T. *NMR Biomed*. 2012;25(6):873-82.
- Boetes C, Veltman J, van Die L, et al. The role of MRI in invasive lobular carcinoma. *Breast Cancer Res Treat*. 2004;86(1):31-7.
- Kinkel K, Helbich TH, Esserman LJ, et al. Dynamic high-spatial-resolution MR imaging of suspicious breast lesions: diagnostic criteria and interobserver variability. *AJR Am J Roentgenol*. 2000;175(1):35-43.
- Schnall MD, Blume J, Bluemke DA, et al. Diagnostic architectural and dynamic features at breast MR imaging: multicenter study. *Radiology*. 2006;238(1):42-53.
- Davis PL, McCarty KS, Jr. Sensitivity of enhanced MRI for the detection of breast cancer: new, multicentric, residual, and recurrent. *Eur Radiol*. 1997;7 Suppl 5:289-98.
- Orel SG, Schnall MD. MR imaging of the breast for the detection, diagnosis, and staging of breast cancer. *Radiology*. 2001;220(1):13-30.
- Heywang-Kobrunner SH, Viehweg P, Heinig A, Kuchler C. Contrast-enhanced MRI of the breast: accuracy, value, controversies, solutions. *Eur J Radiol*. 1997;24(2):94-108.
- Kuhl C. The current status of breast MR imaging. Part I. Choice of technique, image interpretation, diagnostic accuracy, and transfer to clinical practice. *Radiology*. 2007;244(2):356-78.
- Benndorf M, Baltzer PA, Vag T, et al. Breast MRI as an adjunct to mammography: Does it really suffer from low specificity? A retrospective analysis stratified by mammographic BI-RADS classes. *Acta Radiol*. 2010;51(7):715-21.
- Pinker K, Grabner G, Bogner W, et al. A combined high temporal and high spatial resolution 3 Tesla MR imaging protocol for the assessment of breast lesions: initial results. *Invest Radiol*. 2009;44(9):553-8.
- Kuhl CK, Schild HH, Morakkabati N. Dynamic bilateral contrast-enhanced MR imaging of the breast: trade-off between spatial and temporal resolution. *Radiology*. 2005;236(3):789-800.
- Helbich TH. Contrast-enhanced magnetic resonance imaging of the breast. *Eur J Radiol*. 2000;34(3):208-19.
- Kinkel K, Helbich TH, Esserman LJ, et al. Dynamic high-spatial-resolution MR imaging of suspicious breast lesions: Diagnostic criteria and interobserver variability. *American Journal of Roentgenology*. 2000;175(1):35-43.
- Kuhl CK. Current status of breast MR imaging. Part 2. Clinical applications. *Radiology*. 2007;244(3):672-91.
- Lieberman L, Morris EA, Lee MJ, et al. Breast lesions detected on MR imaging: features and positive predictive value. *AJR Am J Roentgenol*. 2002;179(1):171-8.
- Helbich TH, Roberts TP, Gossman A, et al. Quantitative gadopentetate-enhanced MRI of breast tumors: testing of different analytic methods. *Magn Reson Med*. 2000;44(6):915-24.
- Ladd ME. High-field-strength magnetic resonance: potential and limits. *Top Magn Reson Imaging*. 2007;18(2):139-52.
- Stehouwer BL, Klomp DW, Korteweg MA, et al. 7T versus 3T contrast-enhanced breast magnetic resonance imaging of invasive ductal/lobular carcinoma: first clinical experience. *Magn Reson Imaging*. 2013;31(4):613-7.
- Umutlu L, Maderwald S, Kraff O, et al. Dynamic contrast-enhanced breast MRI at 7 Tesla utilizing a single-loop coil: a feasibility trial. *Acad Radiol*. 2010;17(8):1050-6.
- van de Bank BL, Voogt IJ, Italiaander M, et al. Ultra high spatial and temporal resolution breast imaging at 7T. *NMR Biomed*. 2012.
- Kuroki Y, Nasu K, Kuroki S, et al. Diffusion-weighted imaging of breast cancer with the sensitivity encoding technique: analysis of the apparent diffusion coefficient value. *Magn Reson Med Sci*. 2004;3(2):79-85.

- 25 Gruber S, Pinker K, Zaric O, et al. Dynamic contrast-enhanced magnetic resonance imaging of breast tumors at 3 and 7T: a comparison. *Investigative radiology*. 2014;49(5):354-62.
- 26 Pinker K, Bogner W, Baltzer P, et al. Clinical application of bilateral high temporal and spatial resolution dynamic contrast-enhanced magnetic resonance imaging of the breast at 7T. *Eur Radiol*. 2014; 24(4):913-20.
- 27 Gruber S, Pinker K, Zaric O, et al. Dynamic contrast-enhanced magnetic resonance imaging of breast tumors at 3 and 7T: a comparison. *Invest Radiol*. 2014;49(5): 354-62.
- 28 Stehouwer BL, Klomp DW, Korteweg MA, et al. 7T versus 3T contrast-enhanced breast Magnetic Resonance Imaging of invasive ductal lobular carcinoma: First clinical experience. *Magn Reson Imaging*. 2013;31(4):613-7.
- 29 Pinker K, Stadlbauer A, Bogner W, et al. Molecular imaging of cancer: MR spectroscopy and beyond. *Eur J Radiol*. 2012;81(3):566-77.
- 30 Bogner W, Gruber S, Pinker K, et al. Diffusion-weighted MR for differentiation of breast lesions at 3.0 T: how does selection of diffusion protocols affect diagnosis? *Radiology*. 2009;253(2): 341-51.
- 31 Pickles MD, Gibbs P, Lowry M, Turnbull LW. Diffusion changes precede size reduction in neoadjuvant treatment of breast cancer. *Magn Reson Imaging*. 2006; 24(7):843-7.
- 32 Sardanelli F, Boetes C, Borisch B, et al. Magnetic resonance imaging of the breast: recommendations from the EUSOMA working group. *Eur J Cancer*. 2010;46(8):1296-316.
- 33 Korteweg MA, Veldhuis WB, Visser F, et al. Feasibility of 7 Tesla breast magnetic resonance imaging determination of intrinsic sensitivity and high-resolution magnetic resonance imaging, diffusion-weighted imaging, and (1)H-magnetic resonance spectroscopy of breast cancer patients receiving neoadjuvant therapy. *Invest Radiol*. 2011;46(6):370-6.
- 34 Korteweg MA, Veldhuis WB, Visser F, et al. Feasibility of 7 Tesla Breast Magnetic Resonance Imaging Determination of Intrinsic Sensitivity and High-Resolution Magnetic Resonance Imaging, Diffusion-Weighted Imaging, and (1)H-Magnetic Resonance Spectroscopy of Breast Cancer Patients Receiving Neoadjuvant Therapy. *Investigative Radiology*. 2011;46(6): 370-6.
- 35 Wiesinger F, Van de Moortele PF, Adriany G, et al. Parallel imaging performance as a function of field strength—an experimental investigation using electrodynamic scaling. *Magn Reson Med*. 2004;52(5): 953-64.
- 36 Baltzer PAT, Renz DM, Herrmann KH, et al. Diffusion-weighted imaging (DWI) in MR mammography (MRM): clinical comparison of echo planar imaging (EPI) and half-Fourier single-shot turbo spin echo (HASTE) diffusion techniques. *European Radiology*. 2009;19(7):1612-20.
- 37 Bogner W, Pinker-Domenig K, Bickel H, et al. Readout-segmented Echo-planar Imaging Improves the Diagnostic Performance of Diffusion-weighted MR Breast Examinations at 3.0 T. *Radiology*. 2012;263(1): 64-76.
- 38 Holdsworth SJ, Skare S, Newbould RD, Bammer R. Robust GRAPPA-accelerated diffusion-weighted readout-segmented (RS)-EPI. *Magnetic Resonance in Medicine*. 2009;62(6):1629-40.
- 39 Porter DA, Heidemann RM. High resolution diffusion-weighted imaging using readout-segmented echo-planar imaging, parallel imaging and a two-dimensional navigator-based reacquisition. *Magnetic Resonance in Medicine*. 2009;62(2):468-75.
- 40 Porter DA, Heidemann RM. High resolution diffusion-weighted imaging using readout-segmented echo-planar imaging, parallel imaging and a two-dimensional navigator-based reacquisition. *Magn Reson Med*. 2009;62(2):468-75.
- 41 Muller M, Kuhl FC, Grossmann P, et al. Emission properties of ns and ps laser-induced soft x-ray sources using pulsed gas jets. *Opt Express*. 2013;21(10): 12831-42.
- 42 Sardanelli F, Boetes C, Borisch B, et al. Magnetic resonance imaging of the breast: Recommendations from the EUSOMA working group. *European Journal of Cancer*. 2010;46(8):1296-316.
- 43 Rakow-Penner R, Daniel B, Yu HZ, et al. Relaxation times of breast tissue at 1.5T and 3T measured using IDEAL. *Journal of Magnetic Resonance Imaging*. 2006; 23(1):87-91.
- 44 Frost R, Porter DA, Miller KL, Jezzard P. Implementation and assessment of diffusion-weighted partial Fourier readout-segmented echo-planar imaging. *Magn Reson Med*. 2012;68(2):441-51.
- 45 Reshkin SJ, Bellizzi A, Caldeira S, et al. Na<sup>+</sup>/H<sup>+</sup> exchanger-dependent intracellular alkalization is an early event in malignant transformation and plays an essential role in the development of subsequent transformation-associated phenotypes. *Faseb Journal*. 2000;14(14):2185-97.
- 46 Ouwerkerk R, Bleich KB, Gillen JS, et al. Tissue sodium concentration in human brain tumors as measured with Na-23 MR imaging. *Radiology*. 2003;227(2):529-37.
- 47 Ouwerkerk R, Jacobs MA, Macura KJ, et al. Elevated tissue sodium concentration in malignant breast lesions detected with non-invasive Na-23 MRI. *Breast Cancer Research and Treatment*. 2007;106(2):151-60.
- 48 Schepkin VD, Lee KC, Kuszpit K, et al. Proton and sodium MRI assessment of emerging tumor chemotherapeutic resistance. *Nmr in Biomedicine*. 2006;19(8):1035-42.
- 49 Schepkin VD, Ross BD, Chenevert TL, et al. Sodium magnetic resonance imaging of chemotherapeutic response in a rat glioma. *Magnetic Resonance in Medicine*. 2005; 53(1):85-92.
- 50 Sharma R, Wu EX, Kline R, et al. Rapid in vivo monitoring of methyl-nitroso-urea (MNU) induced breast tumor response to Taxotere in rats using intracellular sodium 4.2 Tesla magnetic resonance imaging and immunohistological characterization. *Clinical Cancer Research*. 2001;7(11):3699s.
- 51 Mijatovic T, Jungwirth U, Heffeter P, et al. The Na<sup>+</sup>/K<sup>+</sup>-ATPase is the Achilles Heel of multi-drug-resistant cancer cells. *Cancer Letters*. 2009;282(1):30-4.
- 52 Mijatovic T, Ingrassia L, Facchini V, Kiss R. Na<sup>+</sup>/K<sup>+</sup>-ATPase alpha subunits as new targets in anticancer therapy. *Expert Opinion on Therapeutic Targets*. 2008; 12(11):1403-17.
- 53 Jacobs MA, Ouwerkerk R, Wolff AC, et al. Monitoring primary systemic therapy in locally advanced breast cancer using proton and sodium magnetic resonance imaging. In: *Proceedings of the twelfth meeting of the international society of magnetic resonance in medicine*. ISMRM, Dec 2004. Kyoto, Japan.
- 54 Qian Y, Zhao T, Hue YK, et al. High-resolution spiral imaging on a whole-body 7T scanner with minimized image blurring. *Magn Reson Med*. 2010;63(3):543-52.
- 55 Nagel AM, Amarteifio E, Lehmann-Horn F, et al. 3 Tesla sodium inversion recovery magnetic resonance imaging allows for improved visualization of intracellular sodium content changes in muscular channelopathies. *Invest Radiol*. 2011; 46(12): 759-66.

# Get your free copy of the PI-RADS Scoring Image Atlas

Visit us at [www.siemens.com/magnetom-world](http://www.siemens.com/magnetom-world)  
Go to > Publications > Subscriptions > MRI Poster

## PI-RADS Classification: Structured Reporting for MRI of the Prostate

M. Rothke, D. Blondin, H.-P. Schlemmer, T. Fritzel

Department of Radiology, Heinrich Heine University (2007), Düsseldorf, Germany  
Department of Radiology, Heinrich Heine University (2007), Düsseldorf, Germany  
Department of Radiology, Heinrich Heine University (2007), Düsseldorf, Germany

### Introduction

Prostate MRI has become an increasingly relevant adjunctive modality in the detection of prostate cancer. In Germany, it is mostly used in patients with prior negative biopsy and/or elevated PSA levels. The PI-RADS classification is a structured reporting scheme for prostate MRI. It is based on a 5-point scale with scores ranging from 1 to 5. However, it lacks information on the individual imaging findings and their clinical use as well as uniform instructions for appropriate reporting of the individual radiological findings. This makes use of the PI-RADS classification in daily practice difficult, especially for radiologists who are not familiar with prostate MRI. It is therefore the aim of this paper to present the PI-RADS classification for the detection of prostate cancer using representative images for the relevant scores and to add scoring criteria that can be used in daily practice. The PI-RADS score was also determined by consensus. The individual imaging reports were checked and evaluated with reference to current literature. The scoring criteria for the PI-RADS classification are presented in a schematic chart that allows the findings to be taken into account in the consensus report. The individual imaging reports are described and critically assessed in terms of their advantages and disadvantages.

**Materials and methods**  
The fundamentals of technical imaging parameters were described by consensus. The sample images were selected by the authors to correspond to the basis of representative image findings from the 4 categories. The PI-RADS score was also determined by consensus. The individual imaging reports were checked and evaluated with reference to current literature. The scoring criteria for the PI-RADS classification are presented in a schematic chart that allows the findings to be taken into account in the consensus report. The individual imaging reports are described and critically assessed in terms of their advantages and disadvantages.

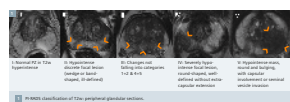
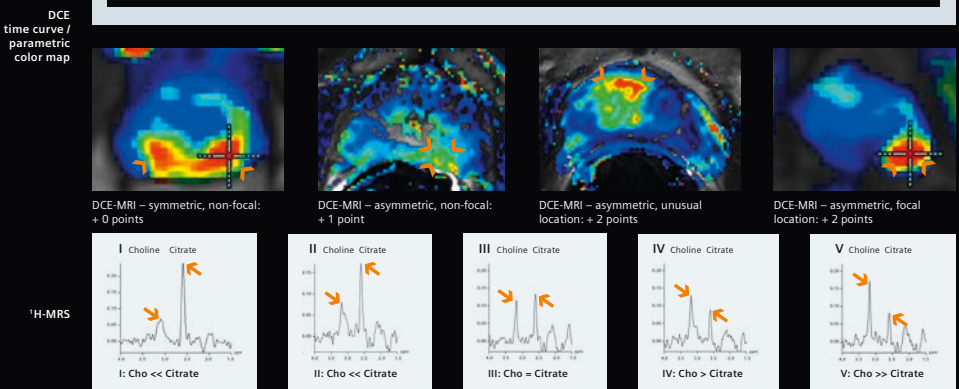
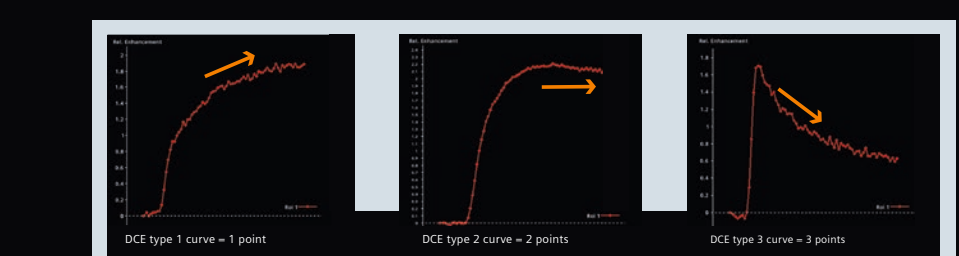
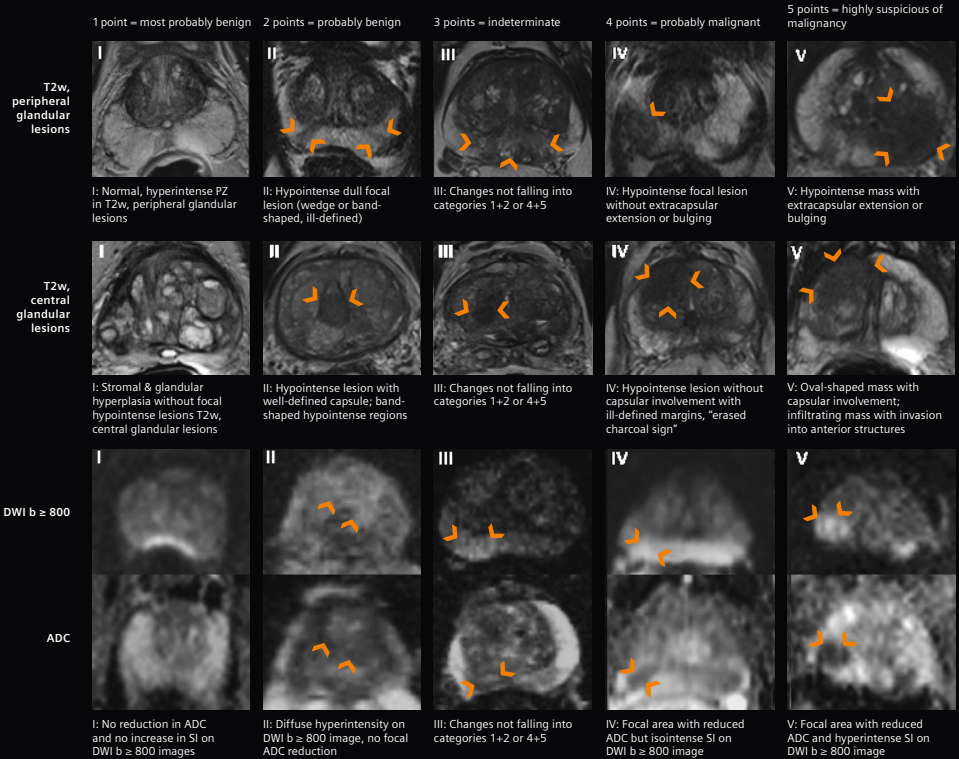


Fig. 1: PI-RADS classification of the peripheral prostate region.



For details please refer to: M. Rothke, D. Blondin, H.-P. Schlemmer, T. Fritzel: "PI-RADS Classification: Structured Reporting for MRI of the Prostate", MAGNETOM Flash issue 4/2013, ASTRO edition, page 30-38.

Read the comprehensive article

## "PI-RADS Classification: Structured Reporting for MRI of the Prostate"

by Matthias Röthke et al.  
in MAGNETOM Flash 4/2013  
page 30-38.

Available for download at [www.siemens.com/magnetom-world](http://www.siemens.com/magnetom-world)

[www.siemens.com/magnetom-world](http://www.siemens.com/magnetom-world)

# PI-RADS SCORING Image Atlas Prostate MRI



# Can an Automated Decision Tree Based on Quantitative DCE-MRI Help to Accurately Classify Complex Adnexal Masses?

Anahita Fathi Kazerooni; Mahnaz Nabil; Hamidreza Saligheh Rad

Quantitative MR Imaging and Spectroscopy Group, Research Center for Molecular and Cellular Imaging, Tehran University of Medical Sciences, Iran

Department of Medical Physics and Biomedical Engineering, School of Medicine, Tehran University of Medical Sciences, Iran

## Introduction

Ovarian cancer is recognized to be a genetically heterogeneous disease with a poor prognosis, and the leading cause of death in women from gynecological cancers [1]. It has been called the "silent killer", due to its non-specific symptoms and absence of effective screening tools, which delays the diagnosis until it is well advanced [2]. Overall 5-year survival is about 50%, which could be improved drastically to 90%, if diagnosed at an early stage [3]. In this light, an adequate screening tool, that allows for sensitive and specific detection at early stages, could highly impact patient survival.

Several diagnostic imaging techniques have been investigated for their potential screening and diagnostic capability. Ultrasonography (US) is the first-line examination method of choice for discovering ovarian masses, due to its wide availability, low costs, and high sensitivity in detecting abnormal masses [4]. Nevertheless, there exist some overlap in US features extracted for benign or malignant ovarian masses and about 10 to 20% of ovarian masses remain indeterminate on US, which are mostly benign lesions. This could be either because their origin (ovary, uterus or other pelvic structures) is difficult to determine on US exam, or they manifest with complex structure (having both solid and cystic components) [5].

Accurate decision making about the type and extent of indeterminate complex ovarian mass could significantly

affect patient outcome: While unnecessary and extensive operation could be avoided in patients with benign masses, increased survival rate could be offered to patients with malignant masses by accurate staging and radical resection [5, 6].

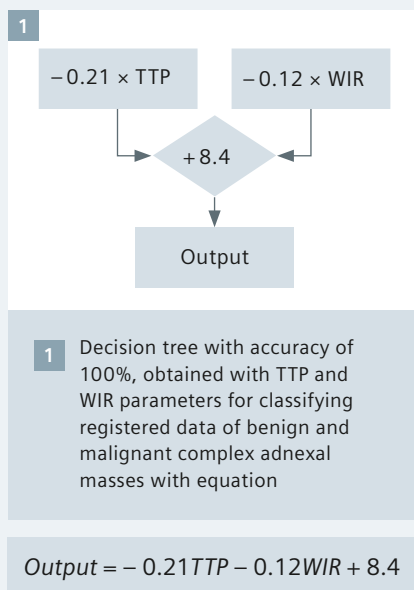
Magnetic resonance imaging (MRI) offers significantly higher specificity over US (84-92% for MRI [7-9] vs. 50% for US [10]) for characterizing indeterminate complex adnexal masses, as it provides superb spatial resolution and tissue contrast [7, 10, 11]. Yet, approximately 10% of indeterminate complex ovarian masses are "overcalled" by conventional MRI: Some benign tumors appear with visible enhancement, which are usually interpreted as malignant lesions [6, 12]. Besides, the interpretation of the images is qualitative; hence it is subjective and dependent on the experience of the radiologist [7].

Dynamic contrast-enhanced (DCE-) MRI has evolved into a helpful predictive and prognostic imaging technique in distinguishing benign from malignant complex adnexal masses [13, 14]. In this setting, semi-quantitative parameters extracted from contrast enhancement curves have shown to provide noninvasive and quantitative biomarkers of tumor progression [15]. Improved imaging accuracy, achieved through sensitive and specific quantitative biomarkers of ovarian tumor malignancy by DCE-MRI, could lead to the development of efficient diagnosis and

screening tools, increase the probability of early diagnosis, and consequently improve patient outcome.

Reliable prediction of malignancy in complex adnexal masses depends on proper selection of quantitative DCE-MRI descriptive parameters and their cutoff points. The selection of cutoff points is commonly carried out by threshold criteria [14, 16], and is dependent on the imaging protocol and the MRI scanner. However, whilst one of the major assumptions in quantification of DCE-MR images in abdominal organs, such as the ovary, is spatially fixed region-of-interest over the time course of contrast agent passage, this assumption becomes essentially invalid when motion artifacts occur. Thus, accurate quantification of DCE-MRI image series depends greatly on minimization of motion artifacts. Typically, this effect is eliminated by fitting the DCE-MRI enhancement curves to a sigmoid function [14, 15], which are prone to estimation errors.

In this article we describe how we exploited an unsupervised, non-parametric clustering algorithm, which does not require any prior expert knowledge about the thresholds to select the optimal predictor parameters, followed by the introduction of a classification decision-tree for accurate differentiation of malignant from benign ovarian tumors. Additionally, we introduced an efficient non-rigid registration approach and investigated the impact of registration on the classification results.



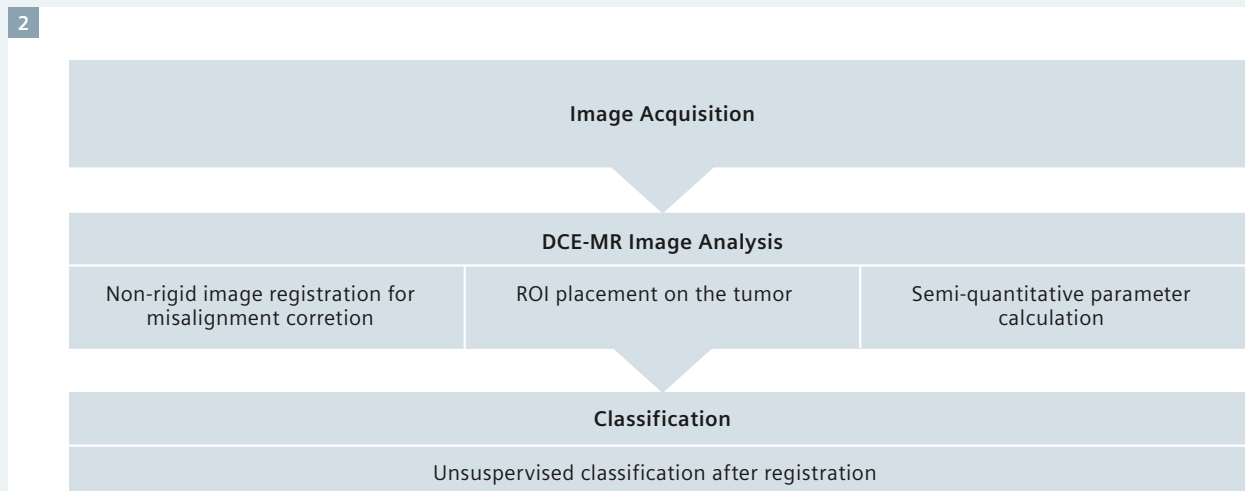
### Case analysis: How we do it

In what follows, we test the automated classification scheme on two patients, diagnosed histopathologically with benign and malignant complex adnexal cases. The overall procedure for the classification of benign and malignant complex adnexal masses is summarized (Fig. 2):

- Data acquisition (summarized in Table 1);
- Pre-processing: including the non-rigid registration scheme for motion correction;
- Quantification: consisting of ROI placement on tumor (we do not need to select an internal reference, as TTP and WIR do not require normalization), and quantitative parameter calculation;
- Classification: employing the decision tree of Figure 1 for distinguishing the tumor type.

**Table 1: Parameters of MRI sequences**

	SE T2w	SE T2w fat saturated	GRE FLASH T1w axial	GRE Spoiled fat saturated T1w (pre- and post- contrast)	3D Turbo FLASH T1w DCE-MRI
Plane	Coronal and/or Sagittal	Axial	Axial	Axial	Axial
TR (ms)	4000	5910	773	832	1.74
TE (ms)	100	96	11	11	5
Flip angle (°)	120	120	70	70	60
Field-of-view (mm <sup>2</sup> )	200 × 250	214 × 350	214 × 350	214 × 350	230 × 230
Slice thickness (mm)	5	4	4	4	5
Gap (mm)	1	1	1	0	0
Matrix	320 × 260	256 × 256	256 × 256	256 × 256	156 × 192



**2** The flow diagram of the overall classification procedure.

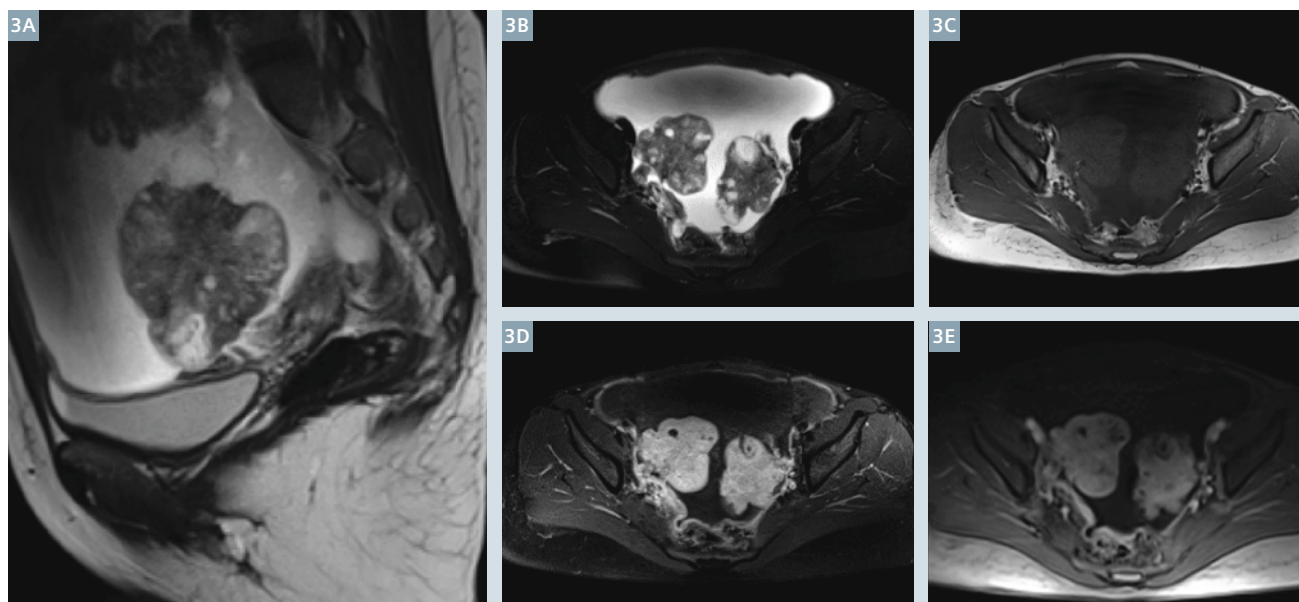
## Case 1: Serous Cystadenocarcinoma

The first example on the overall classification scheme is a 20-year-old patient, diagnosed with complex

adnexal mass on ultrasound examination. The postoperative histopathological assessment indicated the

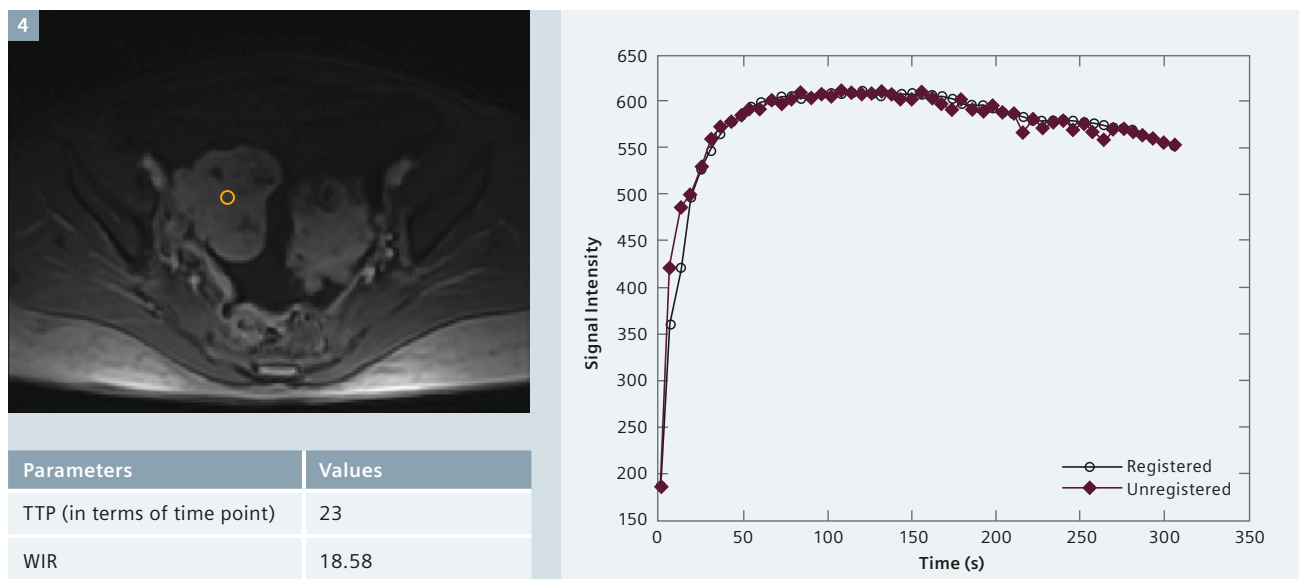
malignancy of the tumor in this patient. The stepwise classification procedure is as follow:

### Step 1: Image acquisition



**3** Figure 3: A 20-year-old patient diagnosed with complex adnexal mass on ultrasound examination: (3A) Sagittal T2w image; (3B) Fat-saturated axial T2w image; (3C) Pre-contrast fat-saturated axial T1w image; (3D) Post-contrast Fat-saturated axial T1w image; and (3E) axial DCE-MR image.

### Step 2: DCE-MR image analysis



**4** ROI placement on solid part of tumor tissue in a sample slice of DCE-MR image of the patient; the red stars represent the unregistered data points and the black circles denote the registered data points. The table indicates the parameter calculations.

### Step 3: Classification

$$\text{Output} = -0.21 \times 23 - 0.12 \times 18.58 + 8.4 = 1.34 > 0 \Rightarrow \text{malignant}$$

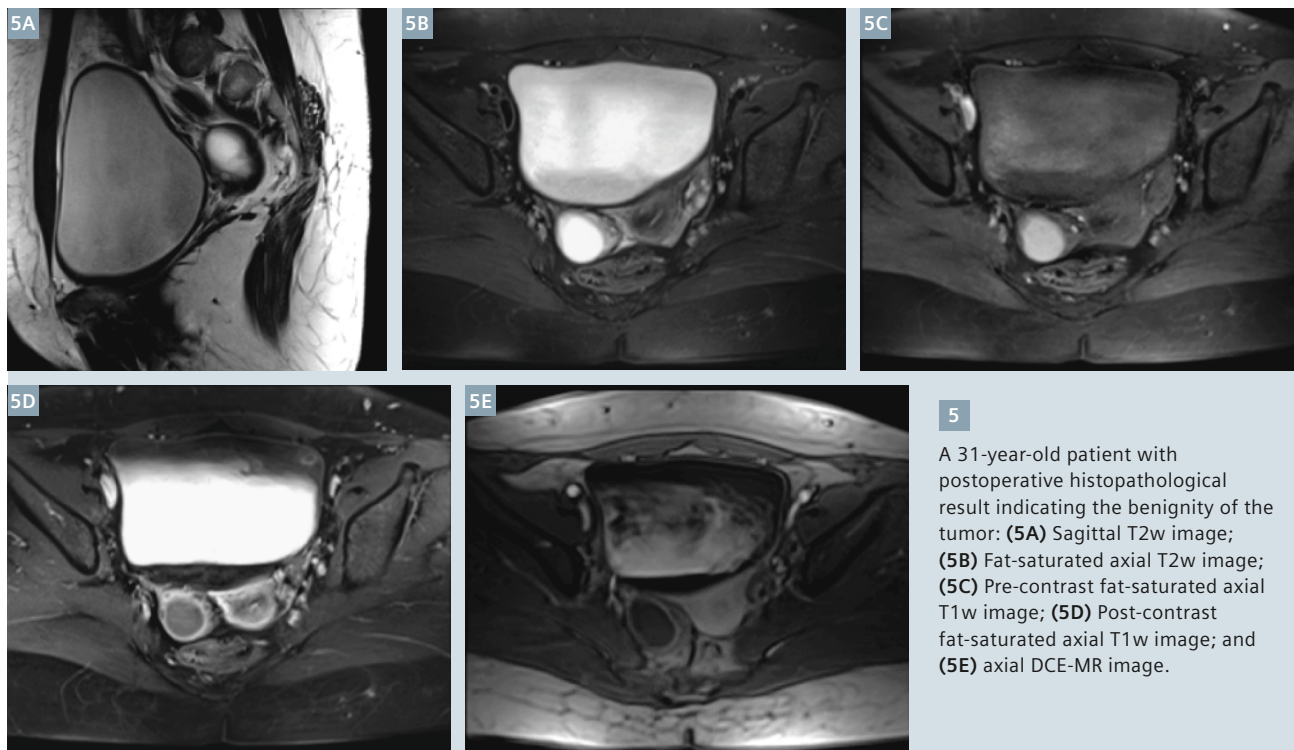


## Case 2: Serous Cystadenoma

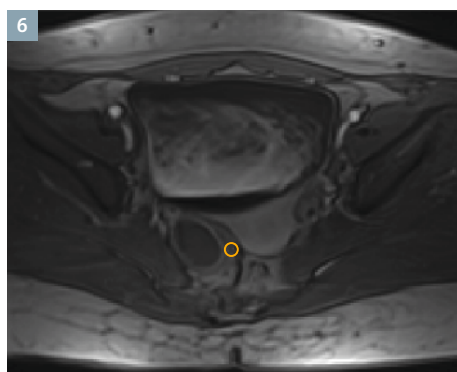
Here, we provide another example of determining the tumor type in a 31-year-old patient, in whom the

postoperative histopathological assessment result demonstrated that the cancer is benign.

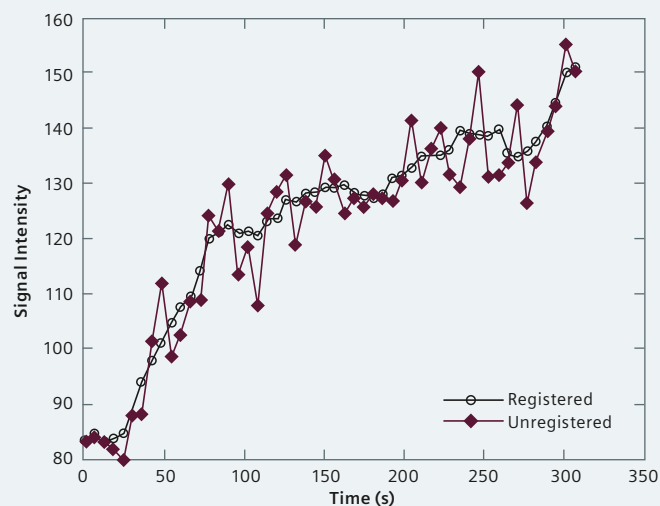
### Step 1: Image acquisition analysis



### Step 2: DCE-MR image analysis



Parameters	Values
TTP (in terms of time point)	51
WIR	3.48



**6** ROI placement on solid part of tumor tissue in a sample slice of DCE-MR image of the patient; the red stars represent the unregistered data points and the black circles denote the registered data points. The table indicates the parameter calculations.

### Step 3: Classification

$$\text{Output} = -0.21 \times 51 - 0.12 \times 3.48 + 8.4 = -2.73 < 0 \Rightarrow \text{benign}$$

## How we do it: Materials and methods

### Subjects

We obtained study approval from the Medical Ethics Committee of Tehran University of Medical Sciences, and patients were included if they provided written informed consent. Between June 2012 and March 2013, MR imaging was carried out preoperatively on twenty-two patients, who were scheduled for surgical removal of an ovarian mass, suspicious as malignant complex adnexal masses on US examination, had no contraindications for MR imaging and for receiving contrast agent. All of the patients underwent postoperative histopathological assessment.

### MR imaging protocol

Magnetic resonance images were acquired on a clinical 3T MR scanner (MAGNETOM Trio, A Tim System, Siemens Healthcare, Erlangen, Germany), with patients placed in a phased-array coil in the supine position. The patients fasted for 3 hours and received 20 mg of an antispasmodic drug (Hyoscine Butylbromide (Buscopan; Boehringer, Ingelheim, Germany)) injected intravenously immediately before MR imaging session to reduce bowel peristalsis. The following pulse sequences were applied:

- A sagittal and/or coronal T2-weighted fast spin-echo image from one femoral head to the other; bony Bankart lesion
- An axial fat-suppressed T2-weighted fast spin-echo images from the renal hilum to the symphysis pubis;
- An axial T1-weighted gradient-echo with breathhold;
- Pre- and post-contrast axial fat suppressed spoiled T1-weighted gradient-echo;
- Axial breathhold DCE-MRI using 3D Turbo FLASH T1-weighted fat-suppressed gradient echo consisting of 52 measurements with a temporal resolution of 6 s/frame. The acquisition was performed before and immediately after injection of 0.2 ml/kg of Gadolinium (Dotarem; Guerbet, Aulnay, France), followed by injection of 20 cc normal saline solution with 3 ml/min injection rate.

### Image analysis and quantification DCE-MRI registration

Two types of motion occur in DCE-MR images of abdominal organs:

- 1) Complex motion resulting from breathing, pulsation, and the natural movement of the organ-of-interest or its surrounding organs;
- 2) Motion of contrast agent in the tissue [17].

Motion correction of DCE-MR image series becomes a challenging issue in the sense that the proposed registration algorithm for rectifying the first type of motion must be unaffected by signal intensity changes during the bolus passage.

Misalignments of DCE-MR images of ovarian masses were corrected by registering each frame to a reference frame selected from the same series. The proposed registration approach composed of two steps: (1) 2D rigid registration employing normalized mutual information (NMI) as the similarity measure: the first image in the sequence of images was used as the reference and the consequent images were aligned with the first image; (2) 2D non-rigid registration using residual complexity (RC) similarity measure along with 2D Free Form Deformation (FFD) b-spline transformation, and the gradient descent optimization method.

The said registration approach was implemented and performed in MATLAB (MathWorks, Natick, MA, USA). The computation time was calculated using the developed software code.

### DCE-MRI quantification

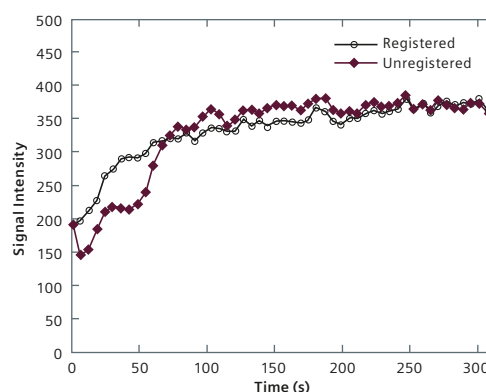
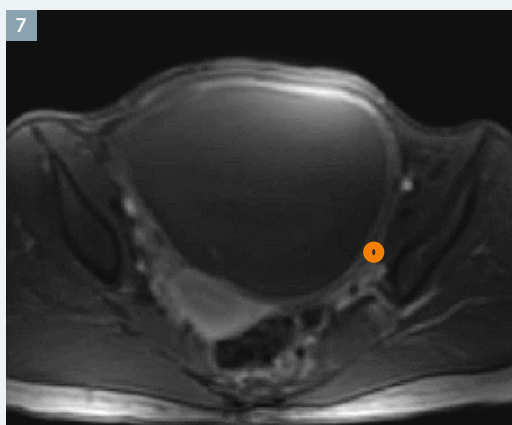
We arranged for the dynamic data to be analyzed by an experienced radiologist unaware of the patients' clinical and pathological information. Two regions-of-interest (ROIs) were drawn for each examination: one within the solid tissue of the adnexal tumor and one in the psoas muscle, as the internal reference. Signal intensity-time courses of these ROIs were determined over all time frames for semi-quantitative analysis. Semi-quantitative enhancement parameters, including maximum absolute enhancement (SI<sub>max</sub>), initial area under the curve in the first 60 seconds (IAUC<sub>60</sub>), wash-in-rate (WIR), and time-to-peak (TTP), were then calculated from the normalized signal intensity-time curves using an in-house software implemented in MATLAB. The quantitative parameters under investigation are summarized in Table 2.

### Classification of benign and malignant tumors

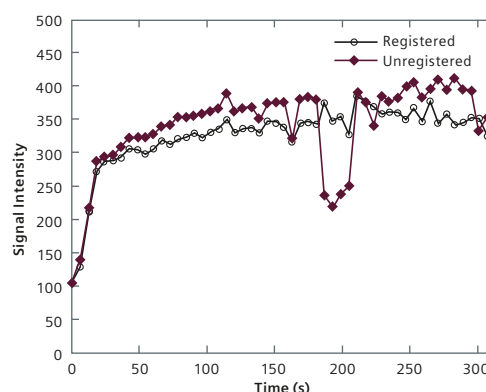
Classification was performed using each of the descriptive parameters and different sets of their combination, using linear discriminant analysis (LDA), before and after registration of the time-intensity curves. The objective of cluster analysis of semi-quantitative parameters was to find an optimal and accurate classifier for diagnosing the tumor type, for routine applications in clinical practice.

**Table 2:**  
Description of semi-quantitative parameters

Parameter	Description	Unit
SI <sub>max</sub>	Maximum absolute enhancement: maximum signal intensity of tumor normalized to that of psoas muscle, as an internal reference.	(Ratio)
IAUC <sub>60</sub>	Initial area under the time-intensity curve over the first 60 seconds after gadolinium injection, normalized to that of psoas muscle.	(Ratio)
TTP	Time-to-Peak: the time to the maximum absolute enhancement.	s
WIR	Wash-in-Rate = (SI <sub>max</sub> -SI <sub>0</sub> )/TTP	a.u./s



**7** Signal intensity time curve from unregistered images, and registered by residual complexity (RC) in a patient diagnosed histopathologically with benign ovarian mass.



**8** Signal intensity time curve from unregistered images, and registered by RC in a patient diagnosed histopathologically with malignant ovarian mass.

## Results

Informed consent forms were collected from a total of twenty-two patients with complex ovarian masses, who were recruited for this study. All subjects were scheduled for consequent surgery to remove at least one ovary and postoperative histopathological assessment. Of these patients 12 were included in the quantification with benign (three with bilateral masses), and 10 with malignant, complex ovarian masses (four with bilateral or multiple masses). Their mean age was 39.3 (age range 20–70). An experienced radiologist defined ROIs within the solid part of adnexal tumor and also in the psoas muscle, by examining the morphological images.

### The effect of registration on DCE-MRI curves

Figures 7 and 8 illustrate two examples, in which the registration highly improved the alignment of dynamic images. On the left side of Figures 7 and 8, the sample image and the selected ROI have been demonstrated

and on the right side, the mean signal intensity time courses have been calculated and drawn for the selected ROI obtained from unregistered image sequence and the images registered by RC similarity measure in two patients with benign and malignant tumors, respectively. The proposed non-rigid registration significantly improved the signal intensity time curves in benign ovarian masses with respect to unregistered data.

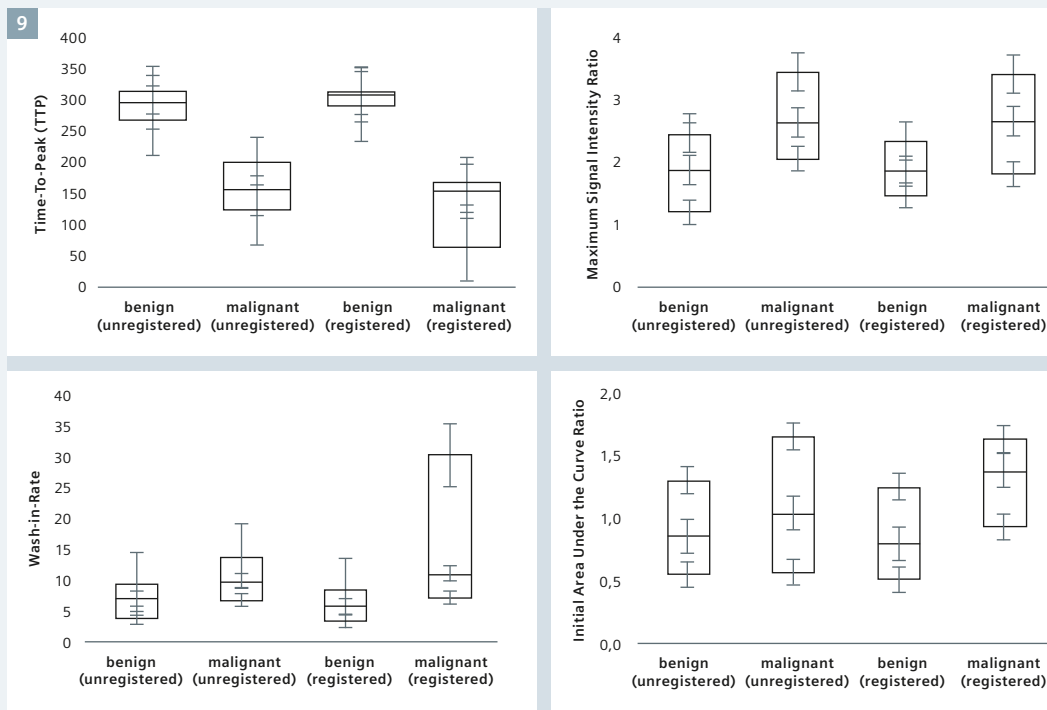
Figure 9 illustrates the box-and-whisker plots for TTP, SI<sub>max</sub>, WIR, and IAUC<sub>60</sub> for both benign and malignant tumors. A difference in the TTP was found between the benign and malignant groups ( $P < 0.001$ ). TTP was higher in benign than in malignant tumors. SI<sub>max</sub>, IAUC, and WIR were higher in malignant than in benign tumors. A difference was noted for SI<sub>max</sub> ( $P < 0.1$ ), but no significant difference was found among these two groups for WIR and IAUC ( $P > 0.1$ ), before motion correction. After registration, the separa-

tion among benign and malignant cancers significantly improved in TTP ( $P < 0$ ), and slightly in WIR ( $P < 0.1$ ) and IAUC ( $P < 0.1$ ) parameters. TTP and WIR parameters led to none and small overlaps between enhancement characteristics of benign and malignant tumors, respectively, suggesting their reliability in distinguishing cancer types.

### Classification of benign and malignant tumors

The classification of benign and malignant complex ovarian cancers was performed on each of the quantitative parameters individually and also on their combinations, before and after registration. The accuracy of classifier for each parameter set is summarized in Figure 10. It is apparent from the results that the classification accuracy of each parameter individually and in combination with other parameters, increases after registration, which is suggestive of the importance of motion correction in DCE-MRI context. TTP alone reaches a high accuracy for detecting malignancy (82%), which





**9** Investigating the effects of registration on differentiation of benign and malignant tumors using TTP,  $SI_{max}$ , WIR, and  $IAUC_{60}$  parameters using box-plots and whisker diagram.



**10** Evaluation of the designed classifier on individual parameters and several combination sets before and after registration, in terms of accuracy. It can be observed from the results that after registration, the results of classification improve greatly or in the case of  $SI_{max}$  alone, remain the same.

improves after registration (95.5%). The  $IAUC$  returns the least classification accuracy, both individually and when added to a combination of other parameters (e.g. by adding  $IAUC$  to the combination of  $SI_{max}$  and TTP, the accuracy values of classification before and after registration remain as 86.4% and 95.5% respectively).

The following feature sets were shown to induce the accuracy of 100% after registration:

- TTP, WIR
- TTP,  $SI_{max}$ , WIR
- TTP, WIR, IAUC
- TTP,  $SI_{max}$ , WIR, IAUC

We evaluated the robustness of all the classifiers using leave-one-out cross-validation. The combination of TTP and WIR, which has the smallest feature set, could reliably separate the benign and malignant complex ovarian cancers. The designed decision tree for classification of benign

and malignant tumors is indicated in Figure 1. If the output of this classifier has a positive value, the cancer should be interpreted as malignant; otherwise, it is a benign cancer.

Interestingly, the WIR and TTP parameters do not require the normalization of the signal intensity time curve; hence, the ROI placement on the psoas muscle could be eliminated, which could result in reduced calculations.

## Discussion

The work we have presented above addresses the problem of classifying complex ovarian masses using DCE-MRI semi-quantitative parameters, by employing an automated decision tree. We have evaluated the capability of several semi-quantitative parameters extracted from DCE-MRI signal intensity time courses in characterization of complex adnexal masses. The TTP parameter was the most sensitive parameter and WIR was the most specific parameter in discriminating benign from malignant complex ovarian tumors. These findings were consistent with previous findings: TTP, which is indicative of early enhancement, is confirmed to be related to the ovarian tumor malignancy [15], and WIR (the maximal slope ratio) has shown to correlate to the expression of vascular endothelial growth factor (VEGF), which is a biomarker of tumor malignancy [15]. In order to increase the overall classification accuracy, TTP and WIR were combined to create a decision tree for discriminating benign and malignant complex ovarian tumors.

In addition, we exploited an efficient non-rigid registration approach using RC similarity measure for correcting motion among consequent images in the dynamic time series. The indicated figures comparing the registered and unregistered data, suggest to us a positive impact of registration for improving the classification accuracy. To test the effect of registration on classification outcome, we explored the classification accuracy of individual and combinations of semi-quantitative parameters, achieved before and after RC registration. We have thus demonstrated that alignment of data could significantly enhance the capability of semi-quantitative parameters in characterization of complex ovarian cancers. In our view, this result is indicative of the importance of DCE-MRI registration, as an alternative to sigmoid data fitting, which is routinely used in literature to account for motion artifacts [14, 15, 18, 19]. We also believe that registration of dynamic series could lead to easier

calculation of characteristic parameters, could preserve the original properties of the acquired curves, and be reasonably robust and reproducible in contrast to sigmoid curve fitting, which is prone to fitting errors [20]. By evaluating the accuracy of different quantitative parameters – both individually and in combination with each other – we have been able to design a robust classifier, composed of WIR and TTP parameters, in the form of a decision tree. This classifier can therefore be used for the diagnosis of tumor type in routine clinical practice.

## Acknowledgements

We would like to thank Shaahin Mehdipour, MRI modality manager at Fanavarihayeh Azmayeshgahi – Iran Siemens Advanced Partner, for his great help and support; Payambaran Imaging Center, Tehran, for their cooperation in clinical research; and, Mahrooz Malek for sharing research data.

## References

- Jemal, A., et al., Cancer statistics, 2008. CA: a cancer journal for clinicians, 2008. 58(2): p. 71-96.
- Bharwani, N., R.H. Reznek, and A.G. Rockall, Ovarian cancer management: the role of imaging and diagnostic challenges. European journal of radiology, 2011. 78(1): p. 41-51.
- Chan, J.K., et al., Patterns and progress in ovarian cancer over 14 years. Obstetrics & Gynecology, 2006. 108(3, Part 1): p. 521-528.
- Brown, D.L., K.M. Dudiak, and F.C. Laing, Adnexal masses: US characterization and reporting. Radiology, 2010. 254(2): p. 342.
- Spencer, J.A. and S. Ghattamaneni, MR imaging of the sonographically indeterminate adnexal mass. Radiology, 2010. 256(3): p. 677.
- Spencer, J.A., et al., ESUR guidelines for MR imaging of the sonographically indeterminate adnexal mass: an algorithmic approach. European radiology, 2010. 20(1): p. 25-35.
- Hricak, H., et al., Complex Adnexal Masses: Detection and Characterization with MR Imaging – Multivariate Analysis 1. Radiology, 2000. 214(1): p. 39-46.
- Sohaib, S., et al., The role of magnetic resonance imaging and ultrasound in patients with adnexal masses. Clinical radiology, 2005. 60(3): p. 340-348.
- Adusumilli, S., et al., MRI of sonographically indeterminate adnexal masses. American Journal of Roentgenology, 2006. 187(3): p. 732-740.
- Lutz, A.M., et al., Early diagnosis of ovarian carcinoma: is a solution in sight? risk, 2011. 6: p. 8.
- Kinkel, K., et al., Indeterminate Ovarian Mass at US: Incremental Value of Second Imaging Test for Characterization – Meta-Analysis and Bayesian Analysis 1. Radiology, 2005. 236(1): p. 85-94.
- Vargas, H.A., T. Barrett, and E. Sala, MRI of ovarian masses. Journal of Magnetic Resonance Imaging, 2013. 37(2): p. 265-281.
- Dilks, P., et al., Can quantitative dynamic contrast-enhanced MRI independently characterize an ovarian mass? European radiology, 2010. 20(9): p. 2176-2183.
- Thomassin Naggara, I., et al., Dynamic contrast enhanced magnetic resonance imaging: A useful tool for characterizing ovarian epithelial tumors. Journal of Magnetic Resonance Imaging, 2008. 28(1): p. 111-120.
- Thomassin-Naggara, I., et al., Epithelial ovarian tumors: value of dynamic contrast-enhanced MR imaging and correlation with tumor angiogenesis 1. Radiology, 2008. 248(1): p. 148-159.
- Bernardin, L., et al., Effectiveness of semi-quantitative multiphase dynamic contrast-enhanced MRI as a predictor of malignancy in complex adnexal masses: radiological and pathological correlation. European radiology, 2012. 22(4): p. 880-890.
- Zöllner, F.G., et al., Assessment of 3D DCE-MRI of the kidneys using non-rigid image registration and segmentation of voxel time courses. Computerized Medical Imaging and Graphics, 2009. 33(3): p. 171-181.
- Carter, J.S., et al., Quantitative multiparametric MRI of ovarian cancer. Journal of Magnetic Resonance Imaging, 2013. 38(6): p. 1501-1509.
- Thomassin-Naggara, I., et al., Characterization of complex adnexal masses: value of adding perfusion-and diffusion-weighted MR imaging to conventional MR imaging. Radiology, 2011. 258(3): p. 793-803.
- Evelhoch, J.L., Key factors in the acquisition of contrast kinetic data for oncology. Journal of Magnetic Resonance Imaging, 1999. 10(3): p. 254-259.



## Contact

Dr. Hamidreza Saligheh Rad, Ph.D.  
Quantitative MR Imaging and Spectroscopy Group,  
Research Center for Molecular and Cellular Imaging,  
Institute for Advanced Medical Technologies  
Tehran University of Medical Sciences, Tehran, Iran  
Phone: (+98) 218 897 3653 – 108  
Fax: (+98) 216.648.2654  
h-salighehrad@tums.ac.ir

# Case Study: Yolk Sac Tumor

Maren Asmussen, M.D.; Peter Reimer, M.D.

Städtisches Klinikum Karlsruhe gGmbH, Department of Pediatric Radiology, Karlsruhe, Germany

Yolk sac tumor (YST) also known as an endodermal sinus tumor, is a rare malignant germ cell tumor.

## Patient history

1-year-old\* patient, consultation with pediatrician due to infection of the airway, child also tearful, increasingly apathetic.

Sonography depicted a mass in lower abdomen.  
Upon acceptance in the pediatric

clinic laboratory data were generated: CRP 10.5 mg/dl, LDH 554 U/l, Leukos 20.58/nl, Erys 2.95/pl, Hb 8.2 g/dl.

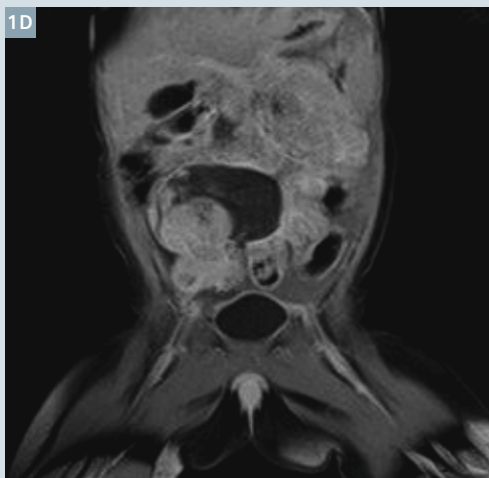
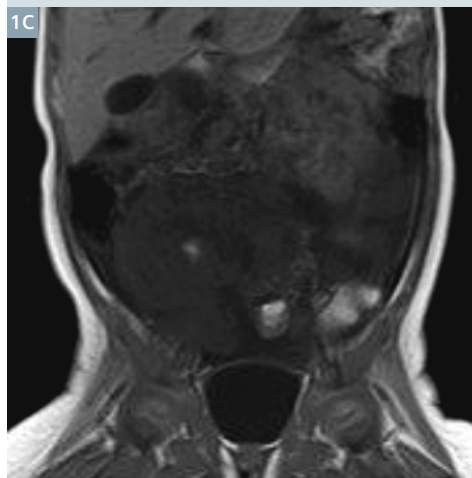
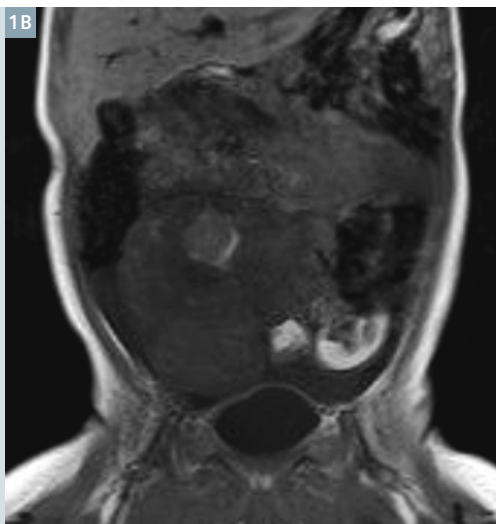
## MR imaging findings

Whole-body MR imaging (1.5T MAGNETOM Espree) showed a large intraperitoneal, supravescical mass lying on the right paramedian and median; the apical portion of the tumor appears highly inhomogeneous with partially more perfused and partially less perfused sections and

two hyperintense areas in T1, with the suspicion of hemorrhage. The caudal portion of the tumor appears less inhomogeneous with strong perfusion and large feeding arteries from the right arteria iliaca interna (syngo TWIST angiography not shown).

Moderate ascites. Major pleural effusion on the right, slight pleural effusion on the left, small pericardial effusion.

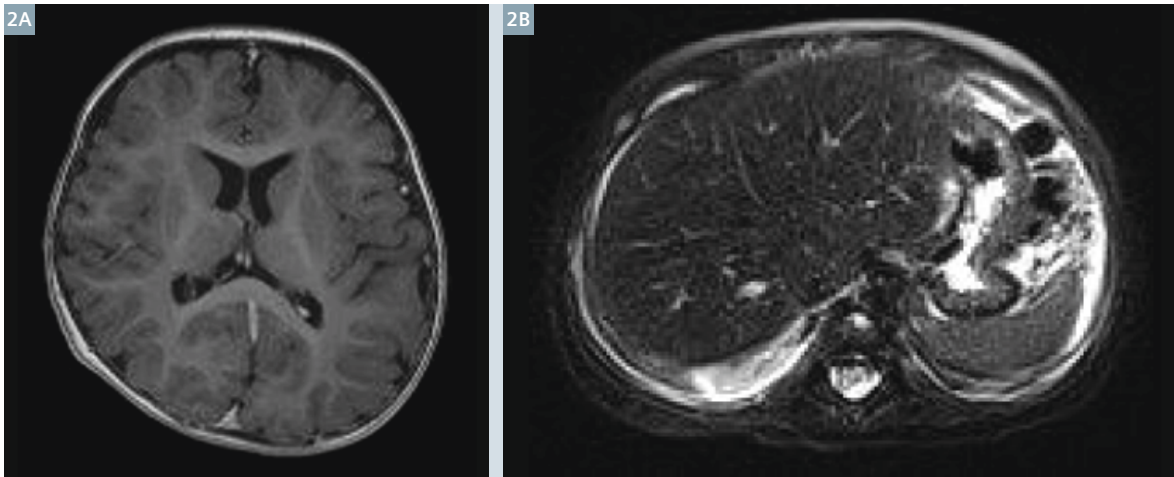
Small intestine partially distended with abundant fluid and air-fluid levels as



1

(1A) STIR coronal,  
(1B, C) T1-weighted  
native cor,  
(1D) T1-weighted  
post-contrast coronal.





2 Staging skull (2A), liver (2B).

indication of a blockage by the mass, currently no evidence of ileus.

No evidence of tumor-suspect or tumor pathological lymph nodes in the head, thorax or abdomen.

Insufficient lung ventilation accompanying pleural effusion, thus limited possibility for assessment of lungs.

To this extent no evidence of metastatic spread.

### Treatment and prognosis

**OP:** Right salpingo-oophorectomy. Tumor dorsally ruptured, partially adherent to sigma, no detectable macroscopic infiltration. Hemorrhagic ascites with parts of tumor.

### Histology:

Yolk sac tumor with partially reticular, partially solid, granular pattern. No mixed differentiation.

### Tumor stage:

Ic, R1

### Laboratory:

AFP 10605 ng/ml (post-OP 4172 ng/ml, after 6 weeks' therapy: 18.7 nl/ml)  
BHCG < 1.0 mU/ml

### Therapy:

Etoposide, cisplatin, ifosfamide

### Staging control:

No further residual tumor delimitable.

\* Siemens disclaimer: MR scanning has not been established as safe for imaging fetuses and infants less than two years of age. The responsible physician must evaluate the benefits of the MR examination compared to those of other imaging procedures.



### Contact

Maren Asmussen, M.D.  
Städtisches Klinikum Karlsruhe gGmbH  
Dept. of Pediatric Radiology  
Moltkestr. 90  
76133 Karlsruhe, Germany  
Phone: +49 (0)721 974 1950  
Maren.Asmussen@klinikum-karlsruhe.de

# Siemens Healthcare Publications

Our publications offer the latest information and background for every healthcare field. From the hospital director to the radiological assistant – here, you can quickly find information relevant to your needs.



**MAGNETOM Flash**  
Everything from the world of magnetic resonance imaging.



**SOMATOM Sessions**  
Everything from the world of computed tomography.



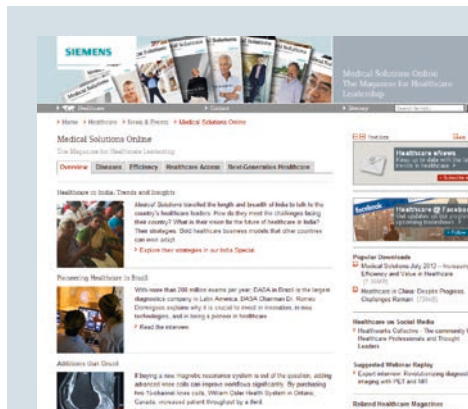
**Imaging Life**  
Everything from the world of molecular imaging innovations.



**AXIOM Innovations**  
Everything from the world of interventional radiology, cardiology, and surgery.



**Heartbeat**  
Everything from the world of sustainable cardiovascular care.



## Medical Solutions Online

The online version includes additional video features and greater depth to the articles in the printed healthcare leadership magazine. Read online at: [www.siemens.com/medical-solutions](http://www.siemens.com/medical-solutions)

For current and past issues and to order the magazines, please visit [www.siemens.com/healthcare-magazine](http://www.siemens.com/healthcare-magazine)

The entire editorial staff extends their appreciation to all the radiologists, technologists, physicists, experts and scholars who donate their time and energy – without payment – in order to share their expertise with the readers of MAGNETOM Flash.

#### MAGNETOM Flash – Imprint

© 2014 by Siemens AG,  
Berlin and Munich,  
All Rights Reserved

#### Publisher:

**Siemens AG**  
Medical Solutions  
Business Unit Magnetic Resonance,  
Karl-Schall-Straße 6, D-91052 Erlangen,  
Germany

#### Guest Editor:

Professor Anwar R. Padhani, MB BS,  
FRCP, FRCR.  
Consultant Clinical Radiologist at  
Mount Vernon Cancer Centre, London,  
UK and Professor of Cancer Imaging  
at the Institute of Cancer Research,  
Royal Marsden Hospital, London, UK.

**Editor-in-chief:** Antje Hellwich  
(antje.hellwich@siemens.com)

**Editorial Board:** Wellesley Were;  
Ralph Strecker; Sven Zühlsdorff, Ph.D.;  
Gary R. McNeal, MS (BME);  
Peter Kreisler, Ph.D.

**Production:** Norbert Moser, Siemens AG,  
Medical Solutions

**Layout:** independent Medien-Design  
Widenmayerstrasse 16, D-80538 Munich,  
Germany

**Printer:** G. Peschke Druckerei GmbH,  
Schatzbogen 35, D-81829 Munich,  
Germany

Note in accordance with § 33 Para.1 of  
the German Federal Data Protection Law:  
Despatch is made using an address file  
which is maintained with the aid of an  
automated data processing system.

MAGNETOM Flash is sent free of charge  
to Siemens MR customers, qualified  
physicians, technologists, physicists and  
radiology departments throughout the  
world. It includes reports in the English  
language on magnetic resonance:  
diagnostic and therapeutic methods and  
their application as well as results and  
experience gained with corresponding  
systems and solutions. It introduces from  
case to case new principles and proce-  
dures and discusses their clinical poten-  
tial. The statements and views of the  
authors in the individual contributions  
do not necessarily reflect the opinion of  
the publisher.

The information presented in these  
articles and case reports is for illustration  
only and is not intended to be relied  
upon by the reader for instruction as to  
the practice of medicine. Any health  
care practitioner reading this information  
is reminded that they must use their  
own learning, training and expertise in  
dealing with their individual patients.  
This material does not substitute for that  
duty and is not intended by Siemens  
Medical Solutions to be used for any  
purpose in that regard. The drugs and  
doses mentioned herein are consistent  
with the approval labeling for uses and/or  
indications of the drug. The treating

physician bears the sole responsibility for  
the diagnosis and treatment of patients,  
including drugs and doses prescribed in  
connection with such use. The Operating  
Instructions must always be strictly  
followed when operating the MR system.  
The sources for the technical data are the  
corresponding data sheets. Results may  
vary.

Partial reproduction in printed form of  
individual contributions is permitted,  
provided the customary bibliographical  
data such as author's name and title of  
the contribution as well as year, issue  
number and pages of MAGNETOM Flash  
are named, but the editors request that  
two copies be sent to them. The written  
consent of the authors and publisher is  
required for the complete reprinting of  
an article.

We welcome your questions and  
comments about the editorial content of  
MAGNETOM Flash. Please contact us at  
magnetomworld.med@siemens.com.

Manuscripts as well as suggestions,  
proposals and information are always  
welcome; they are carefully examined  
and submitted to the editorial board for  
attention. MAGNETOM Flash is not  
responsible for loss, damage, or any  
other injury to unsolicited manuscripts  
or other materials. We reserve the right  
to edit for clarity, accuracy, and space.  
Include your name, address, and phone  
number and send to the editors, address  
above.

MAGNETOM Flash is also available on the internet:

**[www.siemens.com/magnetom-world](http://www.siemens.com/magnetom-world)**

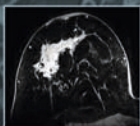


# MAGNETOM Flash

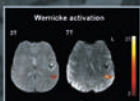
The Magazine of MRI

Issue Number 4/2014 | Oncology Edition

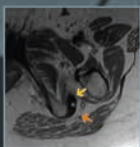
Not for distribution in the US



Clinical Multiparametric  
MR Imaging of Breast  
Tumors at 7 Tesla  
Page 54



fMRI in Presurgical  
Planning at 7T  
Page 20



3 Tesla MR Neurography-  
Guided Posterior Femoral  
Cutaneous Nerve Block  
Page 26

59

Please enter your business address

Institution

Department

Function

Title

Name

Street

Postal Code

City

State

Country

MR system used

Please include me in your mailing list for the following Siemens Healthcare customer magazine(s):

- ☐ Medical Solutions
- ☐ MAGNETOM Flash
- ☐ SOMATOM Sessions
- ☐ AXIOM Innovations

Stay up to date with the latest information

Register for:

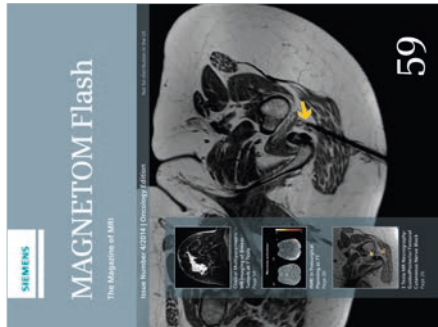
E-mail

☐ Yes, I consent to the above information being used for future contact regarding product updates and other important news from Siemens.

☐ unsubscribe from info service

Please print clearly!

# MAGNETOM Flash



Siemens AG  
Healthcare Sector  
Magnetic Resonance  
Antje Hellwich – Marketing  
P.O. Box 32 60  
D-91050 Erlangen  
Germany



→ Visit [www.siemens.com/magnetom-world](http://www.siemens.com/magnetom-world)  
for case reports,  
clinical methods,  
application tips,  
talks and much more  
clinical information.

**SUBSCRIBE NOW!**

– and get your free copy of future  
**MAGNETOM Flash!** Interesting information from  
the world of magnetic resonance – gratis to your  
desk. Send us this postcard, or subscribe online at  
[www.siemens.com/MAGNETOM-World](http://www.siemens.com/MAGNETOM-World)

On account of certain regional limitations of sales rights and service availability, we cannot guarantee that all products included in this brochure are available through the Siemens sales organization worldwide. Availability and packaging may vary by country and is subject to change without prior notice. Some/All of the features and products described herein may not be available in the United States.

The information in this document contains general technical descriptions of specifications and options as well as standard and optional features which do not always have to be present in individual cases, and which

may not be commercially available in all countries. Due to regulatory reasons their future availability cannot be guaranteed. Please contact your local Siemens organization for further details.

Siemens reserves the right to modify the design, packaging, specifications, and options described herein without prior notice. Please contact your local Siemens sales representative for the most current information.

Note: Any technical data contained in this document may vary within defined tolerances. Original images always lose a certain amount of detail when reproduced.

\*MAGNETOM 7T is still under development and not commercially available yet. Its future availability cannot be ensured. This research system is not cleared, approved or licensed in any jurisdiction for patient examinations. This research system is not labelled according to applicable medical device law and therefore may only be used for volunteer or patient examinations in the context of clinical studies according to applicable law.

Not for distribution in the US

#### Global Business Unit

Siemens AG  
Medical Solutions  
Magnetic Resonance  
Henkestraße 127  
DE-91052 Erlangen  
Germany  
Phone: +49 9131 84-0  
[www.siemens.com/healthcare](http://www.siemens.com/healthcare)

#### Local Contact Information

##### Asia/Pacific:

Siemens Medical Solutions  
Asia Pacific Headquarters  
The Siemens Center  
60 MacPherson Road  
Singapore 348615  
Phone: +65 6490 6000

##### Canada:

Siemens Canada Limited  
Healthcare Sector  
1550 Appleby Lane  
Burlington, ON L7L 6X7, Canada  
Phone +1 905 315-6868

#### Europe/Africa/Middle East:

Siemens AG, Healthcare Sector  
Henkestr. 127  
91052 Erlangen, Germany  
Phone: +49 9131 84-0

##### Latin America:

Siemens S.A., Medical Solutions  
Avenida de Pte. Julio A. Roca No 516, Piso  
C1067 ABN Buenos Aires, Argentina  
Phone: +54 11 4340-8400

##### USA:

Siemens Medical Solutions USA, Inc.  
51 Valley Stream Parkway  
Malvern, PA 19355-1406, USA  
Phone: +1 888 826-9702

#### Global Siemens Headquarters

Siemens AG  
Wittelsbacherplatz 2  
80333 Muenchen  
Germany

#### Global Siemens Healthcare Headquarters

Siemens AG  
Healthcare Sector  
Henkestraße 127  
91052 Erlangen  
Germany  
Phone: +49 9131 84-0  
[www.siemens.com/healthcare](http://www.siemens.com/healthcare)